Study on Application of Soil Infiltration and Evapotranspiration Models for Estimating Field Water Consumption in a Developing Country

博士学位論文

Study on Application of Soil Infiltration and Evapotranspiration Models for Estimating Field Water Consumption in a Developing Country

白木　秀太郎

SHIRAKI SHUTARO

博士学位論文

Study on Application of Soil Infiltration and Evapotranspiration Models for Estimating Field Water Consumption in a Developing Country

2022 年 11 月 11 日

白木　秀太郎

Contents

Chapter 1. General Introduction

1.1. Introduction of the study site and irrigable area

The study site is Yezin dam irrigable area, located near Yezin village, Zayarthiri Township, Naypyitaw, Myanmar. The dam is constructed in 1975 for flood protection and water irrigation, among other purposes. The planned irrigation area is 6,400 ha, the household numbers 5,000 households, and the canal length is 115 km. (Irrigation and Water Utilization Management Department) (Figure 1-1).

Figure 1-1 Location of study site and Yezin dam irrigation area

The Köppen climate classification subtype of this site is tropical savanna climate. The amount of rainfall is average 1,725 mm from 2006 to 2011 and 1,872 mm from 2011 to 2016. The temperatures are an averaged maximum of 44.0℃ and a minimum of 10.5℃. Meanwhile, the overall average temperature is 27.5℃ in 2006–2011 and 42.2℃, 11.0℃, and 26.4℃ in 2011–2016. Figures 1 and 2 show the changes in daily air temperature and monthly precipitation from January 2017 to February 2020 in the study site.

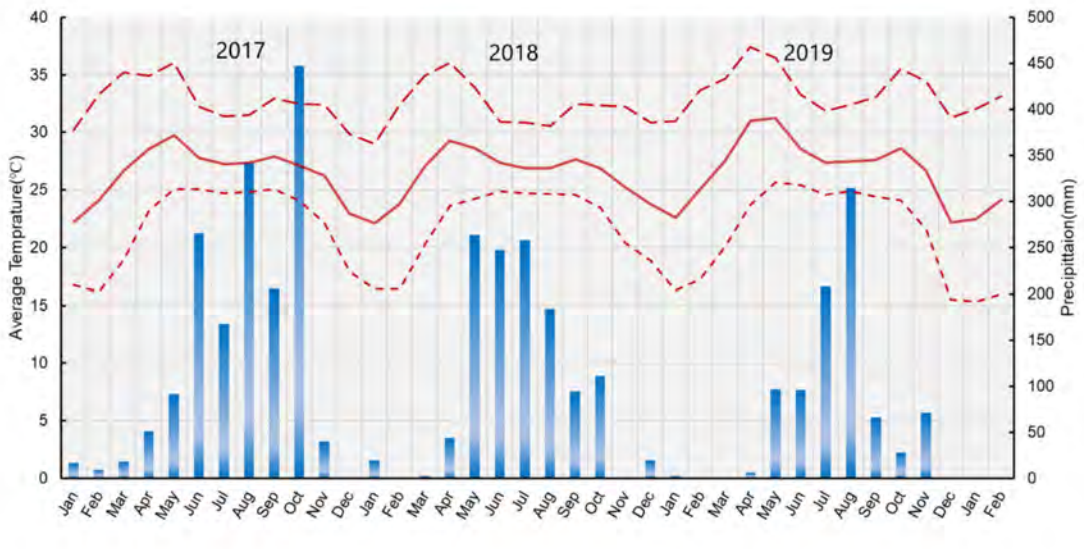

Figure 1-2 Changes in daily air temperature described with maximum and minimum (dashed line), mean (solid line), and monthly precipitation (bar) from January 2017 to February 2020 in the study site.

The Yezin dam irrigation area is located near Naypyidaw, which replaced Yangon as the capital city of Myanmar in 2006. Consequently, the irrigation supply from the dam has been decreasing due to a rapid increase in demand for domestic water. In recent years, the irrigated area was only 1,500 ha for paddy rice in the summer/dry season out of the 6,400 ha of total irrigable area. The irrigation supply was suspended from February 2016 to May 2017 due to the water shortage of the dam resulting from low rainfall in 2015 (Figure 1-3).

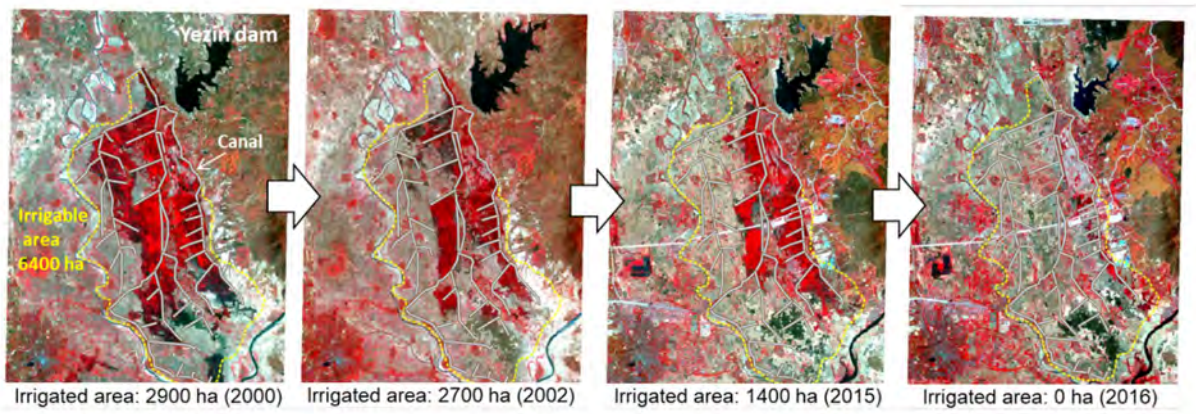

Figure 1-3 Changes in the irrigation area (paddy field) and a lake surface of the Yezin dam in April presented by the normalized difference vegetation index (NDVI). Colored red and dark areas indicate the healthy vegetation cover and the water surface, respectively.

The irrigation area of the Yezin dam strongly depends on the annual rainfall. Because the catchment area of the dam is smaller than the irrigable area, the water storage of the dam will not increase without sufficient rainfall. In addition, irrigation water demand competes with domestic water demand. Since it is difficult to increase the amount of water supply for future irrigation, irrigation water with reduced water loss and applying water-saving techniques are required. However, in Myanmar, there have been few studies for irrigation planning on the water consumption of agricultural fields associated with evapotranspiration (*ET*) and drainage to the underground.

1.1. Challenges of study on water consumption in developing countries

Water consumption of fields includes drainage to the underground through soil penetration and *ET* from vegetation and ground surface. Good underground drainage can lead to less water stress for crops; conversely, poor drainage can result to wet damage for crops. Moreover, *ET* is one of the important factors that govern the matter production of plants. Thus, the amount of water consumption of the fields is an essential information for crop cultivation and irrigation planning. However, especially in developing countries, characterizing water consumption in practice faces many challenges due to the limitation in the observation system. It is difficult to install and maintain expensive observation systems, such as weighing lysimeters and eddy covariance, for measuring *ET*. Therefore, in developing countries, simple observation methods are used to evaluate the characteristics of water consumption in an agricultural field.

1.1.1. Challenges of study on field-saturated hydraulic conductivity

The infiltration process is quantified by determining the infiltrated amount of water for time that can be expressed as the cumulative infiltration I (L) and the infiltration rate i (L T^{-1}). Infiltration measurements have been mainly used to estimate soil saturated hydraulic conductivity. This infiltration property is a key to correctly describing all the components of the soil and land surface hydrologic balance and is essential in the appropriate design of irrigation systems. In dry soils, initial infiltration rates are substantially higher than the saturated hydraulic conductivity of the surface layer due to capillary effects which control the sorptivity of the soil. However, as infiltration proceeds, the gradient between the pressure head at the soil surface and the pressure head below the wetting front reduces over time so that the infiltration rate finally reaches a constant value that approximates saturated hydraulic conductivity [1]. There are various methods of in situ infiltration tests to evaluate the infiltration characteristics. In developing countries, a simple method, such as ring infiltrometer, is used for field tests. A ring is driven vertically into the ground, water is poured into the ring, and reads of the depth of water reduction are taken.

One problem with field tests is that it requires a large amount of water and effort,

especially in arid regions and during the dry season. Moreover, laboratory test using undisturbed soil samples taken from a field is not suitable for the evaluation of actual field conditions, such as soil cracks, vegetation cover, and root distribution. For data analysis, using infiltration models, a solver function (e.g., Excel) is generally used to fit the observed data into models, and the field-saturated hydraulic conductivity (K_{fs}) parameter is estimated. Philip's infiltration model [2] is one of the most widely used models because of its simple form and clear theoretical concept [3]. One problem for data analysis is the infiltration models, which are theoretically derived based on assumptions that are often compatible with actual conditions in field soils [4, 5]. The boundary conditions of Philip's infiltration model are very restrictive. Therefore, it is impossible to satisfy the model in practice [6, 7]. Many studies have been conducted in which field infiltration data yielded negative or zero K_{fs} values by applying Philip's infiltration model (e.g., [8–18]). However, as yet, there has been no discussion regarding how to deal with a negative value of K_{fs} obtained due to the limitation of Philip's infiltration model.

1.1.2. Challenges of measurement on evapotranspiration

The standard method for direct *ET* measurements has been the use of weighing lysimeters. In the last decades, the eddy covariance has been increasingly used for micrometeorological studies of surface fluxes [19]. Although previous studies considered these measurements as an accurate method to assess *ET* [20], installation and operational costs are expensive, and these are challenging to install in developing countries because of the required continuous maintenance and security purposes. For this reason, in general, actual *ET* is estimated using the reference evapotranspiration (ET_0) and crop coefficient (Kc = ET / ET_0) from the FAO-56 equation [21]. However, since Kc primarily depended on the dynamics of canopies (cover fraction and leaf area index) [22], Kc cannot be used in all conditions. Moreover, in developing countries, including Myanmar, agricultural production and crop growth are poor due to low-yield varieties, poor soil, and a lack of knowledge of crop management for farmers. Thus, actual *ET* should be directly observed, and Kc values should be determined based on actual *ET* in Myanmar.

The Bowen ratio energy balance (BREB) method is an alternative to lysimetric measurements and the eddy covariance method [23]. It is widely used to directly estimate *ET* because of its clear physical concept, simple formula, simple data collection, and inexpensive measuring instruments. However, the BREB method has a large number of assumptions and constraints. Thus, it often produces unacceptable fluxes in practical situations based on the following inherent problems. The first problem is that the BREB yields a significantly inaccurate flux magnitude when the Bowen ratio (β) approaches −1 because the denominator in the BREB formula is $1 + \beta$. The reduction of the occurrence of this problem requires an increase in the accuracy of the thermo-hygrometers suggested [24]. The second problem is that the BREB method yields the incorrect directions for the heat fluxes opposite to the observed vertical

differences in the air temperature/water vapor pressure.

However, few papers were reported that deal with the data using the BREB method for checking, and the specific meteorological conditions that cause these problems are poorly understood. When applying the BREB method, it is important to understand the meteorological conditions when the method fails, and unacceptable fluxes should be rejected based on the clearly defined objective criteria.

1.1.3. Parameters estimation of *ET* model

Measurement and estimation of *ET*, which is composed of crop transpiration (*T*) and soil water evaporation (*E*), are essential for many applications in agriculture. *T* is associated with plant productivity, while *E* is regarded as ineffective water consumption that does not directly contribute to plant productivity [25]. Thus, quantification of *T* and *E* is important for developing systems that optimize crop productivity by reducing invalid water consumption [26]. However, the observation of *T* and *E* is not easy because it requires multiple expensive measurement devices. During the last decade, the two-layer Shuttleworth-Wallace (SW) evapotranspiration model, which can partition *ET* into *E* and *T*, has been widely used with good results for different types of sparse crops and climatic conditions [27−32]. However, its practical application is somewhat limited, since it is a highly complex model with a large number of specific parameters, and it is hard and costly to continuously measure all of these elements [33]. Moreover, the general approach in model fitting for parameter estimation (e.g., least-square method) does not take into account the uncertainty in the observations [34].

The Bayesian approach has been used recently to simultaneously estimate the SW model parameters against the observed field-based *ET* [35−39]. The Bayesian approach combines probability distributions of model parameters based on prior probabilities for magnitude and uncertainty, using observed data to generate posterior distributions of parameters. This not only allows the quantification of model inputs, parameters, and outputs uncertainties, but it also takes into account prior knowledge for all parameters and addresses unknown influences [40]. However, these previous studies have used a non-hierarchical Bayesian approach for parameter estimation of SW models, which cannot consider the variation in observed conditions for a dataset. The non-hierarchical approach means that the results are based on a specific set of parameter estimates, which are obtained in a specific observation group with specific conditions at a specific time. These results can not necessarily be generalized among different conditions and groups [41]. It is critical to consider the effects of the changes in season and observed conditions in the parameters of the SW model when simulating *ET* over a long term [38].

1.2. Objectives and composition of this thesis

The objectives of this thesis are (1) to propose an evaluation method for solving the problems of observation and data analysis on water consumption and (2) to evaluate the characteristics of infiltration and *ET* in agricultural fields in a tropical savanna climate region of Myanmar. This thesis consists of four subjects and is compiled from four published research papers on water consumption in agricultural fields in Myanmar.

Chapter 2 discusses the problem of determination of K_{fs} using a dataset of 27 field infiltration tests with a double-ring infiltrometer. The chapter objectives are (1) to investigate the soil physical factors that gave negative K_{fs} value estimated by the infiltration model, (2) to demonstrate a method for obtaining nonnegative K_{fs} values, and (3) to evaluate five infiltration models for selecting a suitable model matched to the conditions of tested fields.

Chapter 3 discusses the *ET* calculation error using the BREB method with the hourly meteorological data from six agricultural field sites in three different seasons. The chapter objectives are (1) to perform rejection determinations for the BREB calculation flux based on the objective criteria improved for data with the Bowen ratio approaching −1 and the incorrect sign of fluxes and (2) to clarify the data features and the meteorological conditions when the BREB method fails.

Chapter 4 evaluates the possibility of parameter estimation with a hierarchical Bayesian inference using a field-based *ET* dataset collected from five agricultural fields over three seasons. The chapter objective is to validate the estimation of *ET* and the parameters of the single- and two-layer *ET* models calibrated using simple and hierarchical Bayesian approaches.

Chapter 5 demonstrates the *ET* estimation using simple measurements with statistical model. The chapter objectives are (1) to determine the *ET* and Kc for double rice ratoon cropping and (2) to infer the water productivity and viability of practicing ratoon rice cropping in Myanmar.

Chapter 6 summarizes the results from Chapters 2 to 6.

Chapter 2. Field Infiltration Test

Evaluation of Infiltration Models and Field-saturated Hydraulic Conductivity In Situ Infiltration Tests during the Dry Season

2.1. Introduction

Field-saturated hydraulic conductivity (K_{fs}) (LT^{-1}) is the hydraulic conductivity of soil when it has been brought to a near-saturated state by water applied abundantly to the land surface by processes such as ponded infiltration, heavy rainfall, or irrigation [42]. Determination of K_{fs} is very important in irrigation studies and water flow modeling [43] because it is an indicator of the economic and technical feasibility of irrigation projects. K_{fs} values are often estimated by fitting an infiltration model to measured data [4, 44] by using nonlinear optimization algorithms; many studies assessing the infiltration models for measured data have been published (e.g., [3, 13, 18, 45−47]).

For irrigation planning during the dry season in Myanmar, we conducted field infiltration tests in 27 agricultural fields by using a double-ring infiltrometer to determine the value of K_{fs} by applying the Philip model [2]. It is one of the most widely used model for evaluating infiltration data measured by ring infiltrometers [4, 48] due to its simple form and clear theoretical concept [3]. However, in our preliminary analyses, for estimating K_{fs} by curve fitting using the Philip model produced negative values for many fields, and the fitting performance of this model to the measured data was very poor, indicating that this model was not satisfied by the infiltration characteristics of tested fields. Watson [4] and Maheshwari et al. [5] concluded that theoretically derived equations based on assumptions such as those of the Philip model are often incompatible with actual conditions in field soils. [6, 7] noted that the boundary conditions of the Philip model are very restrictive, and it is therefore impossible to satisfy the model in practice. Furthermore, there have been many studies in which field infiltration data yielded negative or zero K_{fs} values by applying the Philip model (e.g., [8, 8−15, 17−18]). However, as yet, there has been no discussion regarding how to deal with negative K_{fs} values obtained due to the limits of the Philip model. Therefore, it is important to investigate factors that cause K_{fs} values to become negative and to establish a method of properly obtaining nonnegative K_{fs} values. The objectives of this study, therefore, were the following: 1) to select an infiltration model that is most applicable to field conditions that is likely to get negative K_{fs} values of the Philip model, 2) to determine the factors that result in negative K_{fs} values, and 3) to present a method of obtaining valid K_{fs} values using tested infiltration models.

2.2. Materials and Methods

2.2.1. Field measurements

As many field infiltration tests as possible should be performed for irrigation planning in a large-scale area to gain an understanding of infiltration characteristics when considering heterogeneous soil. However, it was difficult to perform an infiltration test over a long period at many fields because of the limited water supply during the dry season. In this study, therefore, a short-period infiltration test ($Test_{short}$) was performed for an average of 60 min in 23 fields in agricultural fields and DAR's experimental fields for estimating K_{fs} values by infiltration models, and a long-period test ($Test_{long}$) was performed for an average of 360 min in four fields in DAR's experimental fields for directly measuring the final infiltration rate-approximated K_{fs} value. The location of 27 tested fields in Yezin irrigation area and a photograph of field experiment are shown in Figure 1. The tested field was named based on the village or place and site number. A double-ring infiltrometer with an inner ring 30 cm in diameter and an outer ring 55 cm in diameter was driven vertically into the ground in each field to a depth of 10 cm (see Figure 2-1). In three fields (SP3, KC1, and KC2), the inner ring was used alone to avoid cracks in the soil surface. The outer ring and inner ring were filled with water to approximately the same depth (approximately 5–10 cm), and measurements were taken immediately. We continued to take measurements until the infiltration rate reached an approximately constant value. In $Test_{long}$ (DAR6, DAR7, DAR8, and DAR9), the inner ring was covered with thick paper to prevent evaporation of ponding water inside of the ring.

We also collected undisturbed soil cores (50 × 51 mm) from three soil layers at depths of 0–5 cm, 10–15 cm, and 20–25 cm in tested fields near the site of the infiltration test for laboratory testing, including evaluation of soil texture by the pipet method, volumetric water content and bulk density by the oven drying method, and porosity by the pycnometer method. The relationship between physical properties of the soil and infiltration characteristics was analyzed. As a reference, three photographs of soil profile at depths of 0–30 cm after sampling of soil cores are shown in Figure 2-1, and organic matter and soil aggregation were not observed except at the surface layer in the photographs.

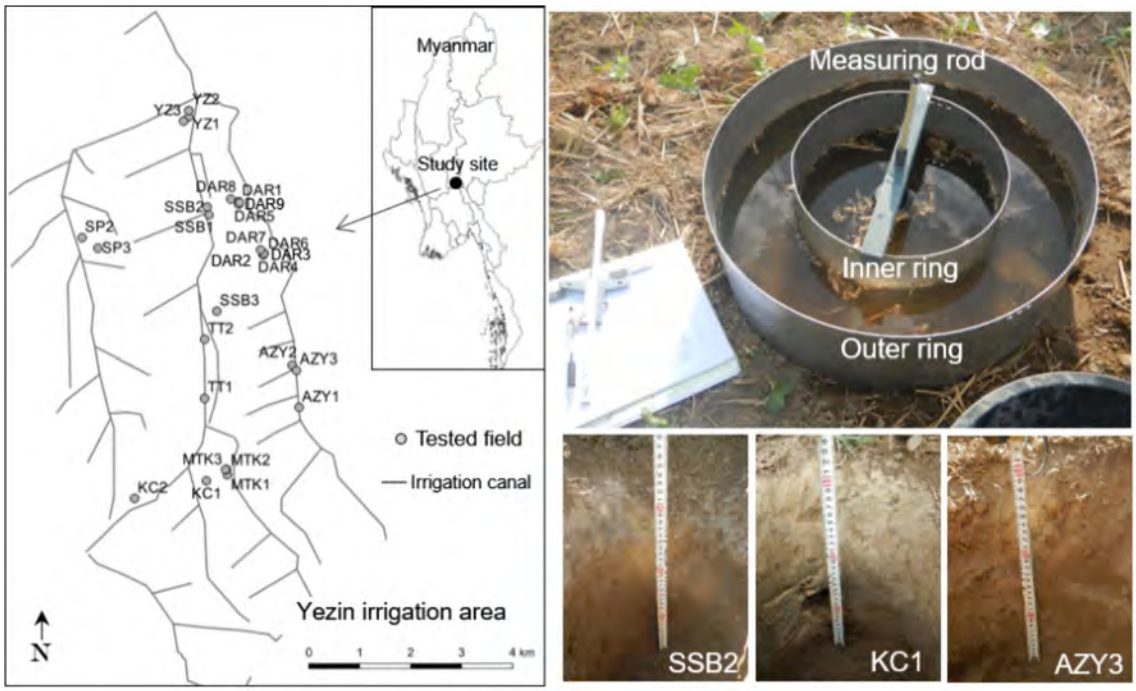

Figure 2-1. Map of the study site with 27 tested fields, of which 23 were tested over a short period and four were tested over a long period. Infiltration tests were located in Yezin irrigation area. Photographs include the field experiment setup for the double-ring infiltrometer, and three examples of soil profile at a depth of 0–30 cm are shown.

2.2.2. Infiltration models and equations

The K_{os} parameter is commonly estimated by fitting some algebraic infiltration equation to measured data or by other procedures—for instance, using the quasi-steady part of the measured data [49]. Because this paper focused on the problem of the negative K_{fs} value by fitting of the Philip infiltration model, we selected five infiltration models and adopted one constant single-head calculation approach to compare with the K_{fs} values given by the fitting of models. The criteria for selecting the models and the approach were that they should be well established in the literature and widely used by scientists and engineers. Three widely known, physically based infiltration models (Equations 2-1 to 2-3) and two empirical models (Equations 2-4 to 2-5) to estimate K_{fs} values by parameter fitting were used, and a constant single-head calculation approach (Equations 2-6) to calculate reference K_{fsref} values directly from the measured data was used, as described below.

(1) Philip [2] developed an infinite-series solution to solve the nonlinear partial differential Richards equation. The general form of the Philip model with physically interpretable parameters is expressed in powers of the square root of time as follows:

$$I = S_p t^{1/2} + A_p t \tag{2-1}$$

Where I (L) is the infiltration amount (cumulative infiltrated depth) in time t (T), S_p ($LT^{-0.5}$) is the sorptivity, and A_p (LT^{-1}) is the permeability coefficient, which is considered to be equivalent to K_{fs} [46, 50]. The A_p/K_{fs} ratio is not clear and is dependent upon the time of infiltration, initial moisture content, and soil properties [51]. The range of the Ap/K_{fs} ratio is proposed to be between 0.3 and 0.4 [52]; a ratio of A_p/K_{fs} = 2/3 is often used [4].

(2) Swartzendruber [53] used an adjusted Philip time-series solution and proposed an alternative series solution that is applicable to all infiltration times and accounts for surface ponding [44, 53]:

$$I = A_s t + \frac{S_s}{A_0}\left[1 - exp\left(-A_0 t^{1/2}\right)\right] \tag{2-2}$$

Where A_s (LT^{-1}) is the estimated value of K_{fs}, S_s ($LT^{-0.5}$) is the sorptivity, and A_0 is an empirical constant (unitless) that depends on soil parameters.

(3) Brutsaert [54] proposed another correction for gravitational force by using the horizontal infiltration solution of the Philip model [2]:

$$I = A_b t + \frac{S_b^2}{BA_b}\left[1 - \frac{1}{1 + (BA_b t^{1/2})/S_b}\right) \tag{2-3}$$

Where A_b (LT^{-1}) is the estimated value of K_{fs}, S_b ($LT^{-0.5}$) is the sorptivity, and parameter B is an empirical constant (unitless) that is fixed at 1/3, 2/3, or 1; for most practical purposes, B = 1 is recommended [55].

(4) Mezencev [56] proposed the modified Kostiakov model, also called the Mezencev model or the Kostiakov–Lewis model [46], which includes the term ultimate infiltration capacity (f_0):

$$I = ct^n + f_0 t \tag{2-4}$$

Where f_0 (LT^{-1}) is the final infiltration rate at steady state, which is the estimated value of K_{fs}, and c and n are empirical constants (unitless) ($c > 0$ and $0 < n < 1$).

(5) Horton [57] presented a three-parameter semiempirical infiltration model:

$$I = I_c\, t + \frac{(I_0 - I_c)}{k}[1 - e^{-k\, t}] \tag{2-5}$$

Where I_c (LT^{-1}) is the final infiltration rate, which can be used as an estimate of K_{fs} [45]. Parameter I_0 (LT^{-1}) is the presumed initial infiltration rate at t = 0, and k (T^{-1}) is a constant representing the rate of decrease in I (L) capacity.

(6) Reference K_{fsref} values for comparing K_{fs} values given by the fitting models were calculated using a constant single-head calculation approach [49, 58] as follows:

$$K_{fsref} = \frac{q_s}{H/(C_1 d + C_2 a) + 1/sn(C_1 d + C_2 a) + 1} \tag{2-6}$$

Where q_s (LT^{-1}) is the quasi-steady infiltration rate calculated from the final reading, H (L) is the average ponding depth inside the ring, d (L) is the depth of ring insertion into the soil, a (L) is the radius of the inner ring, C_1 and C_2 are dimensionless quasi-empirical constants, and sn (L^{-1}) is the soil macroscopic capillary length or the sorptive number [59]. For the purposes of this study, a, d, and sn were assumed to be 30 cm, 10 cm, and 0.12 cm^{-1}, respectively, in all fields. The constants C_1 and C_2 were 0.316π and 0.184π, respectively, for $d \geq 3$ cm and $H \geq 5$ cm [60].

2.2.3. Optimization of model parameters

(1) Fitting tools for determining parameters

Fitting of infiltration models to measured data was carried out by means of nonlinear least squares optimization procedures. Parameters were optimized to minimize an objective function, which contained the least squares solution of the measured and predicted cumulative infiltration at each measured time. The following objective function was used:

$$\text{SSE} = \sum_{j=1}^{n} \left(I(m)_j - I(p)_j\right)^2 \tag{2-7}$$

Where SSE is the sum of square error, n is the total number of infiltration reading, $I(m)_j$ is the measured cumulative infiltration and $I(p)_j$ is the predicted cumulative infiltration at reading time j. The optimization process was performed using three types of software, each with a different algorithm designed for nonlinear programming problems: the generalized reduced gradient method [61] using the Microsoft Excel solver function, the Levenberg–Marquardt method [62, 63] in Gnuplot using the fit function [10], and the differential evolution algorithm for global

optimization using the DEoptim in R software [64].

(2) Unconstrained and constrained curve fitting

Constraining the fitting range for determining parameters would influence the result for the model evaluation. The influence of the unconstrained and the constrained fitting was not examined in the previous studies on the evaluation of infiltration models mentioned above. Therefore, in this study, after revealing the differences in the fitting performance with unconstrained and constrained fitting, we used a constrained/unconstrained fitting that could be favorable for fitting performance for the analysis of the model parameters.

(3) Fitting range of parameter K_{fs} for constrained fitting

The fitting range for parameter K_{fs} was subtly different between the three fitting tools due to different software functions. In the solver function of Microsoft Excel, variables were optimized as unconstrained nonnegative values so that the fitting range was $K_{fs} \geq 0$. In the fit function of Gnuplot, because there is no option to set the fitting range for variables, the inverse trigonometric function (arctangent) was assigned to the model equation for constrained curve fitting. For example, given the equation K_{fs} = (arctangent (x)/π + 0.5) × 2, where x is a fitting parameter, the range of K_{fs} was fixed as $0 < K_{fs} < 120$. The upper limit value (120 mm h^{-1}) was set considering the measured data. In the DEoptim, the upper and lower limits of K_{fs} were specified as an argument of function; the fitting range was fixed as $0 \leq K_{fs} \leq 120$.

2.2.4. Model evaluation for fitting quality

Infiltration models were evaluated by comparing the measured and the predicted cumulative infiltration (mm) by using objective criteria commonly used in model evaluation: the root mean square error (RMSE), the mean absolute error (MAE), the root mean squared percentage error (RMSPE), the mean absolute percentage error (MAPE), and the Nash and Sutcliffe efficiency (NSE) [42]. RMSE provides an overall measure of the degree to which the data differ from model predictions. MAE can potentially be used to identify bias. When RMSE and MAE equal zero, this indicates a perfect fit. RMSPE and MAPE were used as indicators of the margin of error. NSE is widely used in hydrological models and is a normalized statistic that determines the relative magnitude of the residual variance compared with the measured data variance. NSE ranges between −∞ and 1.0, with NSE = 1.0 being optimal.

2.2.5. Analysis of the fitted parameter K_{fs}

(1) The influence of infiltration time on the fitting of parameter K_{fs}

We analyzed the accuracy of K_{fs} estimates fitted using different infiltration times at each reading from $Test_{long}$ where approximated K_{fs} (K_{fsapp}) was measured. The accuracy of fitted K_{fs} value was evaluated by the relative error (RE) which was computed from the fitted K_{fs} versus the K_{fsapp} value. The fitted K_{fs} value was obtained from each cumulative infiltration period was increased by one reading from 30 min after initiating the $Test_{long}$.

(2) Factors for determining the sign of fitted K_{fs}

To clarify the relationship between the sign of fitted K_{fs}, and physical properties of the soil and infiltration characteristics, we statistically analyzed the physical properties of soil and the infiltration characteristics, in which fitted K_{fs} was negative and nonnegative for the 23 tested fields in $Test_{short}$ using Student's *t*-test and discriminant analysis [66, 67]. To examine the effect of initial infiltration for K_{fs} fitting, the behavior of the A_p value of the Philip model was analyzed using data with different initial infiltration times from $Test_{short}$.

(3) Method of obtaining valid K_{fs} values

In field conditions that are biologically and physically affected, the application of the Philip model established in a uniform soil having uniform moisture content is limited. The constant infiltration on the assumption of the Philip model indicates that soil moisture content in soil at penetration time $t = 0$ instantaneously rises to saturated moisture content on infiltrated soil surface at penetration time $t > 0$ after ponding. In this study, the infiltration characteristics caused by drying of the surface soil at the initial stage would be difficult to satisfy the assumption of the Philip model, and the problematic initial infiltration should be rejected for adapting the Philip model. We implemented and subsequently improved a previously specified cumulative linearization approach [68, 69] to determine the initial infiltration period that should be rejected for the best fitting of the Philip model to the measured data. Firstly, both sides of Equation (2-1) were divided by $t^{1/2}$ to give a linear function, Equation (2-8), with slope A_p and intercept S_p:

$$\frac{I}{t^{1/2}} = A_p t^{1/2} + S_p \tag{2-8}$$

Secondly, we nondimensionalized the amount of change of $t^{1/2}$ and $I/t^{1/2}$, divided by the maximum value of $t^{1/2}$ and $I/t^{1/2}$ to give Equation (2-9):

$$\frac{I_a/t_a^{1/2} - I_1/t_1^{1/2}}{I_n/t_n^{1/2} - I_1/t_1^{1/2}} = \frac{t_a^{1/2} - t_1^{1/2}}{t_n^{1/2} - t_1^{1/2}} \tag{2-9}$$

Where I_a (mm) and t_a (min) is the cumulative infiltration amount and the time of an arbitrarily selected reading ($1 \leq a \leq n$), t_1 is the time of the first reading after the rings were filled with water, and t_n is the time of the final reading. The left-hand side of Equation (2-9) is the change ratio of infiltration rate, and the right-hand side is the change ratio of time. Using predicted data, the terms on both sides in Equation (2-9) are equal and take values between zero and one. Therefore, using measured data, when the values on both sides of Equation (2-9) are equal or approximately equal, the measured data are approximate to or coincide with the predicted data of the Philip model. Hence, it is necessary to identify the period of initial infiltration that minimizes the differences between each side of Equation (2-9). The optimal time of initial infiltration for best fitting was determined by RMSE values between the both sides of Equation (2-9).

2.3. Results and Discussion

2.3.1. Laboratory testing of soil cores

The results of laboratory tests (sample size = 27) are shown in Table 2-1. The name of the tested field was indicated from the village or place with the site number. The percentage contents of soil texture, porosity, and bulk density are presented as the averages for the three layers (0–5, 10–15, and 20–25 cm deep). The texture of the soil was primarily sandy loam (10 fields), and clay loam (11 fields), as classified by the International Society of Soil Science. The volumetric water content (VWC) ($cm^3\ cm^{-3}$) of the surface soil varied greatly due to the difference in the soil texture. At a depth of 0–30 cm, the average VWC of sandy loam is 0.17 and that of clay loam is 0.26. Variation in the particle density, porosity, and bulk density of the two textures was small compared with that in other properties.

Table 2-1 Field condition and soil properties of 27 tested fields, of which 23 were tested with short-period testing and four were tested with long-period infiltration tests. Soil texture was classified according to the International Soil Science Society (ISSS). The bulk density, soil texture, particle density, and porosity are presented as the averages for the three layers (0–5, 10–15, and 20–25 cm deep).

Tested field	Field Condition	Volumetric water content			Bulk density	Soil texture (ISSS)	Sand content	Silt content	Clay content	Particle density	Porosity
		0–5 cm	10–15 cm	20–25 cm							
		(cm^3 cm^{-3})			(g cm^{-3})		(%)	(%)	(%)	(g cm^{-3})	(%)
DAR1	Fallow, unplowed	0.08	0.13	0.15	1.69	Sandy loam	78	12	10	2.52	35
DAR2	Fallow, plowed	0.09	0.15	0.18	1.71	Sandy loam	79	11	10	2.52	35
DAR3	Fallow, plowed	0.12	0.17	0.21	1.68	Sandy loam	78	11	11	2.52	35
DAR4	Fallow, plowed	–	–	–	–	Sandy loam	75	13	12	–	–
DAR5	Black gram	0.09	0.22	0.32	1.62	Clay loam	55	26	19	2.52	31
DAR6	Black gram	0.08	0.13	0.23	1.73	Clay loam	54	26	20	2.52	31
DAR7	Sesame, unplowed	0.25	0.29	0.31	1.71	Clay loam	54	24	22	2.60	34
DAR8	Fallow, plowed	0.16	0.27e	0.26	1.70	Sandy clay loam	79	6	15	2.61	33
DAR9	Sunflower	0.10	0.13	0.17	1.68	Sandy loam	80	11	9	2.59	32
SP2	Black gram	0.30	0.29	0.38	1.63	Light clay	43	27	30	2.54	39
SP3	Black gram	0.31	0.35	0.34	1.60	Light clay	35	31	34	2.54	32
MTK1	Fallow, plowed	0.15	0.29	0.33	1.58	Clay loam	49	29	22	2.56	39
MTK2	Sweet corn	0.13	0.23	0.35	1.54	Clay loam	54	30	16	2.58	42
MTK3	Green gram	0.19	0.29	0.36	1.50	Clay loam	51	34	15	2.57	41
TT1	Green gram	0.17	0.33	0.30	1.52	Clay loam	42	35	23	2.57	38
TT2	Horse gram	0.11	0.24	0.31	1.65	Clay loam	48	31	21	2.58	36
SSB1	Fallow, unplowed	0.18	0.25	0.23	1.81	Sandy loam	68	18	14	2.52	36
SSB2	Sesame	0.24	0.24	0.26	1.62	Sandy loam	66	19	15	2.54	35
SSB3	Black gram	0.30	0.34	0.38	1.58	Clay loam	45	32	23	2.55	39
YZ1	Fallow, unplowed	0.16	0.30	0.39	1.50	Clay loam	49	29	22	2.52	40
YZ2	Fallow, plowed	0.18	0.29	0.36	1.55	Clay loam	41	36	23	2.49	38
YZ3	Fallow, unplowed	0.19	0.27	0.10	1.64	Sandy clay loam	67	17	16	2.56	36
AZY1	Fallow, plowed	0.12	0.18	0.15	1.79	Sandy loam	70	16	14	2.55	30
AZY2	Fallow, unplowed	0.10	0.17	0.26	1.64	Sandy loam	67	19	14	2.57	36
AZY3	Fallow, unplowed	0.24	0.19	0.21	1.68	Sandy loam	80	13	7	2.56	35
KC1	Fallow, unplowed	0.14	0.25	0.30	1.68	Light clay	41	33	26	2.55	34
KC2	Harvested black gram	0.18	0.17	0.19	1.80	Sandy clay loam	59	19	22	2.56	30

2.3.2. Measured infiltration data

Figure 2-2 shows the cumulative infiltration curve resulting from 23 short-period tests ($Test_{short}$) and four long-period tests ($Test_{long}$). The approximated K_{fs} (K_{fsapp}) was calculated from the final reading in $Test_{long}$, which was the rate when the infiltration change rate reached one percent to four percent. The fields of $Test_{long}$ were DAR6, DAR7, DAR8, and DAR9. The K_{fsapp} vales seemed to affect the soil texture. In DAR 6 and DAR7, with a small K_{fsapp}, the soil texture was clay loam, and in DAR8 and DAR9, with a relatively large K_{fsapp}, the soil was sandy clay loam and sandy loam (see Table 2-1). It was presumed that the K_{fs} estimates of $Test_{short}$ would be more than 0.8 m h^{-1} considering the infiltration curve of $Test_{short}$ and the K_{fsapp} vales of $Test_{long}$.

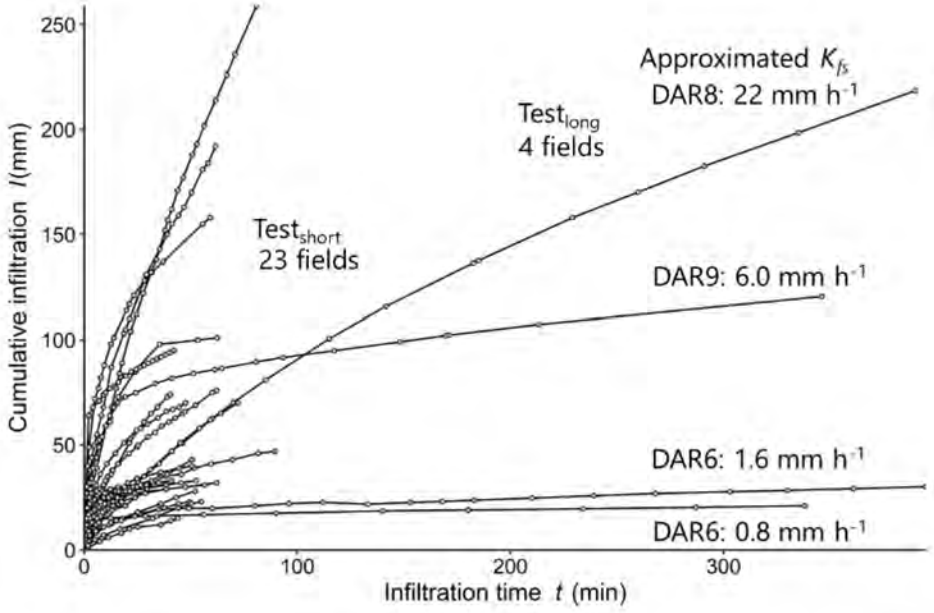

Figure 2-2. Measured infiltration data of 23 short-period infiltration tests ($Test_{short}$) and four long-period infiltration tests ($Test_{long}$). The approximated K_{fs} and the names of the tested fields of $Test_{long}$ are shown.

To understand the features of the measured and predicted infiltration curve, three examples (DAR1, TT2, YZ1) of $Test_{short}$ using unconstrained and constrained fitting by the Philip model are represented in Figure 2-3. The fitting range for constrained fitting was fixed as parameter $A_p \geq 0$ (mm h^{-1}), and RMSE (mm) was calculated from the differences between the predicted and the measured data for cumulative infiltration.

In DAR1, which is sandy loam and a fallow, unploughed field, the fitting performance with constrained fitting was poor, and the large infiltration in the initial stage appeared to fit with difficulty. In TT2, which is clay loam and where beans were cultivated, the unconstrained fitting curve roughly matched the measured data compared with the constrained fitting. In YZ1, which is clay loam and a fallow, unploughed field, the fitting curve approximately matched the measured data, regardless of the constraint conditions. In DAR1 and TT2, which produced negative A_p by unconstrained fitting in both the measured data, the initial infiltration was larger and the late infiltration was smaller than the predicted data with constrained fitting. It was assumed that—with unconstrained fitting—the shape of the infiltration curve affected the determination of the sign of parameter A_p.

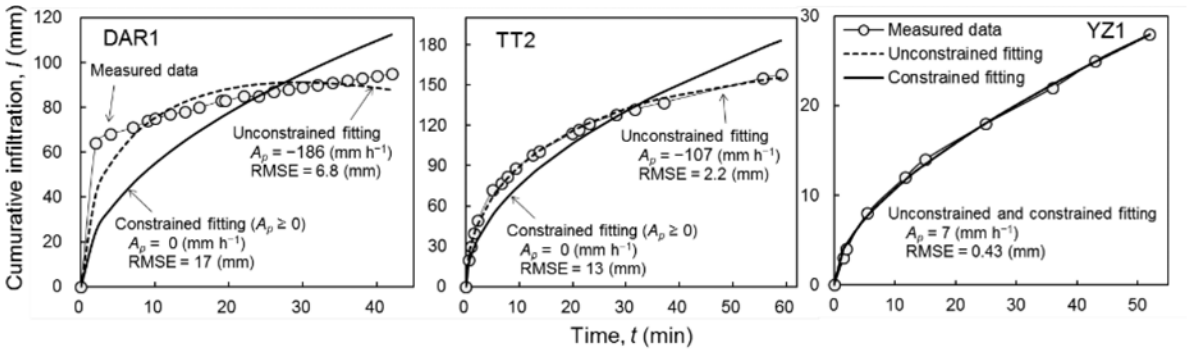

Figure 2-3 Three examples of $Test_{short}$ using unconstrained and constrained fitting with parameter $A_p \geq 0$ (mm h^{-1}) by the Philip model. The RMSE (mm) was calculated from differences between the predicted and the measured data for cumulative infiltration.

2.3.3. Fitting performance

The five models, including the Philip model for comparison with other four models, were fitted to the measured data using unconstrained and constrained curve fitting. Results of the evaluation of the fitting performance for $Test_{short}$ are presented in Table 2-2. The right-hand column of Table 2-2 shows the percentage of fields in which the fitted parameter K_{fs} was negative or was less than 0.1 mm h^{-1}, and asterisks indicate significant differences in fitting performance between the unconstrained and the constrained fitting for each model. The fitting tools used for unconstrained fitting were the fit function of Gnuplot and the solver function of Excel, although the result was the same for both the software.

In the part of unconstrained fitting, the model with the best fitting accuracy was the Mezencev model and those with the worst fitting accuracy were the Philip model. The fitting performances of the Swartzendruber, Brutsaert, and Horton models were similar. Regarding estimates of K_{fs}, the Philip, Swartzendruber, Brutsaert, and Mezencev models produced negative values for many fields. There were only two fields (MTK3 and AZY2) for which all models produced a nonnegative K_{fs} value. The Horton model gave a nonnegative K_{fs} value for all fields. In the part of constrained fitting, most K_{fs} values in fields which were negative for unconstrained fitting became zero or less than 0.1 mm h^{-1}. Considering the approximated K_{fs} (K_{fsapp}) values resulting from $Test_{long}$ (average 7.6 mm h^{-1} and minimum 0.8 mm h^{-1}), it is unlikely that the K_{fs} value was zero or very small in many fields. The fitting performance of the Mezencev and Philip models was significantly reduced by constrained fitting, whereas the Swartzendruber and Brutsaert models varied according to fitting tool and constraints. On the other hand, the Horton model was less affected by fitting conditions and did not given any negative K_{fs} values. We conclude that constrained fitting did not work well except for the Horton model, and it is necessary to consider that the fitting constraints influenced the evaluation of infiltration models on the determination of parameters.

Table 2-2 Evaluation of fitting performance of models using unconstrained and constrained fitting for $Test_{short}$ (short-period infiltration test). Bold font indicates the best result based on the criteria used. The right-hand column shows the percentage of fields in which the fitted parameter K_{fs} was negative or less than 0.1 mm h^{-1}, and asterisks indicate significant differences in fitting performance between unconstrained and constrained fitting (sample size = 23).*significant at $p < 0.05$, **significant at $p < 0.03$, ***significant at $p < 0.01$, MAE: mean absolute error, MAPE: mean absolute percentage error, RMSPE: root mean squared percentage error.

Fitting tool and condition	Model	RMSE (mm)	Rank	MAE (mm)	Rank	RMSPE	Rank	MAPE	Rank	NSE	Rank	Rank-mean	Negative K_{fs} or K_{fs} < 0.1 mm h^{-1} (%)
Fit or Solver Unconstrained fitting	Philip	1.541	5	1.246	5	0.102	5	0.060	5	0.973	5	5.0	65
	Swartzendruber	1.113	2	0.879	2	0.099	3	0.052	3	0.989	3	2.6	44
	Brutsaert	1.204	3	0.954	3	0.099	4	0.053	4	0.985	4	3.6	65
	Mezencev	**0.896**	**1**	**0.720**	**1**	**0.072**	**1**	**0.042**	**1**	0.991	2	**1.2**	78
	Horton	1.318	4	1.085	4	0.081	2	0.046	2	**0.993**	**1**	2.6	0
Fit Constrained $0 < K_{fs} < 120$	Philip	4.034^{***}	5	3.436^{***}	5	0.157^{*}	4	0.120^{***}	5	0.910^{*}	5	4.8	65
	Swartzendruber	1.877^{***}	4	1.531^{***}	4	0.197^{***}	5	0.103^{***}	4	0.948^{**}	4	4.2	30
	Brutsaert	**1.269**	**1**	**1.019**	**1**	0.109	2	0.059	2	0.983	2	1.6	39
	Mezencev	1.553^{*}	3	1.282^{*}	3	0.120^{*}	3	0.068^{**}	3	0.971	3	3.0	74
	Horton	1.318	2	1.085	2	**0.081**	**1**	**0.046**	**1**	**0.993**	**1**	**1.4**	0
Solver Constrained $0 \leq K_{fs}$	Philip	4.038^{**}	5	3.437^{***}	5	0.157^{*}	4	0.120^{***}	5	0.910^{*}	5	4.8	65
	Swartzendruber	1.834	3	1.519	3	0.125	3	0.071	3	0.982	2	2.8	56
	Brutsaert	2.109^{**}	4	1.820^{**}	4	0.163	5	0.106^{***}	4	0.950^{**}	4	4.2	74
	Mezencev	1.555^{*}	2	1.281^{*}	2	0.120^{*}	2	0.068^{**}	2	0.971	3	2.2	78
	Horton	**1.361**	**1**	**1.126**	**1**	**0.083**	**1**	**0.048**	**1**	**0.992**	**1**	**1.0**	0
DEoptim Constrained $0 \leq K_{fs} \leq 120$	Philip	4.034^{**}	5	3.436^{***}	5	0.157^{*}	5	0.120^{***}	5	0.910^{*}	5	5.0	65
	Swartzendruber	**1.214**	**1**	**0.964**	**1**	0.110	2	0.058	2	0.985	2	**1.6**	48
	Brutsaert	1.309	2	1.048	2	0.116	3	0.061	3	0.983	3	2.6	35
	Mezencev	1.568^{**}	4	1.296^{**}	4	0.121^{*}	4	0.069^{**}	4	0.970	4	4.0	83
	Horton	1.318	3	1.085	3	**0.081**	**1**	**0.046**	**1**	**0.993**	**1**	1.8	0
Mean Constrained	Philip	4.035	5	3.436	5	0.157	5	0.120	5	0.910	5	5.0	65
	Swartzendruber	1.642	4	1.338	4	0.144	4	0.077	4	0.972	3	3.8	45
	Brutsaert	1.562	3	1.296	3	0.129	3	0.075	3	0.972	2	2.8	49
	Mezencev	1.559	2	1.286	2	0.120	2	0.068	2	0.971	4	2.4	78
	Horton	**1.332**	**1**	**1.098**	**1**	**0.082**	**1**	**0.047**	**1**	**0.992**	**1**	**1.0**	0

2.3.4. Influence of infiltration time on accuracy of parameter K_{fs} estimate

The relationship between the relative error (RE) for evaluating K_{fs} estimate accuracy and infiltration time are shown in Figure 2-4. The RE was computed from the approximated K_{fs} (K_{fsapp}) vs. the fitted K_{fs} in $Test_{long}$. The fitted K_{fs} values were obtained from each cumulative infiltration increased by one reading from 30 min after initiating the $Test_{long}$. The K_{fsapp} value was calculated from the final reading of $Test_{long}$. Samples for which the fitted K_{fs} value was negative were excluded. The target parameters were A_s for the Swartzendruber, A_b for the Brutsaert, and I_c for the Horton model, except for the Philip and Mezencev, due to many fitted K_{fs} became negative in each cumulative infiltration.

The correlation coefficient for parameters A_s and A_b was small, indicating that infiltration time has little influence on K_{fs} estimate accuracy. In contrast, the estimate accuracy of I_c was strongly correlated with infiltration time. For this model, the longer the infiltration time, the more accurate the K_{fs} estimate becomes. The Horton model therefore has an advantage; the value of I_c can be corrected to the tested time. The value of I_c fitted from the measured data for 60 min was I_{c60} and for 360 min, it was I_{c360}; the correction formula in case of this field condition was represented as $K_{fs} = 0.36 \times I_{c60}$ ($r^2 = 0.940$) and $0.93 \times I_{c360}$ ($r^2 = 0.979$), respectively. The value of I_{c60} was overestimated by a factor of approximately 2.8.

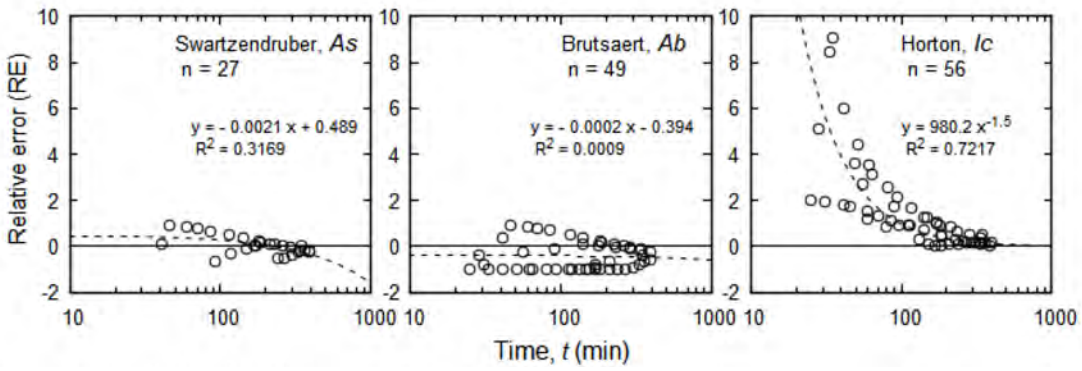

Figure 2-4 Relationship between infiltration time and K_{fs} estimate accuracy in $Test_{long}$ (long-period infiltration test). The RE was computed from the approximated K_{fs} vs. the fitted K_{fs}. The approximated K_{fs} value was calculated from the final reading in $Test_{long}$. The fitted K_{fs} value was obtained from each cumulative infiltration increased by one reading from 30 min after initiating the $Test_{long}$. Samples for which the fitted K_{fs} value was negative were excluded. (n: sample size)

2.3.5. Factor for determining the sing of fitted K_{fs}

Differences in the physical properties of soil and infiltration characteristics from fields with negative and nonnegative K_{fs} values in $Test_{short}$ are presented in Table 2-3. The target models were the Mezencev, Philip, Brutsaert, and Swartzendruber models, except for the Holton model, which provided nonnegative K_{fs} value. The percentage contents of soil components and porosity are presented as the averages for three layers (0–5, 10–15, and 20–25 cm deep); the initial infiltration rate (I_{ini}) was calculated from the first reading and the late infiltration rate (I_{late}) was calculated from the final reading in $Test_{short}$.

There were statistically significant differences in the sand, silt, silt + clay content, and VWC (10–15 cm, 20–25 cm) for the Philip and Brutsaert models. This suggests that the fitting of parameter K_{fs} was influenced by the soil texture and the drying of soil, which was related to the soil's water retention capacity. The K_{fs} value tends to be negative when the initial moisture content of soil is low and sand content is high. Significant differences were observed regarding the ratio of the late to initial infiltration rates (I_{late}/I_{ini}) for the Philip, Brutsaert, and Swartzendruber models. As mentioned above and in Figure 2-3, it was assumed that curve fitting of models failed by deformation of the infiltration curve due to decreased I_{late}/I_{ini} value caused by the change in the absorption capability of the soil as a result of drying.

Table 2-3 Differences in physical properties of soil and infiltration characteristics in tested fields where parameter K_{fs} was negative and nonnegative in Testshort (short-period infiltration test). The percentage contents of soil components and porosity are presented as the averages for three layers (0–5, 10–15, and 20–25 cm deep). VWC: volumetric water content, I_{ini} was calculated from the first reading, and I_{late} was calculated from the final reading, *n*: sample size, *significant at $p < 0.05$, **significant at $p < 0.03$, ***significant at $p < 0.01$, Neg: negative, NonNeg: nonnegative.

Physical properties of soil and infiltration characteristics	Mezencev			Philip and Brutsaert			Swartzendruber		
	Neg (n = 19)	NonNeg (n = 4)	p-value	Neg (n = 14)	NonNeg (n = 9)	p-value	Neg (n = 10)	NonNeg (n = 13)	p-value
Sand content (%)	54	65	0.177	61	48	0.045*	60	53	0.258
Silt content (%)	25	20	0.303	22	29	0.038*	22	26	0.340
Clay content (%)	21	14	0.007***	18	23	0.115	18	21	0.254
Silt + clay content (%)	46	35	0.177	39	52	0.045*	40	47	0.258
Porosity (%)	36	28	0.388	36	32	0.384	36	33	0.310
VWC (0–5 cm) ($cm^3\ cm^{-3}$)	0.19	0.14	0.273	0.17	0.20	0.506	0.18	0.18	0.985
VWC (10–15 cm) ($cm^3\ cm^{-3}$)	0.25	0.21	0.279	0.23	0.28	0.040*	0.23	0.26	0.240
VWC (20–25 cm) ($cm^3\ cm^{-3}$)	0.29	0.22	0.113	0.25	0.32	0.042*	0.27	0.28	0.786
Initial infiltration rate (I_{ini}) ($mm\ h^{-1}$)	644	616	0.935	813	369	0.093	830	492	0.201
Late infiltration rate (I_{late}) ($mm\ h^{-1}$)	30	22	0.709	15	49	0.054	14	39	0.057
I_{late}/I_{ini}	0.12	0.09	0.767	0.03	0.26	0.014**	0.02	0.19	0.014**

We analyzed the influence of initial (I_{ini}) and late infiltration rates (I_{late}) on the sign of K_{fs}. The target models were the same as the above, the I_{ini} was calculated from the first reading, and the I_{late} was calculated from the final reading in $Test_{short}$. The degree of influence of the value of I_{late}/I_{ini} on the determination of the sign of K_{fs} was verified in four models by discriminant analysis. The hit ratio, which was the percentage of each group correctly classified, was used as an indicator of the degree of influence. The results of the discriminant analysis with 23 samples are shown in Figure 2-5.

The hit ratio of the Mezencev model was 56%, of the Philip and Brutsaert models was 100%, and of the Swartzendruber model was 78%. For the Philip and Brutsaert models, this indicates that the I_{late}/I_{ini} value had a strong influence on the fitting and determination of the sign of parameter K_{fs}. As mentioned above in this section, for the Philip and Brutsaert models, it was concluded that curve fitting of models failed by deformation of the infiltration curve due to the decreased I_{late}/I_{ini} value.

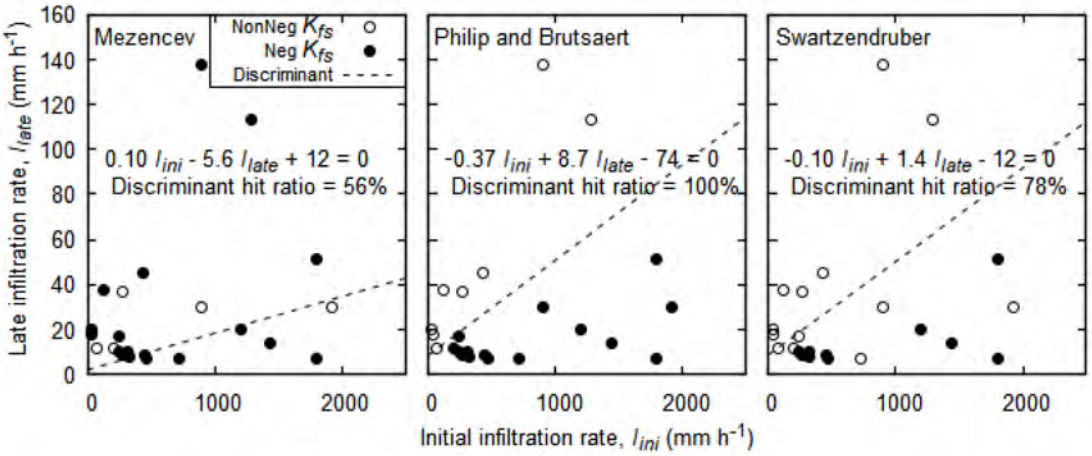

Figure 2-5 Discrimination analysis on the determination of the sign of K_{fs} in $Test_{short}$ (short-period infiltration test). The target models for this analysis were the Mezencev, Philip, Brutsaert, and Swartzendruber models, which provided negative K_{fs}. I_{ini} was calculated from the first reading and I_{late} was calculated from the final reading. Neg: negative, NonNeg: nonnegative.

2.3.6. Influence of difference in initial infiltration on the fitting of parameter K_{fs}

To determine how the initial infiltration period affected the fitting of parameter A_p, we analyzed the changes in the value of A_p (mm h^{-1}) of the Philip model that was obtained from differences in the initial infiltration period (mm) in $Test_{short}$. Figure 2-6 shows nine examples of changes in the value of A_p. The first value of A_p at rejection time (t) = 0 is fitted by the entire infiltration period, and the final value of A_p is fitted by the last four readings as the minimum infiltration period from t_{n-3} to t_n, where n is the total number of readings and t_n is the last time of reading. If the measured data are compatible with the predicted data of the Philip model, the plot line of A_p becomes horizontal, because the value of K_{fs} is constant regardless of the infiltration period. In three fields that gave a nonnegative value of A_p, DAR5, MTK3, and YZ1, it was shown that the influence of the initial infiltration period was not significant, and the regression lines of plotted A_p were nearly horizontal. This suggests that these measured data roughly matched the predicted data. On the other hand, in the other six fields that gave a negative value of A_p, it was found that initial infiltration did affect the fitting of parameter A_p. When the initial infiltration period was rejected, the value of A_p increased rapidly and became positive, except for field KC1. In DAR1, the value of A_p less the initial infiltration over 26 min became constant. It was considered that this infiltration period approximately fitted the prediction data and that this A_p might accurately represent the value of K_{fs}. However, A_p values of other fields did not become constant; therefore, it is necessary to find the optimal time of initial infiltration for best fitting and for obtaining appropriate K_{fs} values.

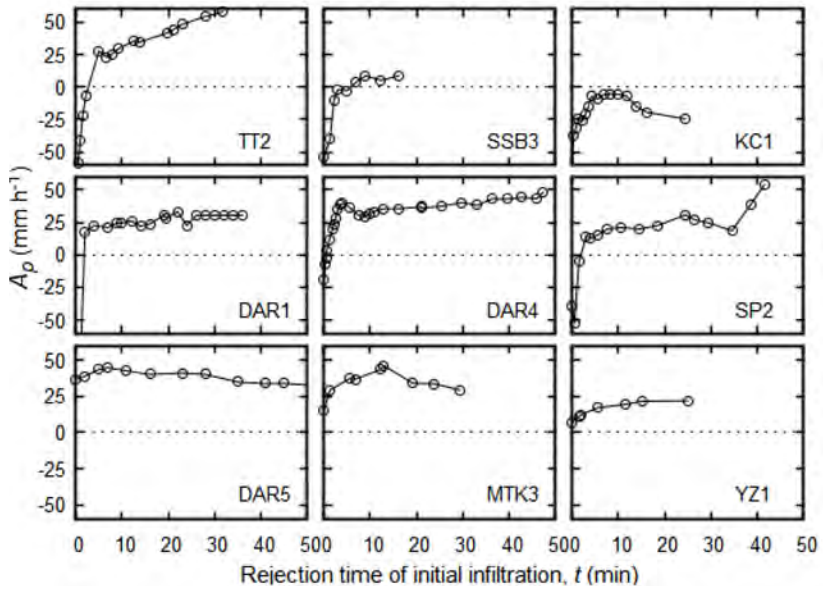

Figure 2-6 Changes in parameter A_p of the Philip model with differences in initial infiltration period in nine examples of $Test_{short}$ (short-period infiltration test). The characters with a number in the figure indicate the name of tested field.

2.3.7. Rejection of initial infiltration time for best fitting

The time of initial infiltration analyzed by Equation (2-9) that should be rejected for best fitting in nine examples of $Test_{short}$ are shown in Figure 2-7. The dotted lines (y = x) represent predicted data from the Philip model which shows the left-hand side and the right-hand side of Equation (2-9) are equal (RMSE = 0). $RMSE_{origi}$ lines represent the original infiltration data from t_1 at the time of first reading to t_n at the time of the final reading, and $RMSE_{mini}$ lines represent the data calculated for the infiltration time from t_a to t_n in which the RMSE value reached a minimum. The number (min) corresponds to the rejected time according to the $RMSE_{mini}$ calculation.

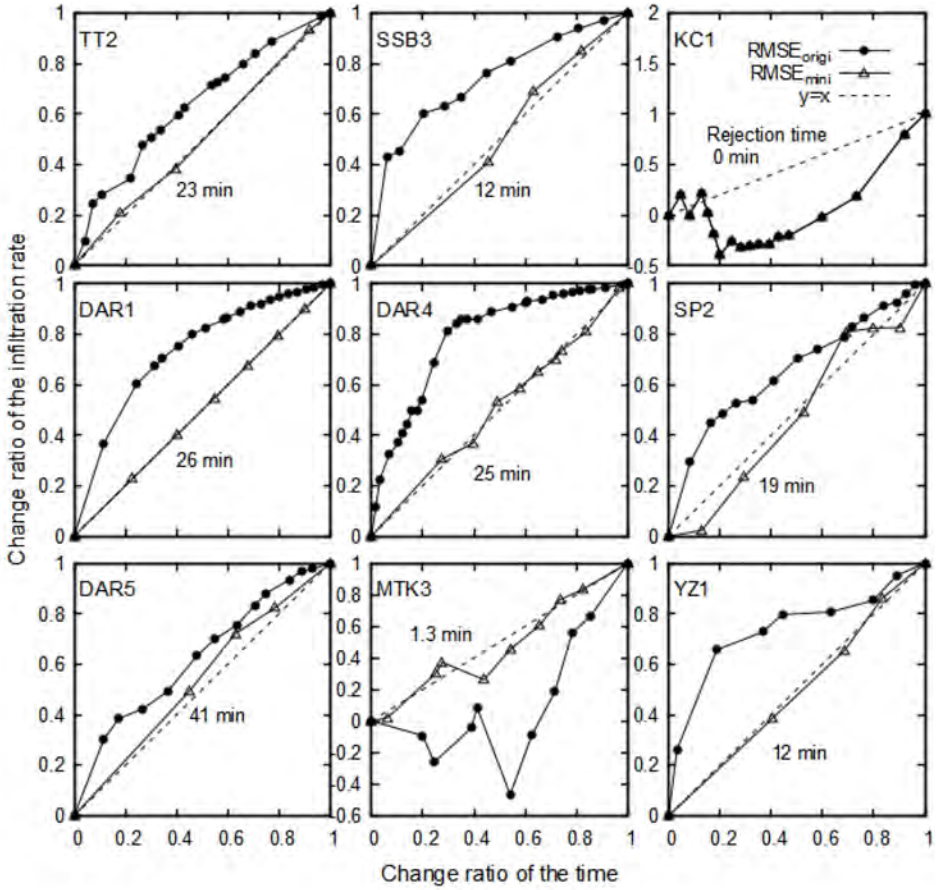

Figure 2-7 Rejection of initial infiltration time analyzed by Equation (2-9) for best fitting to the Philip model in nine examples of $Test_{short}$ (short-period infiltration test). $RMSE_{origi}$ is the value of RMSE calculated by the original measured data, and $RMSE_{mini}$ is the minimum value of RMSE using the data obtained by rejection the initial infiltration data. The number (min) in figures corresponds to the rejected time according to the $RMSE_{mini}$ calculation.

The results of four representative examples are as follows. DAR1 was a field in which the measured data were approximately matched to the predicted data by rejecting 26 min for initial infiltration. The value of $RMSE_{origi}$ was 0.248 and that of $RMSE_{mini}$ was zero. DAR1 was the only

field out of 23 fields in which the value of $RMSE_{mini}$ was zero. MTK3 was a field in which the measured data were roughly matched to the predicted data by rejecting 1.3 min for initial infiltration. The value of $RMSE_{origi}$ was 0.530 and that of $RMSE_{mini}$ was 0.084. DAR5 was a field in which the measured data roughly matched the predicted data regardless of the reduction of time for initial infiltration. The value of $RMSE_{origi}$ was 0.139 and that of $RMSE_{mini}$ was 0.063. KC1 was a field in which the measured data did not approximate the predicted data regardless of the reduction of time for initial infiltration. The values of both $RMSE_{mini}$ and $RMSE_{origi}$ were 0.498, which was the highest value for any of the tested fields. In two fields, KC1 and KC2, the measured data did not approximate the predicted data even when initial infiltration time was rejected.

2.3.8. Evaluation of revised K_{fs}

The parameter K_{fs} (A_p for Philip, A_s for Swartzendruber, A_b for Brutsaert, and f_0 for Mezencev model) was refitted with unconstrained conditions by using the infiltration time analyzed by Equation (2-9) for 21 fields in which we conducted $Test_{short}$, except for KC1 and KC2. For the Philip, Swartzendruber, and Brutsaert models, nonnegative K_{fs} parameters were obtained from all fields, but the Mezencev model gave a negative value in nine fields. Descriptive statistics of the value of the parameter K_{fs} (A_p, A_s, A_b, f_0, I_c for Horton model, and I_{cc} for corrected I_c) and reference K_{fsref}, are presented in Table 2-4 and Figure 2-8. The value of I_{cc} was calculated using the correction formula ($I_{cc} = 0.36 \times I_{c60}$), and we regarded the value of I_{cc} as the most appropriate among all the estimates. The value of A_p, A_s, and A_b estimates were similar, and I_{cc} were closed to reference K_{fsref}. The value of refitted A_p, A_s, A_b, and f_0 overestimated the K_{fs} value compared with I_{cc} and reference K_{fsref}. However, we found that refitted parameters (A_p, A_s, A_b, f_0) were correlated with the value of I_c and I_{cc}, and the determination coefficients (r^2) ($n = 21$) with I_{cc} were $A_p = 0.951$, $A_b = 0.932$, $A_s = 0.911$, and $f_0 = 0.607$. Based on the relationship between refitted parameters and I_{cc} values, each parameter could be presented as follows: $A_p = K_{fs}/0.50$, $A_b = K_{fs}/0.50$, $A_s = K_{fs}/0.52$, and $f_0 = K_{fs}/0.65$.

Table 2-4 Statistical description of the value of the parameter K_{fs} and reference K_{fsref} in $Test_{short}$ (short-period infiltration test). Sample size: n = 21 except for Mezencev (n = 12). Min: minimum, Max: maximum, SD: standard deviation, CV: coefficient of variation.

Model and equation, parameter K_{fs} (mm h^{-1})	Statistic				
	Mean	Min	Max	SD	CV (%)
Philip, A_p	28	2.5	128	29	104
Swartzendruber, A_s	27	2.6	128	30	111
Brutsaert, A_b	28	2.3	128	29	104
Mezencev, f_0	28	0.4	113	31	109
Horton, I_c	40	6.0	149	38	94
Horton, corrected I_c (I_{cc})	15	2.2	54	14	94
Reynolds, reference K_{fsref}	18	4.3	80	20	112

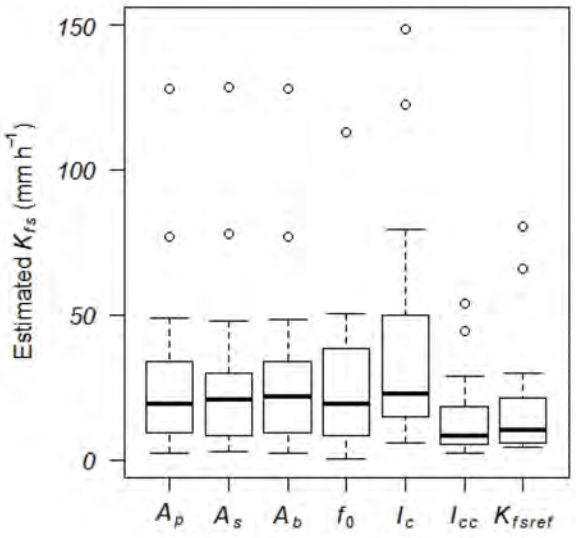

Figure 2-8 Box plots (sample minimum, first quartile, median, third quartile, maximum, outlier) of estimated K_{fs} in $Test_{short}$ (short-period infiltration test). The targets K_{fs} were A_p for Philip, A_s for Swartzendruber, A_b for Brutsaert, f_0 for Mezencev, I_c for the Horton model, I_{cc} for the corrected I_c, and reference K_{fsref} for the Reynolds equation. Sample size: n = 21 except for Mezencev (n = 12).

2.4. Conclusions

The fitting performance and estimates of parameter K_{fs} of five infiltration models were evaluated to select a suitable model matched to the conditions of tested fields, as popular models such as the Philip model often produced negative K_{fs} values. The results showed that Horton was the most useful model; fitting quality was good, and nonnegative values of K_{fs} were estimated in all tested fields, although it tended to overestimate K_{fs} in short-period tests. The empirical model of Mezencev exhibited the highest fitting performance but often gave negative K_{fs} values. The physically based models of Swartzendruber and Brutsaert performed similarly; they had a slightly higher fitting performance than the Philip model and gave negative K_{fs} values in short-period tests, as did the Philip model. The Philip, Swartzendruber, Brutsaert, and Mezencev models using constrained curve fitting to obtain nonnegative K_{fs} lowered in fitting quality.

The physical factors of the soil that gave negative K_{fs} values were analyzed statistically, and the main factor at play was found to be deformation of the infiltration curve due to the magnitude of initial infiltration caused by drying of the soil. We demonstrated a method of obtaining nonnegative K_{fs} values by rejecting an initial infiltration period calculated by improving the cumulative linearization approach of the Philip model. However, the revised K_{fs} was overestimated relative to reference values, so the correction formula for applying the revised K_{fs} was taken from the relationship between the revised K_{fs} and I_c of the Horton model.

Chapter 3. Measurement of evapotranspiration

Data Features for the Rejection of Bowen Ratio Fluxes

3.1. Introduction

An accurate estimation of the evapotranspiration (*ET*) that occurs in fields is required to determine the amount of irrigation water, water management, and the effective use of water resources. Various methods exist to measure and estimate the actual amount of *ET*. The standard method for direct *ET* measurements has been the use of weighing lysimeters. Although previous studies considered lysimeters as the most accurate method to assess *ET*, installation and operational costs are expensive. Also, they are typically considered research devices that are not practical for irrigation planning [70]. In the last decades, the eddy covariance has been increasingly used for micrometeorological studies of surface fluxes [71]. This method utilizes surface fluxes that are mixed in the atmosphere near the surface via turbulence [72]. However, measuring instruments, such as a three-dimensional sonic anemometer, are quite expensive and challenging to install in developing countries because of the required continuous maintenance and security purposes. An alternative to lysimetric measurements and the eddy covariance method is the Bowen ratio energy balance (BREB) method [23]. It is widely used to directly estimate *ET* because of its clear physical concept, simple formula, simple data collection, and inexpensive measuring instruments. This method is based on the theory that one-dimensional fluxes of sensible heat and latent heat can be described in terms of flux–gradient relationships:

$$H = -\rho C_p K_h \frac{\partial T}{\partial z} \quad , \quad lE = -\frac{\rho C_p}{\gamma} K_E \frac{\partial e}{\partial z} \tag{3-1}$$

Table 3-1 defines the symbols that appear in all equations in this study. For the sign convention, *lE* and *H* are positive upward, with direction the same as the negative gradients of the air temperature and water vapor pressure (Figure 3-1). The turbulent diffusion coefficients of sensible heat (K_h) and latent heat (K_E) are assumed to be equal in Equation (3-1), and the Bowen ratio (β) is defined as follows:

$$\beta = \frac{H}{lE} = \gamma \frac{T_1 - T_2}{e_1 - e_2} = \gamma \frac{\Delta T}{\Delta e} \tag{3-2}$$

ΔT and Δe are obtained by measuring air temperature and water vapor pressure or dew point at two heights above the top of the canopy within the boundary layer.

The equation of latent heat flux based on the energy balance in Equation (3-3) is as follow:

$$R_n = H + lE + G + \Delta W \tag{3-3}$$

$$lE = \frac{R_n - G - \Delta W}{1 + \beta} \tag{3-4}$$

For the sign convention, energy fluxes R_n, G, and ΔW are positive downward, with direction opposite to the air temperature and water vapor pressure of gradients, lE and H (Figure 3-1). We applied the change in the stored heat energy flux of water (ΔW) for the paddy field scenario to improve the energy balance calculation accuracy. There are no studies that consider ΔW in determining the rejection of the BREB calculation fluxes. Positive ΔW values represent the amount of heat flux consumed to raise the water temperature, whereas negative values indicate the amount of heat flux generated to reduce the water temperature. Section 3.2 describes the equation used to calculate ΔW. However, the BREB method has a large number of assumptions and constraints. Thus, this method often produces unacceptable sensible and latent heat fluxes in practical situations based on the following inherent problems.

The first problem is that the BREB yields a significantly inaccurate flux magnitude due to the fact that when the Bowen ratio (β) approaches −1, the denominator in the BREB formula is $1 + \beta$. When β is exactly −1, it is not possible to calculate the fluxes. At sunrise and sunset [73], as well as at midday and early afternoon with exposure to cloudy conditions [74], the β value approaches −1. Several previous studies have defined a fixed interval in which the β values are near −1, for example, $\beta < -0.75$ or $-1.3 < \beta < -0.7$ [75, 76]. The problems associated with β as it approaches −1 depend on the measurement accuracy and resolution limits of the sensors used were pointed out [77]. The reduction of the occurrence of this problem requires an increase in the accuracy of the thermo-hygrometers was suggested [24].

The second problem is that the BREB method yields the incorrect signs (directions) for the heat fluxes opposite to the observed vertical differences in the air temperature/water vapor pressure. For example, the signs or directions of the calculated latent flux may be positive or upward (evaporation), but the observed differences in water vapor pressure are negative or downward (condensation). This problem are frequently encountered in the early morning, in the late afternoon, during precipitation events, and at nighttime [78], as well as when wind speed is less than 0.07 m s^{-1} due to poor turbulent development [79] and condensing events.

There are few papers that deal with the data using the BREB method for checking. For example, [77] proposed objective criteria for unacceptable fluxes derived from instrument resolution limits and physical considerations. [80] reported four conditions when the BREB method fails, which are associated with the available energy flux, vapor pressure difference, Bowen ratio, and heat fluxes. [81] and [82] discussed the criteria for rejecting inaccurate data and rejection procedures. The data subsets that require rejection depend on the climatic characteristics,

surface conditions of the observation site, and sensor conditions. However, few previous studies have commented on the influence of the differences in observation conditions with respect to the rejection parameters. However, the specific meteorological conditions that cause these problems are poorly understood. Therefore, the aim of this study is to understand the data features and the meteorological conditions when the BREB method fails. We used the dataset observed from six agricultural fields over three seasons in Myanmar, where no previous research has been conducted regarding measuring ET and energy fluxes in agricultural fields.

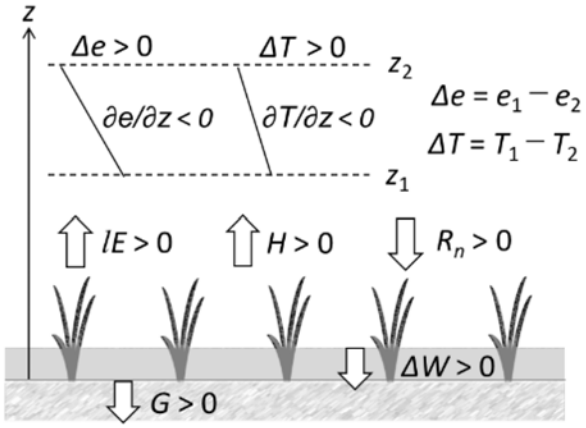

Figure 3-1. A representation of the energy fluxes at the interface between the air and the surface in a paddy field as indicated by the arrows (modified after [15]). The parameter R_n is the net radiation, lE is the latent heat flux, H is the sensible heat flux, G is the surface soil heat flux, ΔW is the change in the stored heat energy flux of ponded water, Δe and ΔT are the water vapor pressure and air temperature differences between heights Z_1 and Z_2, and $\partial e/\partial Z$ and $\partial T/\partial Z$ are the corresponding water vapor pressure and air temperature gradients, respectively.

Table 3-1 A list of the symbols and variables in the equations, figures, and their definitions.

Symbol	Units	Description
ET	mm h^{-1}	Evapotranspiration rate
H	W m^{-2}	Sensible heat flux
lE	W m^{-2}	Latent heat flux
B	–	Bowen ratio
R_n	W m^{-2}	Net radiation
G	W m^{-2}	Soil heat flux
ΔW	W m^{-2}	Change in the stored heat energy flux of water
P	kg m^{-3}	Mean air density
C_p	kJ kg^{-1} °C^{-1}	Specific heat capacity of air at constant pressure (approximately 1.01)
Γ	kPa °C^{-1}	Psychrometric constant (approximately 0.066)
K_h and K_E	m^2 s^{-1}	Turbulent diffusion coefficients of sensible heat and latent heat
K	m^2 s^{-1}	$K = K_h = K_E$
Z	M	Profile height difference
h_i	M	Height of the sensor above the ground
T_i	°C	Air temperature at h_i
RH_i	%	Relative humidity at h_i
e_i	kPa	Water vapor pressure at h_i calculated from T_i and RH_i
$\partial T/\partial z$ and $\partial e/\partial z$	–	Air temperature and water vapor pressure gradients between two heights
$\Delta\theta$	°C	Equivalent profile air temperature difference ($\Delta T + \Delta e/\gamma$)
ΔT and Δe	°C and kPa	Differences in observed value of T and e between two heights
δT and δe	°C and kPa	Differences in true value of T and e between two heights
E_T and E_e	°C and kPa	Resolution limits for air temperature and water vapor pressure measurements
E_θ	°C	Resolution limit in equivalent temperature ($E_T + E_e/\gamma$)
C_W	J m^{-3} °C^{-1}	Volumetric heat capacity of water
d_w	M	Ponded water depth
$T_{w(t)}$	°C	Temperature of ponded water at time t
Δt	S	Differences in time of observed temperature of ponded water

3.2. Data rejection

3.2.1. Objective criteria

The inherent problem of the BREB method arises when β approaches −1 because of the denominator in Equation (3-4) and yields the sensible/latent heat fluxes with incorrect signs (directions) inconsistent with the observed gradients of the air temperature/water vapor pressure. Criteria based on [77] derived from instrument resolution limits and physical consideration for determining objectively the unacceptance fluxes were as follows:

3.2.2. Criteria for data with the Bowen ratio approaching −1

If β approaches −1 in Equation (3-2), the equivalent profile air temperature difference $\Delta\theta$ (℃) can be defined as follows:

$$\Delta\theta = \Delta T + \Delta e/\gamma = 0 \tag{3-5}$$

The conditions that satisfy $\beta = -1$ are $\Delta T = \Delta e/\gamma = 0$ and $\Delta T = -\Delta e/\gamma$. The field conditions that satisfy these conditions in practice, however, are unclear. The feature where β approaches −1 is associated with the measurement accuracy and resolution limits of the thermo-hygrometers. The measurement resolution limits with respect to the air temperature and water vapor pressure are denoted as E_T and E_e, respectively. The relationship between the true air temperature difference, δT, and the observed air temperature difference, ΔT, can be expressed as follows:

$$\Delta T - 2E_T < \delta T < \Delta T + 2E_T \tag{3-6}$$

Similarly, for water vapor pressure, the following relationship can be obtained:

$$\Delta e - 2E_e < \delta e < \Delta e + 2E_e \tag{3-7}$$

By substituting Equations (3-6) and (3-7) into Equation (3-5), the following relationship can be obtained:

$$\Delta T - 2E_T + (\Delta e - 2E_e)/\gamma < \delta\theta < \Delta T + 2E_T + (\Delta e + 2E_e)/\gamma \tag{3-8}$$

When $\beta = -1$, $\delta\theta = 0$ and the resolution limit in equivalent temperature can be defined as $E_\theta = E_e/\gamma + E_T$; therefore, the following relationship can be obtained:

$$-\Delta e/\gamma - 2E_\theta < \Delta T < -\Delta e/\gamma + 2E_\theta \tag{3-9}$$

By combining Equatoin (3-2) and (3-9), the criterion for the range of β that yields significantly inaccurate flux magnitudes due to the fact that β approaches −1 can be obtained:

$$-1 - 2\gamma E_\theta < \beta < -1 + 2\gamma E_\theta \tag{3-10}$$

3.2.3. Criteria for data with incorrect sign of fluxes

This problem is a physical paradox due to the direction of the calculated sensible (or latent) heat fluxes and the fact that the vertical differences in the observed air temperature (or water vapor pressure) are opposite. This criterion equation can be expressed by combining Equation (3-2) and (3-3):

$$\Delta e/lE = \gamma\Delta T/H = \gamma\Delta\theta/(R_n - G - \Delta W) < 0 \quad (3\text{-}11)$$

The assumption of the BREB method is that the sign of both $R_n - G - \Delta W$ and $\gamma\Delta\theta$ must be identical. Thus, the cases for rejection occur when $\gamma\Delta\theta > 0$ and $R_n - G - \Delta W < 0$ or $\gamma\Delta\theta < 0$ and $R_n - G - \Delta W > 0$ based on the Equation (3-11). It is unclear which condition often occurs in practical applications, and the magnitude of the measurement errors for the available energy flux and air temperature and water vapor pressure differences is related to this problem.

The latent and sensible heat fluxes can be calculated based on the product of the turbulent diffusion coefficient ($K = K_E = K_h$), air temperature/water vapor pressure differences, and several physical constants from Equation (3-1). The signs of the sensible/latent heat fluxes and air temperature/water vapor pressure differences must be identical. In other words, this problem yields a negative turbulent diffusion coefficient ($K < 0$) owing to measurement errors and resolution limits of the sensors, resulting in a physical paradox.

3.2.4. Meteorological conditions when the BREB method fails

Table 3-2 shows the rejection type classified by meteorological conditions which were derived from the earlier mentioned objective criteria modified after [80].

Table 3-2 Rejection type when the BREB method fails classified by meteorological conditions (modified after [80])

Rejection type	Meteorological conditions			
A	$R_n - G - \Delta W > 0$	$\beta < -1 + 2\gamma E_\theta/\Delta e$	$\Delta e > 0$	$\Delta T > 0$
B				$\Delta T < 0$
C		$\beta > -1 + 2\gamma E_\theta/\Delta e$	$\Delta e < 0$	$\Delta T > 0$
D				$\Delta T < 0$
E	$R_n - G - \Delta W < 0$	$\beta > -1 - 2\gamma E_\theta/\Delta e$	$\Delta e > 0$	$\Delta T > 0$
F				$\Delta T < 0$
G		$\beta < -1 - 2\gamma E_\theta/\Delta e$	$\Delta e < 0$	$\Delta T > 0$
H				$\Delta T < 0$

The symbols in meteorological conditions are defined in Table 3-1. $R_n - G - \Delta W$ denotes the available energy flux, and $2\gamma E_\theta/\Delta e$ is twice the resolution limits in equivalent water vapor pressure with dimensionless quantity.

3.3. Materials and Methods

3.3.1. Study site and observation conditions

Figure 3-2 shows the location of the study site and micrometeorological equipment used. Micrometeorological observations were conducted at the experimental fields (latitude: 19.8°; longitude: 96.3°) of the Department of Agricultural Research, Ministry of Agriculture, Livestock and Irrigation, Myanmar, located in Zayarthiri Township in the Naypyidaw Union Territory at an elevation of 100 m above mean sea level. The area has a moderate monsoon climate with an average annual rainfall of 1,100 mm, where approximately 75% of the precipitation occurs during the monsoon season (i.e., between June and September). The soil texture of the fields at the study site is mainly sandy loam and clay loam. Tthe physical properties of the soil in these fields were described in the Section 3.2.

Table 3-3 lists the observed conditions and periods of data analysis. Observations were taken from six agricultural fields growing five crops (rice, sunflower, sesame, maize, and groundnut) over three seasons (dry, monsoon, and post-monsoon). For the data analysis, the monsoon and post-monsoon seasons were segmented into first (early) and second (late) half periods. The analysis periods were from after planting or sowing to before harvesting, and the crop heights were recorded at the beginning and end of the analysis period. Irrigated fields were used for paddy rice during the dry season (PrD), paddy rice during the late monsoon (PrM_2), and sesame during the dry season (SsD). For the SsD, the amount of irrigation was 185 mm, and the frequency was five times. These measurements were not recorded for the paddy fields (PrD and PrM_2). Maize cultivation in the early monsoon (MzM_1) was stopped on July 15, 2018, because of heavy rain, but meteorological observations continued.

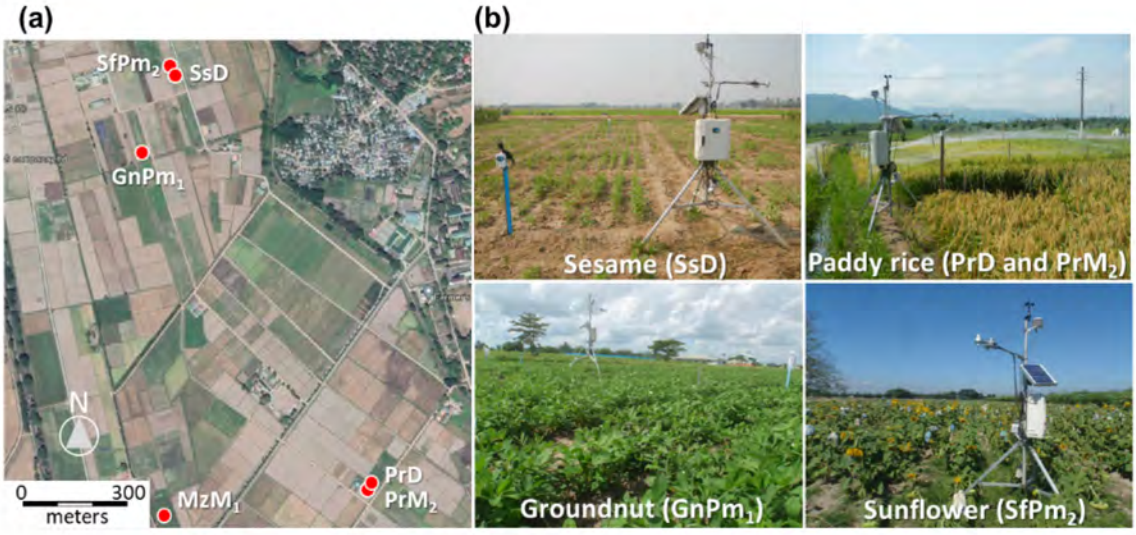

Figure 3-2. (a)The location of observation site showing (b) the micrometerological observation station in agricaltural experiment fields.

Table 3-3 Observation conditions for the flux calculations. The periods are from after planting or sowing to before harvesting, and the crop heights were recorded at the beginning and the end of the peirod.

Crops	Seasons	Periods (84 days)	Abbreviation	Crop height (m)
Paddy rice	Dry	Feb 4–Apr 28 (2017)	PrD	0.15–0.94
Sesame	Dry	Feb 4–Apr 28 (2018)	SsD	0.03–1.10
Maize	Early monsoon	Jun 7–Aug 29 (2018)	MzM_1	0.20–1.50
Paddy rice	Late monsoon	Aug 1–Oct 23 (2017)	PrM_2	0.15–0.86
Groundnut	Early post-monsoon	Sep 14–Dec 6 (2018)	$GnPm_1$	0.09–0.40
Sunflower	Late post-monsoon	Nov 8 (2017)–Jan 30 (2018)	$SfPm_2$	0.07–1.00

3.3.2. Observation data for the BREB method

A tripod micrometeorological station was installed with a height of 2.8 m that can be easily relocated for observation in different fields. There were seven elements of micrometeorological observations. The net radiation was calculated based on the sum of the shortwave/long-wave radiation with the upward/downward directions observed using solar radiometers (PCM-01NB-L3CS, PREDE Co, Tokyo, Japan) for the shortwave radiation with output accuracy of ±3% and infrared radiometers (PRI-01B-L3CS, PREDE Co, Tokyo, Japan) for the long-wave radiation with the output accuracy of ±5%. The soil heat flux was recorded using a heat flux sensor (PHF02-L5CS, PREDE Co, Tokyo, Japan), and the wind speed was obtained using an anemometer (03101Y-L3CS, RM Young, Traverse, Michigan, USA) at a height of 2.8 m. The measurement of dew-point temperature is common in the estimation of water vapor pressure on the BREB method. However, we estimated the water vapor pressure using the values of air temperature and relative humidity observed using thermo-hygrometers (i.e., air temperature and capacitive relative humidity sensor instrument) (HMP110, Vaisala, Helsinki, Finland) with multiplate radiation shields (FP1806, Field Pro, Tokyo, Japan) because a simplified observation system was required in Myanmar. Many previous studies on the BREB method also used a capacitive humidity sensor as an alternative to a dew-point hygrometer [116]. [82] showed a reasonable agreement between the BREB method using a thermo-hygrometer and that substituted with dew-point hygrometer with magnitudes of error at most 2% for relative humidity and 0.3℃ for air temperature. For relative humidity, the accuracy of HMP110 is ±1.5% in the range of 0–90% and ±2.5% in the range of 90–100%, and for air temperature, the accuracy of HMP110 is ±0.2℃ in the range of 0–40℃ and ±0.4℃ in the range of 40–80℃. Hence, the use of the HMP110 is adequate except for high-temperature condition.

For installation heights for thermo-hygrometers, h_1 was from 0.5 to 1.5 m for the paddy rice, sunflower, and maize fields depending on crop heights, while other crops with low plant height had a fixed height of 1.0 m. Height h_2 was at 2.5 m for all crops. For the change in the stored heat energy of water (ΔW) in paddy fields exposed to flooding conditions, the capacitance sensor, which was installed near the meteorological station, was used to measure the ponded water

depth, d_w, and water temperature, $T_w(t)$, at time t with a data logger (WT-VO250, TruTrack, Christchurch, New Zealand). The parameter ΔW was calculated with the following equation:

$$\Delta W = C_w d_w \frac{\partial T_w}{\partial t} = C_w d_w \frac{T_{w(t+1)} - T_{w(t)}}{\Delta t} \quad (3\text{-}12)$$

For the meteorological observation data, an average 10 min interval sampling value was based on a 10 s sampling recorded by the data logger (CR1000, Campbell Scientific, Logan, UT, USA). The water level and temperature for ΔW were recorded at 30 min intervals. In this study, the data used to determine rejection were the hourly values, which were the averages of the corresponding six 10 min interval values of the meteorological data and two 30 min interval values for ΔW. For preliminary analysis, we compared the rejection rate of the calculated fluxes using 30 min and 60 min interval values based on the criteria of Equation (3-10) and (3-11), but the result of both intervals was nearly identical.

3.3.3. Thermo-hygrometer resolution limits

The measurement resolution limits, which depend on the sensor and data logger, are necessary to be determined if the data require rejection using the objective criteria. Common thermo-hygrometers have no specifications on the resolution limits because they are analog signal output devices. The aforementioned previous studies have estimated the resolution limits based on the accuracy and error magnitude of the measurement used [24, 78, 80], despite differences between the resolution limit and the accuracy of the sensor. In this study, the resolution limits were set to a theoretical value calculated using the range of the data logger arithmetic processing as follows: the bit number of the data logger CR1000 was 13 bits (2^{13} = 8,192), the available range of input voltage in the logger was ±2500 mV, and the minimum input value corresponding to the resolution limit was 5000 mV/8192 = 0.61 mV, which converts to 0.06°C for the thermometer and 0.005 kPa for the hygrometer. In previous studies, for example, the estimated values of the resolution limit for temperature and water vapor pressure were 0.01°C and 0.01 kPa in [80], 0.07°C and 0.05 kPa in [78], and 0.1°C and 0.04 kPa in [24], respectively.

3.3.4. Characteristics of unacceptable data

First, we compared the hourly median value of each meteorological element in the period of time when $R_n \geq 0$ and $R_n < 0$ to understand the differences in the meteorological characteristics for each observation. Secondly, we examined the hourly rejection frequencies during the observation period using objective criteria for unacceptance data with Bowen ratios approaching −1 and with incorrect flux signs based on Equations (3-10) and (3-11) to clarify the data features that require rejection.

3.4. Results and Discussion

3.4.1. Meteorological characteristics of each observation

Table 3-4 lists the meteorological observation values in the time when $R_n \geq 0$ and $R_n < 0$ (i.e., daytime and nighttime) for each observation. The sample size of each observation was 2016 for 84 days, with data descriptions for the hourly median values except for rainfall and $lE < 0$; that is, the rainfall was the total amount, and $lE < 0$ was a percentage of the data that had a negative lE value.

The available energy flux at the surface ($R_n - G - \Delta W$) when $R_n < 0$ during the monsoon (MzM_1 and PrM_2) was more than 0 W m^{-2} due to the downward infrared radiation (i.e., radiant heat by atmosphere). As the results, air temperature did not easily drop and the values of ΔT and Δe were small, and $\Delta\theta$ was nearly zero, where MzM_1 was closest to zero. The meteorological conditions at MzM_1 during the night indicate that the Bowen ratios tend to approach −1 based on the Equation (3-5). In the PrD at the time of $R_n < 0$, the majority of the calculated latent heat fluxes (95%) had negative values under the condition with large Δe and ΔT, since the ground surface of paddy field was ponded with exposure to the night dry air, and condensation could likely occur due to cooling effect of surface temperature at nighttime. In the majority of the observation conditions during the time of $R_n < 0$, the ΔT values were negative and the wind speed characterizes a slight breeze, which indicates that surface air was less likely to move vertically and maintains stable conditions at the surface. It may affect evaluations of the BREB method, which requires the measurement of ΔT and Δe, due to decreased turbulent development.

Table 3-4 Meteorological observation values of each period in the time when $R_n \geq 0$ and $R_n < 0$.

Elements	Units	Period of time when $R_n \geq 0$							Period of time when $R_n < 0$						
		Dry		Monsoon		Postmonsoon			Dry		Monsoon		Postmonsoon		
		PrD	SsD	MzM_1	PrM_2	$GnPm_1$	$SfPm_2$	All	PrD	SsD	MzM_1	PrM_2	$GnPm_1$	$SfPm_2$	All
Sample size		846	828	1021	968	863	803	5329	1170	1188	995	1048	1153	1213	6767
R_n	W m^{-2}	390	392	228	322	360	315	332	−69	−72	−10	−13	−49	−60	−48
G	W m^{-2}	28	71	13	16	36	58	30	−30	−32	−17	−19	−32	−24	−25
ΔW	W m^{-2}	0	Na	na	12	na	na	1	−2	na	na	−6	na	na	−3
$R_n - G - \Delta W$	W m^{-2}	351	300	215	274	297	224	274	−28	−39	8	12	−17	−36	−21
T_2	℃	32	32	28	29	30	28	30	23	23	26	26	24	21	25
RH_2	%	49	49	82	78	69	61	70	76	76	92	93	92	88	84
e_2	kPa	2.0	2.2	3.2	3.3	2.9	2.2	2.9	2.0	2.1	3.0	3.1	2.8	2.1	2.6
ΔT	℃	−0.10	1.0	0.25	−0.07	0.30	0.49	0.22	−0.40	−0.88	−0.05	0	−0.19	−0.28	−0.20
ΔRH	%	2.7	−0.54	0.32	1.7	0.59	−0.11	0.61	3.4	5.2	0.63	0.53	2.0	1.7	1.8
Δe	kPa	0.11	0.09	0.06	0.06	0.07	0.05	0.07	0.05	0.04	0.01	0.02	0.03	0.01	0.02
Wind speed	m s^{-1}	1.7	1.4	2.3	1.4	1.5	1.6	1.7	0.3	0.3	1.3	0.01	0.4	0.3	0.4
$\Delta\theta$	℃	1.6	2.4	1.2	0.73	1.4	1.3	1.4	0.33	−0.15	0.10	0.30	0.22	−0.14	0.15
$\gamma\Delta\theta$	kPa	0.11	0.16	0.078	0.048	0.096	0.088	0.092	0.022	−0.010	0.006	0.020	0.015	−0.009	0.010
Rainfall	mm	na	2	320	320	47	11	700	na	23	264	673	115	50	1125
Rate of $lE < 0$	%	0.5	1	0.4	7	1	2	2	95	54	29	27	63	67	56

The sample size of each observation was 2016 for 84 days. Hourly median values except for rainfall and $lE < 0$ are described, rainfall denotes the total amount, and the rate of $lE < 0$ refers to the percentage of the data that have negative lE values. $\Delta\theta$ is $\Delta T + \Delta e/\gamma$ and $\gamma\Delta\theta$ is $\gamma\Delta T + \Delta e$. Na denotes not available or without observation. The abbreviations of each observation period representing seasons and crops are defined in Table 3-3.

1.1.1. Data feature when the BREB method fails

Table 3-5 lists the rejection rates for the rejection types based on Equations (3-10), (3-11), and Table 3-2. Figure 3-4 shows the rejection frequency rates (per hour) in the day for each observation, with a sample size in each observation of 2016 for 84 days. As shown in Table 3-5, the total rejection rates of each observation, which satisfy the objective criteria that include the inaccurate flux magnitudes when β approaches −1 ($\beta = -1$) or the incorrect flux sign opposite to the gradients of air temperature/water vapor pressure ($K < 0$), were 56% for PrD, 49% for MzM_1, 40% for $SfPm_2$, 40% for PrM_2, 37% for $GnPm_1$, and 33% for SsD. Approximately 30% of the rejection data for each observation duplicated rejection type of $\beta = -1$ and $K < 0$. The rejection frequency varied depending on the observation conditions, but the majority of the rejections likely occurred during the nighttime (Figures 3-4ab). The percentage of nighttime rejection (from 18:00 to 6:00) to the total rejection for the PrD, SsD, MzM_1 PrM_1, $GnPm_1$, and $SfPm_2$ were 98%, 53%, 88%, 58%, 61%, and 59%, respectively. Most of the nighttime data in PrD were unacceptance, which should be related to the highest frequency rate of yielding $lE < 0$ (95%) shown in Table 3-4, that is, condensation condition in the time when $R_n < 0$.

As shown in Figure 3-4a, the frequent occurrences of rejection were (1) for $\beta = -1$ from 22:00 to 6:00 for the MzM_1 and (2) for $K < 0$ from 18:00 to 6:00 for the PrD and from 17:00 to 18:00 at sunset for PrD and $SfPm_2$. The highest rejection rate for $\beta = -1$ was the MzM_1, which is 46% (Table 3-5 and Figure 3-4a). The relationship between ΔT and Δe in which Bowen ratio approaches −1 for the MzM_1 would be satisfied because $\Delta T \cong \Delta e/\gamma \cong 0$ (Table 3-4). On the other hand, the lowest rejection rate for $\beta = -1$ was the SsD (19%) having large values of ΔT and Δe; in this case, the relationship between ΔT and Δe when β approaches −1 would be satisfied because $\Delta T \cong -\Delta e/\gamma$. It suggests that the rejection for $\beta = -1$ associated with the measurement error due to the resolution limits of thermo-hygrometer is less likely to occur in the seasons when the difference in the air temperature and water vapor pressure is large. The highest rate for $K < 0$ was the PrD, which is 47% (Table 3-5), having the highest value of Δe (Table 3-4). Since the available energy flux ($R_n - G - \Delta W$) at the nighttime naturally has a negative value, thus, based on the Equation (3-11), the conditions that yielded incorrect flux signs ($K < 0$) at the night must be the satisfaction of the condition $\gamma\Delta\theta > 0$ (or $\Delta e > -\gamma\Delta T$). Thus, the conditions of the PrD contributed the determination of $\gamma\Delta\theta > 0$; that is, the flooded ground surface exposed to a dry atmosphere under the negative available energy flux resulted in $\gamma\Delta\theta > 0$, because the value of Δe became highly positive and ΔT easily yielded small negative values. Similarly, we assumed that changes in the amount of surface soil moisture during the dry season due to the irrigation supply and rainfall influence the increase in $\gamma\Delta\theta$ positively, which yield fluxes with incorrect sign. On the other hand, for the SsD with the same season as the PrD, the rejection rate of $K < 0$ was low (22%) as shown in Table 3-5 with the highest negative value of ΔT at nighttime. The magnitude of the negative ΔT value due to the effect of ground surface cooling during the night could have forced

the value of $\gamma\Delta\theta$ to a negative value.

The majority of rejection on the meteorological elements was F condition (i.e., $R_n - G - \Delta W < 0$, $\beta > -1 - 2\gamma E_\theta/\Delta e$, $\Delta e > 0$, and $\Delta T < 0$) for the observations except for the monsoon (Table 3-5 and Figure 3-4b). This could be a result of the condensation condition due to fact that ΔT was negatively large under the high humidity and stable condition in the nighttime (Table 3-4). For the monsoon, the rejection occurrence was multiple conditions (i.e., A, B, E, and F conditions), which may be a result of the fact that the rainfall and small air temperature/relative humidity difference affected the rejection determination. In other words, the BREB method during the monsoon could be susceptible to measurement errors and resolution limits with respect to the use of a specific instrument.

Table 3-5 The rejection rates (%) based on the rejection types with Bowen ratio approaching −1 and with incorrect flux sign defined by (10) and (11) and classified by meteorological conditions presented in Table 3-2.

Rejection types	Dry		Monsoon		Post-monsoon		All
	PrD	SsD	MzM_1	PrM_2	$GnPm_1$	$SfPm_2$	
$\beta = -1$	27	19	46	30	21	31	29
$K < 0$	47	22	18	17	27	22	26
$\beta = -1$ and $K < 0$	18	8	15	8	11	13	12
$\beta = -1$ or $K < 0$	56	33	49	40	37	40	43
A	0	0	7	11	0	1	3
B	3	2	25	12	5	4	9
C	0	0	1	0	0	0	0
D	0	0	4	0	1	1	1
E	1	3	1	6	1	4	3
F	51	28	10	11	30	28	26
G	0	0	0	0	0	0	0
H	1	0	1	0	0	2	1

$\beta = -1$: significantly inaccurate flux magnitudes when Bowen ratio approaches −1. $K < 0$: incorrect flux direction opposite to the observed air temperature/water vapor pressure gradients. Alphabets for rejection of meteorological conditions are defined in Table 1. Sample size for each condition was 2016 hourly data for 84 days. The abbreviations for the observation conditions are defined in Table 3.

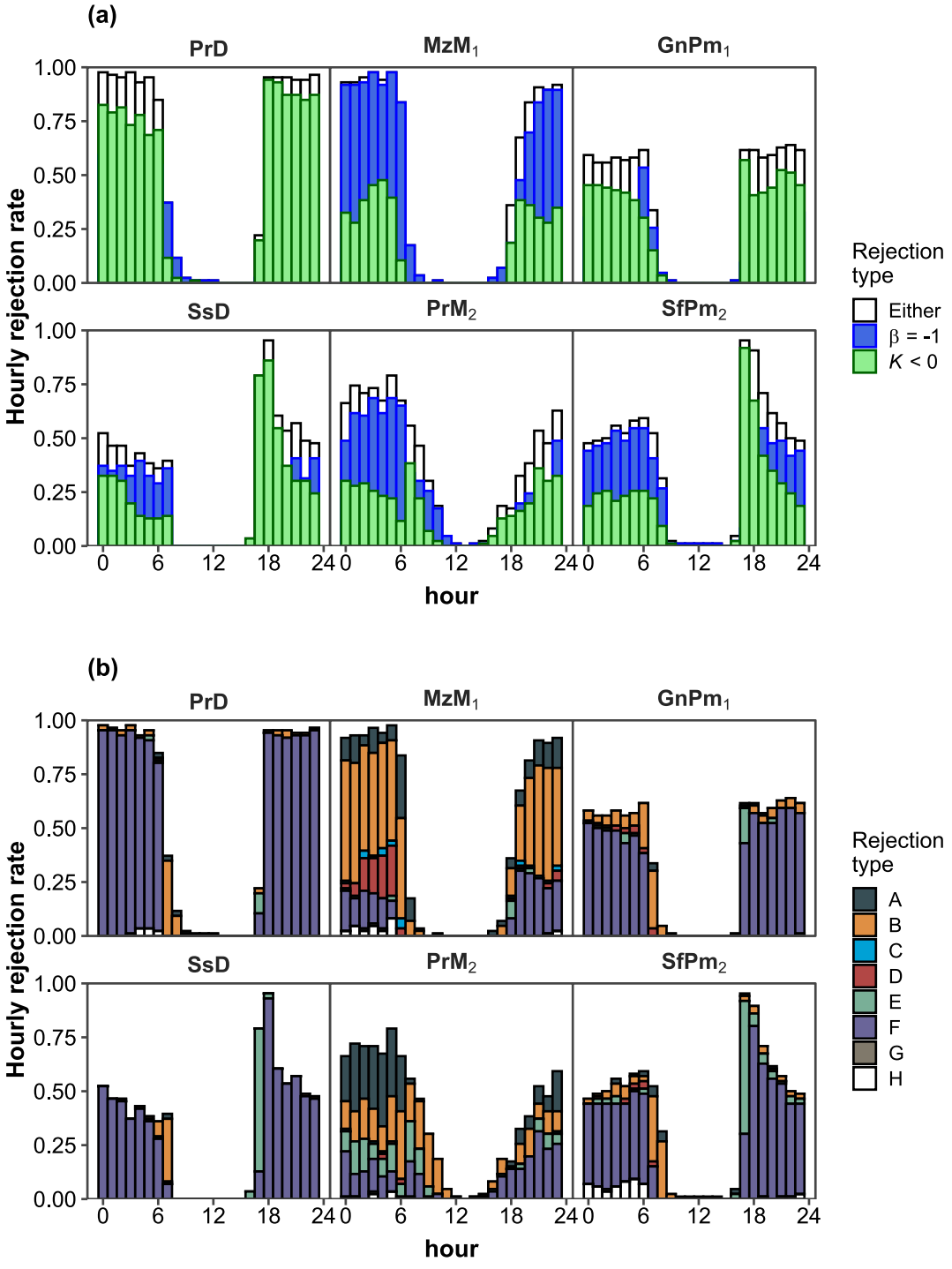

Figure 3-3 (a) Hourly rate of each rejection overlaid with Bowen ratio approaching −1 ($\beta = -1$), with incorrect flux sign ($K < 0$), and with either $\beta = -1$ or $K < 0$. (b) Hourly rate of the total rejection classified by meteorological conditions (A to H) defined in Table 3-2. The sample size of each observation for (a) and (b) was 2016 hourly data points for 84 days. The abbreviations for the observation conditions are defined in Table 3-3.

3.5. Conclusions

Using the hourly meteorological data from six agricultural field sites in three different climate conditions (PrD, SsD, MzM_1, PrM_2, $GnPm_1$, and $SfPm_2$) in Myanmar, we performed rejection determinations for the BREB calculation flux based on the criteria for data with the Bowen ratio approaching −1 and the incorrect sign of fluxes.

Rejection rates produced significantly inaccurate flux magnitudes due to Bowen ratios that approached −1 for all observation conditions at 29%, a 26% rate of obtaining incorrect flux signs, and a 43% rate for the overall rejected data. The highest rejection rate was 56% for PrD and then followed by 49% for MzM_1. The majority of the rejected data occurred during the nighttime, with rejection frequencies of 98% and 88% for PrD and MzM_1, respectively, as well as the rejection of most calculated negative latent fluxes. This study showed not only limitations associated with measurement accuracy due to $\Delta T \cong \Delta e/\gamma \cong 0$ but also meteorological conditions that spontaneously satisfy $\Delta T \cong -\Delta e/\gamma$ because the Bowen ratio approaches to −1. We found that the main factor for rejection was predominantly caused by the condition that satisfies $\Delta T \cong -\Delta e/\gamma$ during the dry season, during which large differences in the air temperature/water vapor pressure occur. Also, we found that rejection was due to the condition that satisfies $\Delta T \simeq \Delta e/\gamma \simeq 0$ in the monsoon season where small differences in air temperature/water vapor pressure occur. The majority of the rejected data yielded incorrect flux signs that satisfied $\gamma\Delta\theta > 0$ with exposure to negative available energy flux. The meteorological condition that increases Δe positively and decreases ΔT negatively contributed to the satisfaction of $\gamma\Delta\theta > 0$, such as a situation in flooded or high moisture surface exposed with dry night air. Rejected data are susceptible to measurement errors associated with a specific instrument during the period when the available energy flux and differences in air temperature/water vapor pressure are often nearly zero.

Taken togher, the BREB method cannot be applied under the conditions that the water vapor pressure gradient is positive (latent heat flux is upward) and the air temperature gradient is negative (sensible heat flux is downward), such as in a paddy field during nighttime in the dry season. Under the above observation conditions, the aerodynamic method by adding another wind speed in the BREB observation system (i.e., to observe the specific humidity and wind speed at two heights) can be suggested to estimate proper fluxes at the above conditions instead of the BREB method.

Chapter 4. Evapotranspiration Model Estimation

Simple and Two-Level Hierarchical Bayesian Approaches for Parameter Estimation with One- and Two-Layer Evapotranspiration Models of Crop Fields

4.1. Introduction

Evapotranspiration (*ET*) is the process of moving water from vegetation to the atmosphere by a combination of soil water evaporation (*E*) and crop transpiration (*T*). The measurement and prediction of *ET* are essential for many applications in agriculture, such as irrigation scheduling, crop yield forecasting, and general hydrologic studies [83]. *ET* and its components can be directly measured using lysimeter, sap flow, eddy covariance, and stable isotope techniques [84, 85]. However, these methods are expensive and labor intensive. Several models of *ET* have been developed since the 1950s. Over the last decade, the two-layer Shuttleworth–Wallace (SW) evapotranspiration model, which is physically sound and rigorous, has been widely used, and has shown performance superior to that of one-layer models such as the Penman–Monteith model (PM) [86] for different types of sparse crops, and different climatic conditions [29–32, 87, 88]. The SW model calculates *ET* as the sum of the PM equation for *E* and *T*, weighted by a set of coefficients that represent the combination of soil and canopy resistance [89]. However, the practical application of this approach is somewhat limited, since it is a highly complex model with a large number of specific parameters [31], which are both difficult and expensive to continuously measure under field conditions [33]. The most widely used approach to the estimation of parameter for the model is fitting to observed values by trial and error, using an approach such as a least-square method. However, this approach does not take into account the uncertainty in the model estimation process [34, 90]. When the least-square criterion is used, outliers can strongly influence the final values of the parameters, and can therefore introduce significant bias into the estimated model parameters [91].

Bayesian approaches have recently been used to simultaneously estimate the model parameters against the *ET* observed in the field [35]. These approaches have been used in grassland [36], for maize [37], for jujube [38], and for maize, vegetables, and fruit trees [39]. The Bayesian approach combines the probability distributions of model parameters based on the prior probabilities for magnitude and uncertainty, using observed data to generate the posterior distributions of the parameters. This approach allows the quantification of model inputs, parameters, and output uncertain-ties, and also takes into account prior knowledge for all parameters, and makes allowance for unknown influences [40].

However, these studies used a non-hierarchical Bayesian (HB) approach for parameter estimation. This approach cannot take into account sources of uncertainty such as variations in observed conditions or measurement errors in the model parameter estimation process. Using the non-hierarchical approach, the results are based on a specific set of parameter estimates, which are obtained in a specific observation group, under specific conditions, at a specific time. These results therefore cannot necessarily be generalized across different conditions and groups [41]. It is critical to consider the effects on the parameters of changes in season and observed conditions when simulating *ET* over long periods [38]. To improve parameter estimation, therefore, a Bayesian model with a hierarchical structure should be used, to take into account the variations in crop growth and seasonal fluctuations within a dataset. In a hierarchical model, individual parameter estimates are assumed to come from a group level distribution, such crop growth stages and observation periods, and can account for both differences and similarities between groups [92].

The objectives of this study, therefore, were: (1) to estimate the parameters of the SW and the PM models using simple non-hierarchical Bayesian (SB) and two-level HB approaches against *ET* data collected in the field for different crops and seasons, in Myanmar; (2) to compare the posterior distributions of the model parameters obtained using the SB and HB approaches; (3) to analyze the effects of variation in observation conditions on the posterior mean values of parameters calibrated using the HB approach in the SW and PM models; and (4) to assess the performance of models parameterized using either the SB or the HB approach on the estimation of daily *ET*. We calculated *ET* using the Bowen Ratio Energy Balance (BREB) method [23] at five agricultural fields over three seasons from 2017 to 2019 in Myanmar, where few studies on *ET* have been conducted. Thus, little data exists concerning crop water requirements and the water balance of agricultural fields. One of the most important problems with respect to agriculture in Myanmar is the shortage of irrigation, which leads to low productivity [93]. We expect that this study will not only improve the method of model parameter calibration, but also contribute to the practical application of *ET* models, increasing the efficiency of water use.

4.2. Materials and Methods

4.2.1. Study Sites and Observation

The study sites were experimental fields of the Department of Agricultural Re-search in the Zayarthiri Township of Naypyidaw (latitude 19°49.5′ N, longitude 96°16.44′ E, 100 m above sea level) (Figure 4-1a). This area has a moderate monsoon cli-mate, with an average annual rainfall of 1,100 mm, of which about 75% falls during the monsoon season, between June and September. The observation of *ET* using the BREB method was conducted using a tripod micrometeorological station installed at five agricultural experimental fields growing five crops—

rice, sunflower, sesame, and groundnut—over three seasons—dry, monsoon, and post-monsoon—from 2017 to 2019 (Figure 4-1b). The abbreviations of each observation, representing seasons and crops [i.e., sesame in the dry (SsD), paddy rice in the dry (PrD), paddy rice in the mon-soon (PrM), groundnut in the post-monsoon (GnPm), sunflower in the post-monsoon (SfPm) seasons], are defined in Table 4-1. The soil at a depth of 0–70 cm in the study fields was primarily sandy loam and clay loam with poor organic matter content, and partially contained a layer of loam and loamy sand. Due to the limited dataset in Myanmar, only PrD2 was used to validate the model parameters. The other observations were used for the calibration. The calibration period for the parameters of the *ET* model was 87 days for all observations. In the HB approach, the parameters were calibrated using a dataset of 87 days which was divided equally into three calibration periods of 29 days each considering three growth stages of crops (i.e., vegetative, reproductive, and ripening stages). The irrigated fields included both paddy rice and SsD fields, the soil condition of paddy field is almost saturated duration the observation, thus, the amount of water provided by basin irrigation was only observed for SsD.

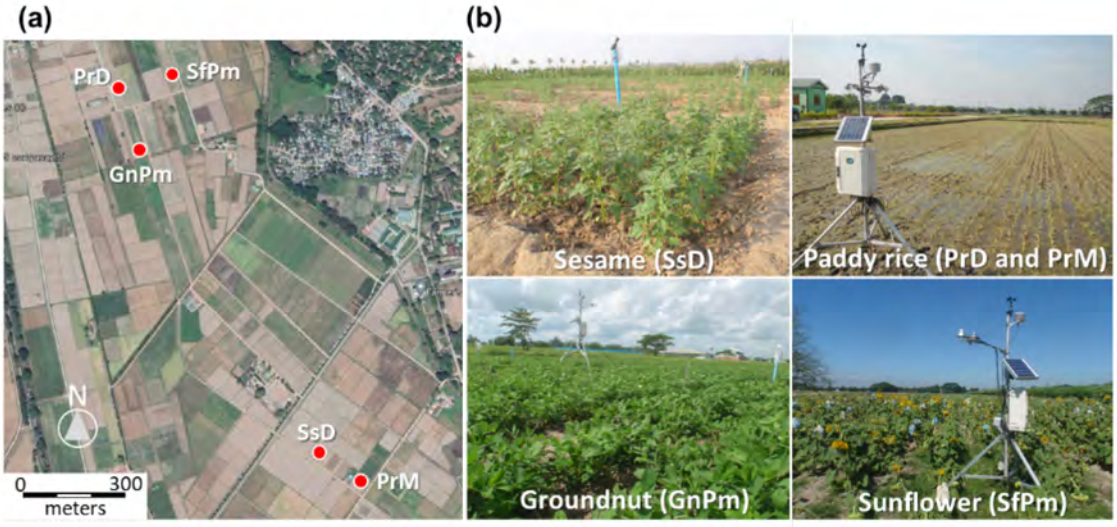

Figure 4-1. (a) experiment fileds location and (b) fields where evapotranspiration was observed.

Table 4-1 Conditions of observation of crops, seasons, cultivation schedules, and soil, and calibration/validation periods for model parameters using Bayesian approaches.

Abbrev.	Crops	Seasons	Sown Day/Harvested Day	Soil Texture	Periods (87 Days)
Calibration					data
SsD	Sesame	Dry	5 February/15 May	Clay loam	5 February–2 May 2018
PrD1	Paddy rice	Dry	27 January/11 June	Sandy loam	24 February–21 May 2019
PrM	Paddy rice	Monsoon	31 June/30 November	Sandy loam	1 August–26 October 2017
GnPm	Groundnut	Post-monsoon	12 September/12 January	Sandy loam	14 September–9 December 2018
SfPm	Sunflower	Post-monsoon	31 October/30 January	Sandy loam	8 November 2017–2 February 2018
Validation					
PrD2	Paddy rice	Dry	1 February/30 May	Sandy loam	4 February–1 May 2017

The BREB *ET* observation system was composed of thermo-hygrometers (air temperature and capacitive relative humidity sensor instruments) (HMP110; Vantaa, Vaisala, Finland) with multi-plate radiation shields (FP1806; Field Pro, Tokyo, Japan) located at 1.0 m and 2.5 m above ground level; solar radiometers (PCM−01NB−L3CS; PREDE Co., Tokyo, Japan) for shortwave radiation and infrared radiometers (PRI−01B−L3CS, PREDE Co,. Tokyo, Japan) for long-wave radiation; a heat flux sensor (PHF02−L5CS; PREDE Co. Tokyo, Japan); and an anemometer (03101Y−L3CS; RM Young, Traverse City, MI, USA). These data were automatically logged every 10 min using a data logger (CR1000; Campbell Scientific Inc., Logan, UT, USA). The soil moisture content was observed using capacitance sensors (GS-1; METER Group Inc., Pullman, WA, USA) installed in each field, which recorded into a data logger at 30 min intervals (Em50; METER Group Inc., Pullman, WA, USA). The daily mean datasets were used for the *ET* calculation of the BREB and the simulation of the SW model. We did not measure the leaf area index (LAI), and no research into LAI has been conducted in Myanmar. The LAI plays important roles in determining the coefficients of soil surface and canopy resistances in *ET* models, for weighting *ET* partitioning into *E* and *T*. However, since in this study we did not aim to rigorously evaluate *ET* by the models, we estimated the values of LAI from plant height using formulas from the literature, as described below.

4.2.2. Evapotranspiration Model

4.2.2.1. Two-Layer Model Based on the SW Model

The SW model is composed of the sum of two terms, *E* and *T*, as follows:

$$\lambda ET = \lambda E + \lambda T = \mathrm{C_s} ET_\mathrm{s} + \mathrm{C_c} ET_\mathrm{c} \tag{4-1}$$

where the latent heat flux (λET) is the sum of the latent heat of water evaporation of the soil surface (λE) and crops (λT), respectively (W m^{-2}). $\mathrm{C_s}$ and $\mathrm{C_c}$ represent the soil surface and canopy resistance coefficients, respectively. λ is the latent heat of water vaporization (MJ kg^{-1}). ET_s and ET_c represent the soil evaporation and the canopy transpiration (W m^{-2}), respectively, and are calculated as:

$$ET_\mathrm{s} = \frac{\Delta A + \left[\rho C_p D - \Delta r_\mathrm{a}^\mathrm{s}(A - A_\mathrm{s})\right]/(r_\mathrm{a}^\mathrm{a} + r_\mathrm{a}^\mathrm{s})}{\Delta + \gamma[1 + r_\mathrm{s}^\mathrm{s}/(r_\mathrm{a}^\mathrm{a} + r_\mathrm{a}^\mathrm{s})]} \tag{4-2}$$

$$ET_\mathrm{c} = \frac{\Delta A + \left[\rho C_p D - \Delta r_\mathrm{a}^\mathrm{c} A_\mathrm{s}\right]/(r_\mathrm{a}^\mathrm{a} + r_\mathrm{a}^c)}{\Delta + \gamma[1 + r_\mathrm{s}^\mathrm{c}/(r_\mathrm{a}^\mathrm{a} + r_\mathrm{a}^\mathrm{s})]} \tag{4-3}$$

where Δ is slope of the saturation vapor pressure curve at the mean air temperature (kPa °C^{-1}), ρ is the mean air density (kg m^{-3}), C_p is the specific heat capacity of dry air at constant pressure (approximately 1.01 kJ kg^{-1} °C^{-1}), γ is the psychrometric constant (approximately 0.066 kPa °C^{-1}), D is the air water vapor pressure deficit at the reference height (kPa), r_a and r_s are the aerodynamic resistance and stomatal resistance (s m^{-1}), respectively, and A and A_s represent the available energy input above the canopy and above the soil surface (W m^{-2}), respectively. These are expressed as:

$$A = R_\mathrm{n} - G \tag{4-4}$$

$$A_\mathrm{s} = R_\mathrm{ns} - G \tag{4-5}$$

where R_n and R_ns are the net radiation fluxes (W m^{-2}) into the canopy and the soil surface, and G is the soil heat flux (W m^{-2}). R_ns can be calculated using Beer's law:

$$R_\mathrm{ns} = R_\mathrm{n}\exp(-K_a \mathrm{LAI}) \tag{4-6}$$

where K_a is the extinction coefficient of light attenuation depending on crop development stage. For example, the K_a of rice increases from 0.35 to 0.62 from the vegetative period to the post-heading stage [94]. In this study, K_a was set to 0.4 for all crop and growth stages. The LAI is defined as the effective value of the leaf area index that accounts for illumination-induced stomatal closure deeper in the canopy (m^2 m^{-2}). The value of estimated LAI ($\mathrm{LAI_{est}}$) was estimated

from the measured plant height (h_c) using the following formula for typical values of field crops [95, 96]:

$$\mathrm{LAI_{est}} = \mathrm{LAI_{max}} + 1.5 \ln (h_c) \tag{4-7}$$

The maximum LAI ($\mathrm{LAI_{max}}$) for normal conditions of plant density were obtained from the literature, and were 4.0 for rice [97, 98], 5.0 for groundnut [99, 100], 3.0 for sunflower [101], and 2.2 for sesame [102]. The coefficients C_s and C_c are given by the expressions:

$$\mathrm{C_s} = \frac{1}{1 + [R_s R_a / R_c (R_s + R_a)]} \tag{4-8}$$

$$\mathrm{C_c} = \frac{1}{1 + [R_c R_a / R_s (R_c + R_a)]} \tag{4-9}$$

in which R_a, R_s, and R_c are calculated as:

$$R_a = (\Delta + \gamma) r_a^a \tag{4-10}$$

$$R_s = (\Delta + \gamma) r_a^s + \gamma r_s^s \tag{4-11}$$

$$R_c = (\Delta + \gamma) r_a^c + \gamma r_s^c \tag{4-12}$$

The three aerodynamic resistance values (r_a^c, r_a^a and r_a^s) (s m^{-1}) were calculated using the methodology of [103], as detailed in Appendix A. The bulk stomatal resistance of the canopy (r_s^c) (s m^{-1}), which is the equivalent resistance of all the individual stoma in a canopy and depends on other environmental variables, can be calculated using the Jarvis-type model [104, 105] and following the protocol of [36] as;

$$r_s^c = \frac{r_{STmin}}{\mathrm{LAI}\{F_1(R_s) F_2(T_a) F_3(D) F_4(wc)\}} \tag{4-13}$$

where r_{STmin} indicates the minimal stomatal resistance (s m^{-1}), and is estimated using a Bayesian approach. Following previous studies [36, 106], the stress functions F_1 to F_4, representing the effect of the variables related to soil surface and aerodynamic resistance R_s, air temperature T_a (°C), D (kPa), and volumetric moisture content wc (m^3 m^{-3}), are defined as follows:

$$F_1(R_s) = \frac{R_s}{1000} \frac{1000 + k_1}{R_s + k_1} \tag{4-14}$$

$$F_2(T_a) = \frac{\left(T_{\mathrm{a}} - T_{\mathrm{a,low}}\right)\left(T_{\mathrm{a,high}} - T_{\mathrm{a}}\right)^{\left(T_{\mathrm{a,high}} - k_2\right)/\left(k_2 - T_{\mathrm{a,low}}\right)}}{\left(k_2 - T_{\mathrm{a,low}}\right)\left(T_{\mathrm{a,high}} - k_2\right)^{\left(T_{\mathrm{a,high}} - k_2\right)/\left(k_2 - T_{\mathrm{a,low}}\right)}} \tag{4-15}$$

$$F_3(D) = 1 - k_3 D \tag{4-16}$$

$$F_4(wc) = \begin{cases} 1 & wc_{root} > wc_{\mathrm{cr}} \\ \dfrac{\left(wc_{root} - wc_{\mathrm{wp}}\right)}{\left(wc_{\mathrm{cr}} - wc_{\mathrm{wp}}\right)} & wc_{\mathrm{wp}} \le wc_{root} \le wc_{\mathrm{cr}} \\ 0 & wc_{root} < wc_{\mathrm{wp}} \end{cases} \tag{4-17}$$

where k_1 (W m^{-2}), k_2 (°C), and k_3 (kPa^{-1}) are constants optimized using a Bayesian approach. $T_{\mathrm{a,low}}$ and $T_{\mathrm{a,high}}$ are the low and high temperature limits, and were assumed to be 0 and 40 °C, respectively [107]; wc_{root} is the moisture content in the root zone, estimated from observed data at a depth of 0–50 cm (m^3 m^{-3}); wc_{wp} is the moisture content at the wilting point (m^3 m^{-3}) measured in the laboratory, and wc_{cr} is the critical moisture content at which plant stress starts, set to 60% of saturated moisture content [35]. When the value of the stress function is zero, the canopy resistance is not calculated. The soil surface resistance ($r_{\mathrm{s}}^{\mathrm{s}}$) (s m^{-1}) is expressed as:

$$r_{\mathrm{s}}^{s} = \exp\left(b_1 - b_2 \frac{wc_{sur}}{wc_{\mathrm{SAT}}}\right) \tag{4-18}$$

where b_1 and b_2 are empirical constants (s m^{-1}) representing the estimation parameters using the Bayesian approaches; wc_{sur} is the observed volumetric soil moisture content 5 cm below the soil surface, and wc_{SAT} is the saturated moisture content.

4.2.2.2. Traditional One-Layer PM Model

The PM model can be formulated as [5]:

$$\lambda ET = \frac{\Delta(R_n - G) + \rho C_p D / r_a}{\Delta + \gamma(1 + r_s^c / r_a)} \tag{4-19}$$

where the canopy resistance r_s^c was computed following Equation (4-15). r_{a} is the aerodynamic resistance (s m^{-1}) and is usually calculated using the following equation, assuming neutral stability conditions [42]:

$$r_a = \frac{1}{k^2 u_2} \ln\left(\frac{z - d}{h_c - d}\right) \ln\left(\frac{z - d}{z_0}\right) \tag{4-20}$$

where k is von Karman's constant (0.41), u is the wind speed at 2 m height (m s^{-1}); z is the reference height above the crop at which meteorological measurements are available (2 m); d is zero plane displacement (m), estimated as $d = 0.63 \cdot h_{\mathrm{c}}$; and z_0 is the roughness length for momentum transfer (m), estimated as $z_0 = 0.13 \cdot h_{\mathrm{c}}$.

4.3. Simple and HB Approaches

Figure 4-1 shows the graphical models of the (a) SB and (b) HB approaches, and (c) the structure of the two-layer model based on the SW model constructed using the HB approach in this study. In Figures 4-1ab, *O* indicates the observed *ET* data, θ_s represents the model specific unknown parameters associated with canopy resistance (r_{STmin}, k_1, k_2, k_3, b_1, and b_2), and σ_{θ_s} indicates the variance in three observation periods in a dataset called "hyperparameters". These parameters describe the probability distribution. A set of parameters, θ_s, generates a set of data, *O*, through a likelihood function, *f*. In the HB approach, the model parameters θ_s are generated by other processes, g_l parameterized by σ_{θ_s}, and its structure accommodates the group level differences: the observation period and crop growth stage. The structure of the SW model using the HB approach is composed of the specific parameters, hyperparameters, observed data, and functions with variables shown in Figure 4-1c.

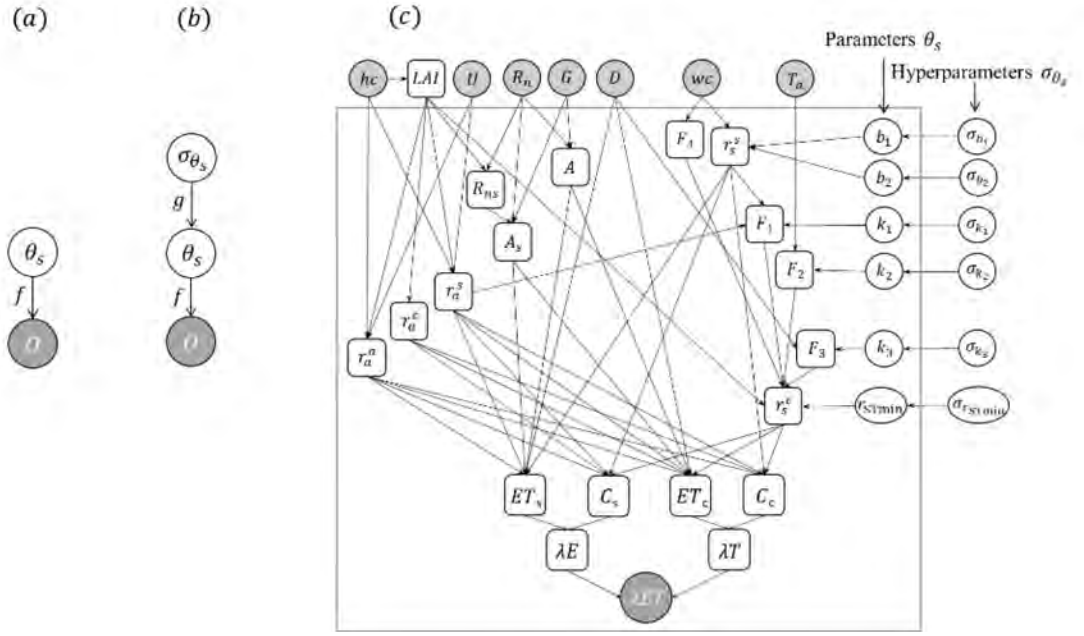

Figure 4-2 Graphical models of the (a) simple (SB) and (b) hierarchical Bayesian (HB) approaches, and (c) structure of the Shuttleworth–Wallace (SW) model using the HB approach. The box contains the SW model elements based on Equations (4-1) to (4-20). The gray-shaded circle nodes with white letters and with black letters indicate observed latent heat flux (λET) and other elements inputted (h_c: plant height, *U*: wind speed, R_n: net radiation, *G*: soil heat flux, *D*: vapor pressure deficit, *wc*: soil moisture content, T_a: air temperature), respectively. The square nodes with black letters represent variables that are determined by a specific function applied to another variable.

The probabilistic models for the estimation of parameters of the *ET* model are described as follows. For the SB approach,

$$O_{ET}[t] \sim \text{Normal}(S_{ET}(\theta_s)[t], \sigma) \quad (4\text{-}21)$$

and for the HB approach,

$$O_{ET\,[c]}[t] \sim \text{Normal}\left(S_{ET}(\theta_{s\,[c]})[t], \sigma\right) \quad (4\text{-}22)$$

$$\theta_{s\,[c]} \sim \text{Normal}\left(\theta_{s,mean}, \sigma_{\theta_s}\right) \quad (4\text{-}23)$$

where the SB approach does not include the constant *c*, representing different groups; in this study, the three calibration periods. $O_{ET\,[c]}[t]$ indicates the *ET* data observed at day *t* (1, 2, …, 87 in this study) at each observation period, divided evenly into three calibration periods *c* (1, 2, 3), $S_{ET\,[c]}[t]$ are the *ET* data estimated by the SW and PM models at day *t* for each period *c*, and σ is the standard deviation, representing the measurement error variance of *ET* estimates (mm day^{-1}). Normal indicates a normal distribution from which the *ET* estimates are generated. $\theta_{s\,[c]}$ represents a prior uncertainty in the parameters of the calibration period, and can be described as being stochastically generated from a normal distribution of $\theta_{s,mean}$ and σ_{θ_s}. $\theta_{s,mean}$ is the overall mean distribution of each parameter in a dataset, while σ_{θ_s} is a random variable distribution that represents the difference in the calibration period of the parameter. We assumed that the specific unknown parameters θ_s are distributed uniformly within a specified prior distribution range, as shown in Table 4-2.

In this study, all the simulations and calculations were performed in R version 4.0.2. For estimating the posterior distribution for the SB and HB approaches, we used RStan version 2.19.3 developed by [109], which employs a Markov Chain Monte Carlo (MCMC) technique to sample from the posterior distribution of a given model. We ran four MCMC chains with 50,000 iterations, and monitored them to confirm that the MCMC chains converged to the target distributions. When the Rhat of RStan was less than 1.05, we judged the chains to have converged.

Table 4-2 Prior distributions used for estimating the posterior distributions of the model parameters associated with canopy and soil surface resistance.

Parameter	Prior Range	References
$r_{ST\,\min}$	[0, 60]	[104]
k_1	[0, 500]	[105]
k_2	[5, 30]	[104]
k_3	[0, 0.1]	[105]
b_1	[4, 15]	[108]
b_2	[0, 8]	[108]

4.3.1. Evaluation of the Performance of the SW Model Using Bayesian Approaches

The *ET* values calculated from the posterior mean values of the model parameters in the SW and the PM models were evaluated using four statistical criteria: the mean absolute error (MAE), the root mean square error (RMSE), the mean absolute percentage error (MAPE), and the root mean square percentage error (RMSPE). The MAE can potentially be used to identify bias. RMSE provides an overall measure of the degree to which the data differ from the model estimation. MAE and RMSE values of zero indicate a perfect fit. MAPE and RMSPE, which can express the estimation accuracy as a ratio, were included because the model was estimated under different observation conditions: the dry and the monsoon. These statistical criteria are described as follows:

$$\mathrm{MAE} = \frac{1}{n}\sum_{i=1}^{N}|E_i - O_i| \tag{4-26}$$

$$\mathrm{RMSE} = \sqrt{\frac{1}{n}\sum_{i=1}^{N}(E_i - O_i)^2} \tag{4-27}$$

$$\mathrm{MAPE} = \frac{1}{n}\sum_{i=1}^{N}\left|\frac{E_i - O_i}{O_i}\right| \tag{4-28}$$

$$\mathrm{RMSPE} = \sqrt{\frac{1}{n}\sum_{i=1}^{N}\left(\frac{E_i - O_i}{O_i}\right)^2} \tag{4-29}$$

where E_i and O_i represent the estimated and observed values, respectively. N (or n) is the number of data points in the dataset.

4.4. Results and Discussion

4.4.1. Differences in Observation Conditions in a Dataset

In the HB approach, the model parameters were estimated taking into account the uncertainty in group levels within a dataset. The growth period of crops is generally separated into three stages: the vegetative, reproductive, and ripening stages. Therefore, daily observed data for the 87 days were divided into three periods to calibrate the parameters using the HB approach, as described in Figure 4-2.

The difference between R_n and T_a in the first and third periods of the dry season and the post-monsoon was greater than that for the monsoon season. The T_a of PrM was almost constant, and SsD, PrD1 and PrD2 gradually increased, but GnPm and SfPm gradually decreased over the three periods. The difference between the minimum and maximum T_a in a dataset was 3.6 °C in the monsoon, 6.1 °C and 8.1 °C in the dry, and 7.2 °C and 8.0 °C in the post-monsoon seasons,

respectively. Changes in *wc*, except in the paddy field, indicated that SsD, GnPm and SfPm had decreased residual *wc*, and PrM, PrD1 and PrD2 with ponded water maintained high. As calculated using Equation (4-7), the estimated LAI values increased rapidly in the first and second periods, and gradually reached a constant value in the third calibration period. The value of PrD1 and PrD2 increased constantly over the entire period.

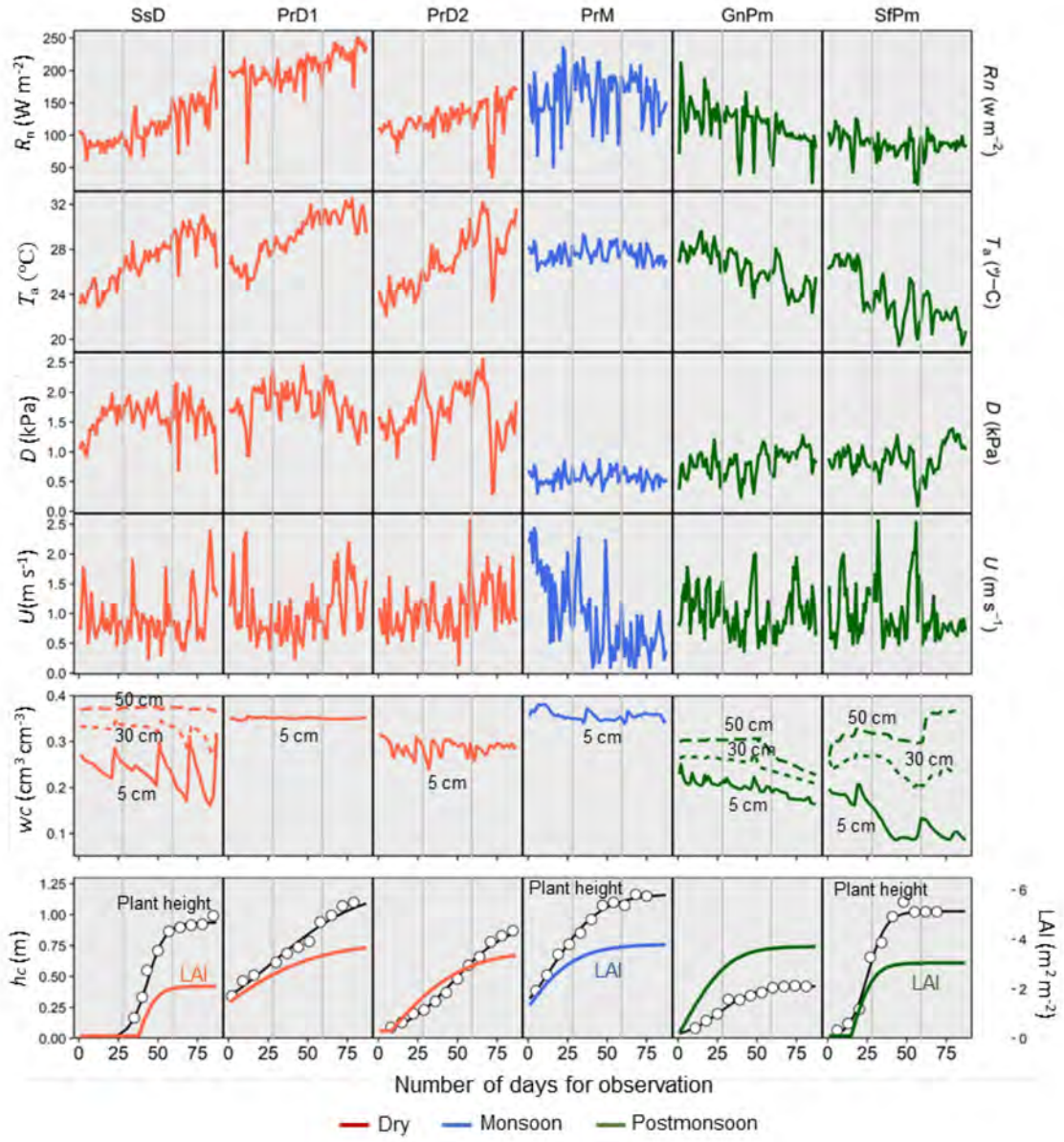

Figure 4-3 Variations in daily net radiation (R_n), air temperature (T_a), air water vapor pressure deficit (D), wind speed (U), soil moisture content (wc), and plant height (h_c) with estimated leaf area index (LAI) in different observation periods at three fields in the dry season, a different field in the monsoon season, and a third set of two fields in the post-monsoon season. The three calibration periods for HB are indicated by vertical lines.

4.4.2. Model Parameter Estimation Using the SB and HB Approaches

4.4.2.1. Comparison of Posterior Distributions of Model Parameters

A violin plot, depicting the posterior distribution of the SW and PM models parameters using the SB and HB approaches, is presented in Figure 4-3. These results showed that parameterizations using SB and HB were, in most cases, successful in reducing the uncertainties in the parameters. Several posterior distributions, such as the k_2 of SsD and the b_1 of SfPm for the SW model were strongly constrained, indicating their importance as a parameter for controlling *ET* estimation and partition (Figure 4-3a), as discussed below. In the estimation of the k_2 of SsD, we assumed that the strong correlation between T_a and the observed *ET* with the small LAI was a factor that constrained the posterior distributions, in order to reduce the value of *T*. SsD had the highest correlation with T_a, which was associated with k_2, and the observed *ET* of all crops. The correlation coefficients between daily T_a and the observed *ET* in descending order were SsD 0.66 > PrD1 0.57 > PrM 0.47 > GnPm 0.36 > SfPm 0.21. This strongly constrained k_2 of SsD at the low side of the prior bound, indicated that the stomatal resistance of the canopy largely limited the value of *T*. In the estimation of the b_1 of SfPm in the SW model, the soil moisture of SfPm near the soil surface was the lowest of all observations (Figure 4-2). The posterior distribution range of b_1 associated with the soil surface resistance was therefore constrained to the low side of the prior range, to reduce the value of *E*. The parameter k_3, which is related to *D*, was poorly constrained, and displayed large variability in all observations (Figure 4-3). Although the *D* value differed considerably between the dry and monsoon seasons (Figure 4-2), there were no differences in the posterior distribution of k_3 between the two seasons for the SW model. As previous studies [36, 37] showed, k_3 is an insensitive parameter of the models. Some parameters showed large differences between SB and the HB on the posterior distribution. For example, the b_2 of SsD for the SB in the SW model was constrained at the low side on the prior bound, but that for the HB was restricted at the upper side, with no differences in group levels (Figure 4-3a). This observation indicated that the parameter b_2 calibrated by the SB and the HB had different abilities under the same environmental factors, and thus might have made a difference in the estimated and partitioned *ET* between the SB and HB approaches (Figure 4-3a).

The range of posterior distributions for several parameters differed substantially between the SW and PM models. For example, the r_{STmin} of PrM of the SW model was well constrained compared to that of the PM model. For the PM model, the k_2 of SsD had lower uncertainty than that for the SW model, and for PrD1 was constrained at the upper side, in contrast to the SW model. The differences in model structure between the SW and PM models affected the reduction of uncertainties in the parameter estimation. However, for most of parameters and conditions, there were no large differences in the range of posterior distributions between the models.

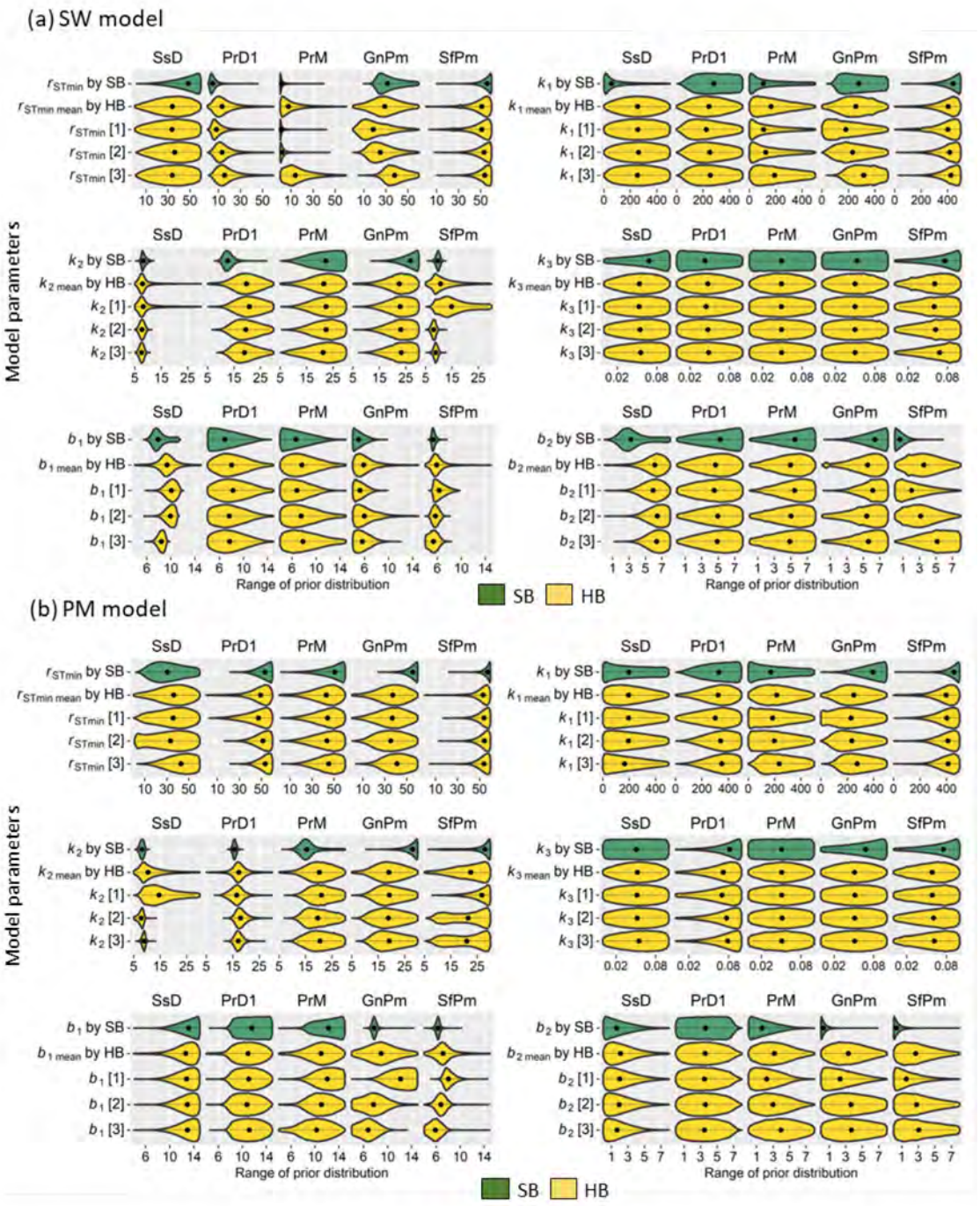

Figure 4-4 Violin plots of the posterior distributions of (a) the Shuttleworth–Wallace (SW) and (b) Penman–Monteith (PM) model parameters calibrated using simple Bayesian (SB) and hierarchical Bayesian (HB) approaches. The numbers in square brackets with parameters indicate the three calibration periods of the HB approach. Parameters with mean by HB represent the overall mean distribution. The black dotted circles and horizontal lines inside the violin shapes represent the posterior means and 95% credible intervals.

Table 4-3 Posterior probability distributions of the parameters in the Shuttleworth–Wallace (SW) and the Penman–Monteith (PM) models using simple Bayesian (SB) and hierarchical Bayesian (HB) approaches for five observations, characterized by the posterior means and 95% Bayesian credible intervals.

Parameter	Model	Bayes	SsD	PrD1	PrM	GnPm	SfPm
r_{STmin} (s m^{-1})	SW	SB	45.8 (19.0, 59.5)	5.60 (1.60, 15.2)	2.10 (0.033, 10.4)	33.9 (19.6, 57.0)	54.4 (40.9, 59.8)
		HB	33.4 (5.40, 57.4)	15.8 (2.30, 45.2)	11.6 (0.41, 45.8)	29.4 (4.48, 55.8)	48.2 (19.1, 59.3)
	PM	SB	31.8 (9.46, 57.6)	52.0 (37.6, 59.7)	47.7 (22.3, 59.6)	54.3 (41.5, 59.8)	56.5 (47.7, 59.9)
		HB	35.2 (5.95, 57.6)	46.6 (16.4, 59.0)	40.9 (11.8, 58.4)	36.3 (8.55, 57.3)	51.2 (27.8, 59.4)
k_1 (W m^{-2})	SW	SB	104 (2.10, 432)	284 (70.3, 489)	155 (2.30, 471)	286 (104, 488)	427 (266, 498)
		HB	256 (32.2, 473)	250 (37.4, 470)	185 (11.3, 453)	257 (36.3, 471)	381 (125, 492)
	PM	SB	214 (4.50, 483)	317 (86.1, 492)	197 (3.20, 479)	378 (177, 495)	446 (322, 498)
		HB	209 (14.4, 463)	309 (64.1, 483)	225 (22.9, 464)	254 (39.2, 470)	378 (137, 490)
k_2 (°C)	SW	SB	8.41 (7.02, 10.6)	12.9 (10.0, 17.2)	21.6 (10.4, 29.6)	26.2 (18.8, 29.9)	9.70 (8.11, 11.0)
		HB	9.06 (5.55, 21.0)	19.7 (9.23, 28.6)	20.9 (8.76, 29.2)	22.0 (9.96, 29.3)	12.2 (5.82, 26.0)
	PM	SB	8.11 (6.66, 9.50)	15.7 (14.5, 17.0)	16.3 (10.95, 27.6)	27.2 (19.8, 29.9)	25.8 (11.6, 29.9)
		HB	12.0 (5.77, 26.0)	17.4 (10.2, 25.3)	20.1 (9.23, 28.9)	19.1 (8.34, 28.7)	21.5 (7.94, 29.5)
k_3 (kPa^{-1})	SW	SB	0.063 (0.006, 0.099)	0.045 (0.002, 0.096)	0.049 (0.002, 0.097)	0.052 (0.003, 0.098)	0.069 (0.009, 0.099)
		HB	0.053 (0.006, 0.095)	0.048 (0.005, 0.094)	0.049 (0.005, 0.094)	0.050 (0.005, 0.095)	0.058 (0.008, 0.096)
	PM	SB	0.050 (0.003, 0.097)	0.077 (0.024, 0.099)	0.050 (0.002, 0.098)	0.063 (0.006, 0.099)	0.069 (0.009, 0.099)
		HB	0.052 (0.006, 0.095)	0.068 (0.015, 0.098)	0.051 (0.006, 0.095)	0.051 (0.005, 0.095)	0.056 (0.007, 0.096)
b_1 (s m^{-1})	SW	SB	8.20 (6.39, 11.1)	7.26 (4.13, 12.0)	7.06 (4.12, 12.0)	5.21 (4.04, 7.36)	5.41 (4.92, 6.16)
		HB	9.42 (5.74, 13.2)	8.32 (4.45, 13.6)	8.00 (4.36, 13.6)	6.33 (4.16, 11.8)	6.22 (4.35, 10.6)
	PM	SB	12.9 (9.27, 14.9)	11.6 (8.13, 14.8)	12.0 (8.22, 14.9)	7.81 (7.07, 8.67)	6.29 (5.54, 7.05)
		HB	12.3 (7.03, 14.8)	10.9 (6.57, 14.5)	10.8 (5.61, 14.5)	9.06 (4.58, 14.2)	7.39 (4.49, 12.3)
b_2 (s m^{-1})	SW	SB	3.65 (1.16, 7.66)	4.93 (0.626, 7.88)	5.18 (0.835, 7.89)	6.13 (2.86, 7.93)	0.774 (0.027, 2.33)
		HB	5.87 (2.23, 7.79)	4.54 (0.685, 7.67)	4.76 (0.789, 7.69)	5.19 (0.616, 7.78)	3.65 (0.40, 7.40)
	PM	SB	2.02 (0.072, 5.87)	3.59 (0.192, 6.96)	1.99 (0.069, 5.57)	0.419 (0.010, 1.55)	0.573 (0.013, 2.28)
		HB	2.43 (0.183, 6.55)	3.62 (0.359, 7.19)	3.30 (0.329, 7.19)	3.474 (0.315, 7.38)	2.98 (0.230, 7.17)
σ (mm day^{-1})	SW	SB	0.406 (0.348, 0.477)	0.702 (0.603, 0.821)	0.840 (0.723, 0.981)	0.509 (0.438, 0.595)	0.318 (0.273, 0.373)
		HB	0.310 (0.265, 0.364)	0.705 (0.604, 0.825)	0.806 (0.692, 0.943)	0.479 (0.412, 0.561)	0.285 (0.244, 0.336)
	PM	SB	1.20 (1.03, 1.40)	0.676 (0.581, 0.792)	0.948 (0.815, 1.11)	0.897 (0.768, 1.05)	1.05 (0.892, 1.23)
		HB	1.06 (0.911, 1.24)	0.646 (0.553, 0.760)	0.768 (0.660, 0.899)	0.701 (0.602, 0.820)	0.944 (0.808, 1.11)

4.4.2.2. Effect of Difference in Observation Conditions on Parameter Estimation

The differences between the posterior distributions of the model parameters estimated using the HB approach based on observed *ET* data, over the three calibration periods, were clear in several cases (Figure 4-3), including the r_{STmin} of PrM and GnPm, the k_1 of GnPm, the k_2 of SfPm, and the b_1 of SsD in the SW model, and the k_2 of SsD and SfPm, the b_1 of GnPm, and the b_2 of SfPm in the PM model. However, in the k_3 of all conditions, and all parameters for PrD1 these differences were unclear.

The degrees of variation in the posterior mean value of the three calibration periods in a dataset—the coefficient of variation (CV) for each parameter and observation—are shown in Figure 4-4. The CV was calculated from the posterior mean value of σ_{θ_s} divided by $\theta_{s,mean}$ in Equation (4-25). The CV values of r_{STmin}, which is associated with stomatal resistance, varied greatly depending on the observations, and the difference between the SW and PM models was also larger than those of other parameters. Since the two-layer SW model is sensitive to error in the values of canopy and soil resistance [32, 111], measurement errors or improperly used constants and variables, such as K_a and LAI, may have increased the variation in the estimation of this parameter. In paddy fields, which have continuously saturated surfaces in which the fluctuations in the surface resistance are small, the variations in r_{STmin} may be strongly affected by the growth of plant. In contrast, the variability of k_3 was nearly constant, regardless of differences in the models and observations. The posterior distributions of k_3 were poorly constrained and widespread along prior ranges (Figure 4-3). As has been shown in previous studies [102, 103, 105], this observation suggests that k_3 is not very susceptible to seasonal fluctuations with large uncertainties. Therefore, k_3 may not be necessary for strict parameter estimation, and empirical values may suffice.

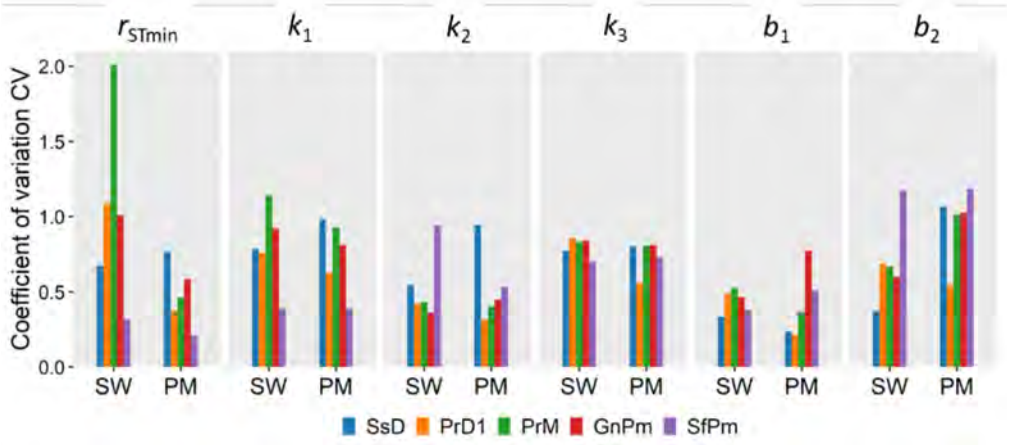

Figure. 4-5 Coefficient of variation of posterior mean values of the parameters estimated in the Shuttleworth–Wallace (SW) and Penman–Monteith (PM) models using the hierarchical Bayesian (HB) approach, calculated from σ_{θ_s} divided by $\theta_{s,mean}$ in Equation (4-25), indicating the degree of variation in the posterior mean value of the three calibration periods.

4.4.2.3. Comparison of *ET* Estimation by SW and PM Models Using SB and HB Approaches

Figures 4-5a and 4-6a show the daily changes in observed and estimated *ET* using the SW and the PM models with parameters calibrated using the SB and HB approaches with irrigation + rainfall amount for SsD, while rainfall amount only was used for the others. Figures 4-5b and 4-6b show the values corresponding to the difference in the SB and HB approaches on the estimated *ET*, calculated as the estimated *ET* of the SB approach divided by that of the HB approach. The *ET* observed and estimated by the two models with parameters calibrated by the SB and HB approaches with portioned *E* and *T* only for the SW model, and the results of statistical evaluation for the model performances are shown in Table 4-3, and the regression analysis between the observed *ET* and that estimated by the models are presented in Figure 4-7.

For the SW model, generally, the posterior mean value of the parameters calibrated using the SB and HB approaches provided acceptable estimations of *ET* over 87 days (Figure 4-5a), and the differences in the estimated total values of *ET* between the SB and HB approaches were small: 0 to 1 mm for PrD1 and SfPm, and 3 to 10 mm for SsD, PrM, and GnPm (Table 4-3). However, for the PM model, there was a large difference between the estimated and observed *ET*, except for PrD1 and PrM (Figure 4-6a and Table 4-3). The confidence intervals of the posterior distributions on the estimated *ET* for the PM model were generally wider than those for the SW model, indicating that large uncertainty in the parameter values led to poor model performance. For the PrD1 of both models, the estimated total value of *ET* produced by the SB and HB approaches were very similar (Table 4-3). The values of $ET_{sw.SB}/ET_{sw.HB}$ and $ET_{pm.SB}/ET_{pm.HB}$ were close to 1.0 over the entire period (Figures. 4-5b and 4-6b), indicating a lack of variation in the posterior mean distributions at three calibration periods using the HB approach (Figure 4-3). The *wc* and LAI values changed constantly or linearly over all calibration periods (Figure 4-2). Therefore, even when the variables that affected the estimation of the parameters varied considerably over the calibration period, the variables would not have affected the parameter estimation for each period if the change ratio was a constant. For PrM with a small fluctuation in environmental factors, a slight difference in *ET* estimates between SB and HB was apparent in the third calibration period (Figures. 4-5b and 4-6b), possibly because the estimated LAI value varied in different change rate at the third period (Figure 4-2). The averaged change rate of LAI for the three stages in PrM were 3.2%, 1.0%, and 0.1%. For SsD and SfPm, large fluctuations in environmental factors produced differences between the *ET* estimates obtained using the SB and HB approaches for almost the entire period, especially in the PM model (Figures 4-5 and 4-6). This observation suggests that the SW model could adapt well to changes in seasons and surface conditions with respect to parameter estimation, but the PM model was subject to environmental fluctuation in the calibration period.

The *ET* estimates obtained using the HB approach in both models were better than those produced using the SB approach in both models, indicating that the performance of the SW model was superior to that of the PM model (Table 4-3). The slope of the estimates obtained using the HB approach in the regression was closer to 1 than that produced by the SB for most observation conditions in both models (Figure 4-7). Considering the magnitude of errors for the BREB method, which are reported to be in order of several to 10 percent [112], it is not appropriate to evaluate the accuracy of estimated *ET* with parameters calibrated using the SB and HB approaches. However, the HB approach improved the fit of the model to the observed data, indicating the potential importance of accounting for seasonal fluctuations and variations in crop growth stages in calibrating models which can reliably predict *ET*.

For *ET* partitioning in PrM for the SB and HB approaches in the SW model (Table 4-4), the E_{est} and E_{est}/ET_{est} values were very small, at 43 mm and 0.08, respectively, indicating the improper use of estimated LAI values, or the uncertainty in *ET* partitioning by the SW model calibrated using only observed *ET* data. However, due to the lack of direct measurements of the different components of *ET*, it is not possible to validate the partitioned *ET* values using the SB and HB approaches in the SW model, although the estimated total *ET* was acceptable. Thus, multiple observations obtained using lysimeters and measures of sap flow should be used to validate *ET* partitioning into *E* and *T* by the SW model using the Bayesian approach in future studies.

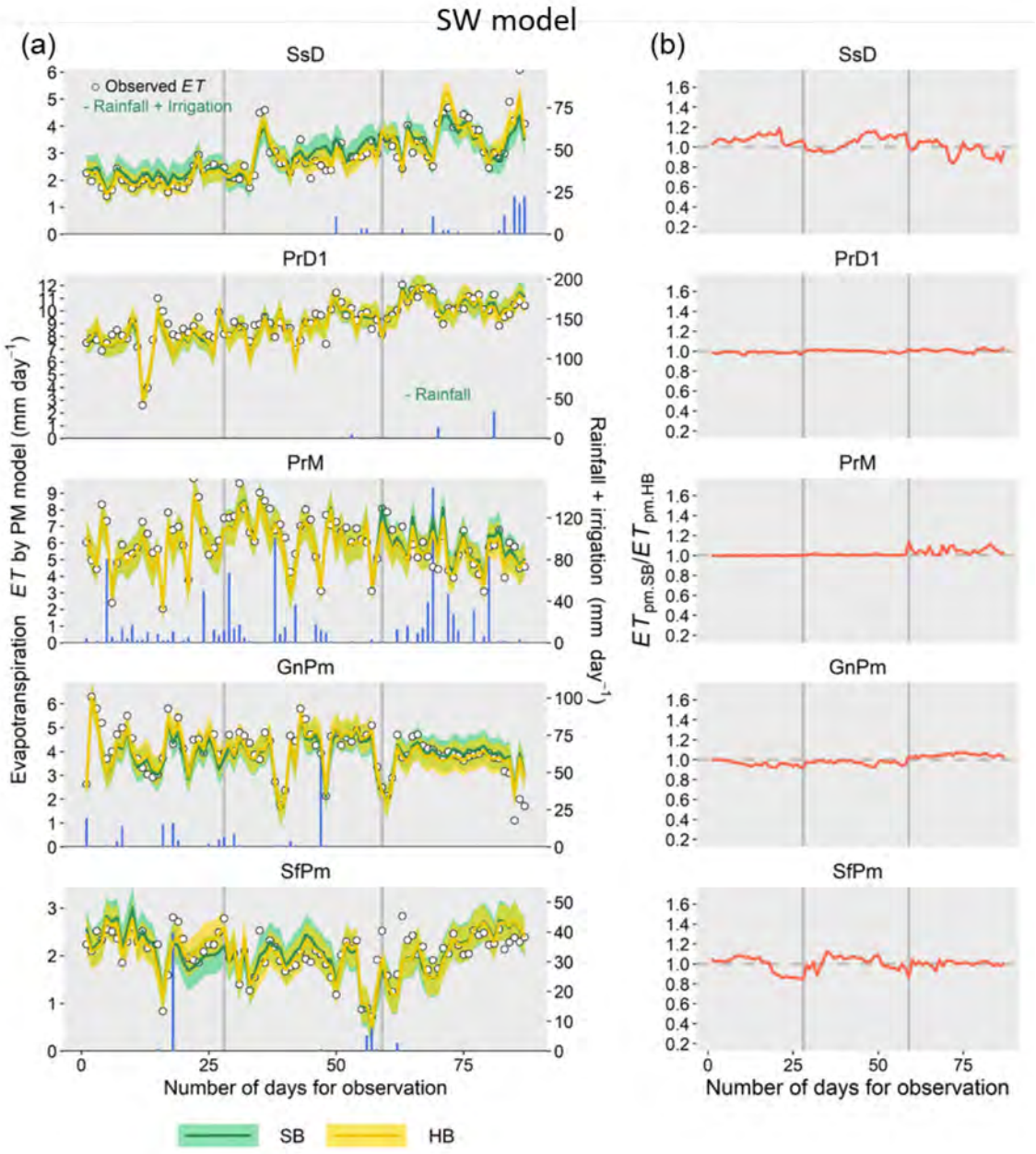

Figure 4-6 (**a**) Observed and estimated evapotranspiration (*ET*) using the Shuttleworth–Wallace (SW) model with parameters calibrated using simple Bayesian (SB) and hierarchical Bayesian (HB) approaches. Lines and bands corresponding to the posterior means and credible intervals at the 95% probability, respectively, in all five observation conditions. Vertical bars indicate the rainfall + irrigation amount for the SsD, and rainfall only for the others. (**b**) Variations in the values of $ET_{sw.SB}$ and $ET_{sw.HB}$ calculated from *ET* estimates by the SW model using SB and HB. The three calibration periods for HB are separated by vertical lines.

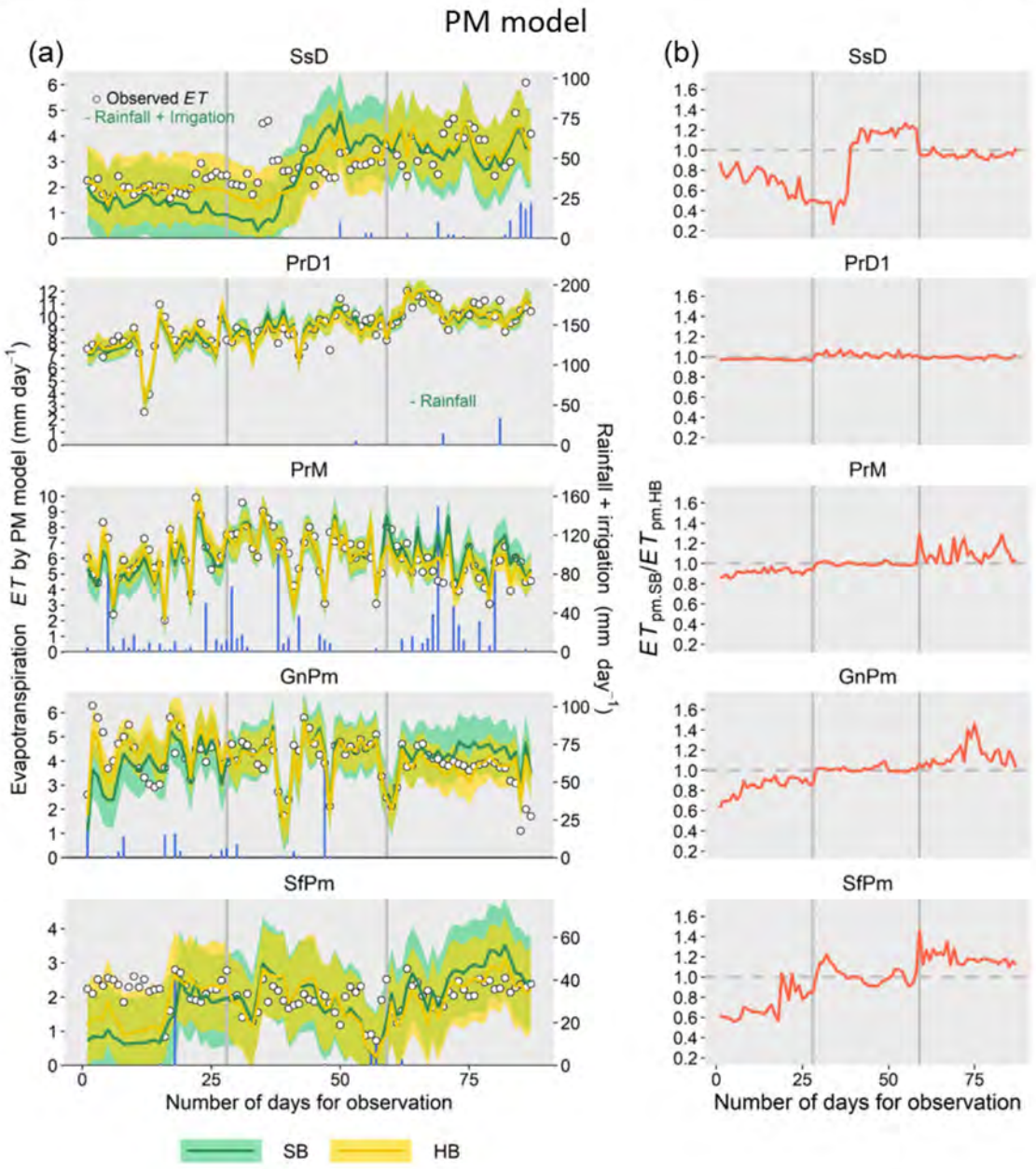

Figure 4-7 (**a**) Observed and estimated evapotranspiration (*ET*) using the Penman–Monteith (PM) model with parameters calibrated using the simple Bayesian (SB) and hierarchical Bayesian (HB) approaches. Lines and bands correspond to the posterior means and credible intervals at the 95% probability, respectively, in all five observation conditions. Vertical bars indicate the rainfall + irrigation amount for the SsD, and rainfall only for the others. (b) Variations in the values of *ET*pm.SB and *ET*pm.HB calculated from *ET* estimates by the PM model using SB and HB. The three calibration periods for HB are separated by vertical lines.

Table 4-4 Observed and estimated evapotranspiration (*ET*) with partitioned evaporation (*E*) and transpiration (*T*) using the Shuttleworth–Wallace (SW) and the Penman–Monteith (PM) models with parameters calibrated using simple Bayesian (SB) and hierarchical Bayesian (HB) approaches, and statistical criteria under five observation conditions.

Model	Bayes Type	Condition	ET_{ob} (mm)	ET_{est} (mm)	E_{est} (mm)	T_{est} (mm)	MAE (mm d^{-1})	RMSE (mm d^{-1})	MAPE (%)	RMSPE (%)
SW	SB	SsD	248	253	182	71	0.275	0.388	0.099	0.120
		PrD1	798	783	110	673	0.562	0.684	0.065	0.087
		PrM	529	516	43	473	0.663	0.825	0.112	0.142
		GnPm	350	339	89	250	0.371	0.499	0.110	0.141
		SfPm	180	179	124	55	0.239	0.309	0.117	0.170
	HB	SsD	248	248	213	35	0.218	0.294	0.074	0.089
		PrD1	798	784	94	690	0.557	0.679	0.065	0.086
		PrM	529	506	43	463	0.642	0.786	0.106	0.140
		GnPm	350	342	78	264	0.341	0.464	0.103	0.133
		SfPm	180	179	129	49	0.205	0.272	0.102	0.153
PM	SB	SsD	248	217	–	–	0.921	1.17	0.333	1.37
		PrD1	798	796	–	–	0.529	0.657	0.062	0.077
		PrM	529	528	–	–	0.731	0.927	0.125	0.151
		GnPm	350	352	–	–	0.608	0.878	0.180	0.291
		SfPm	180	163	–	–	0.661	0.838	0.317	1.01
	HB	SsD	248	236	–	–	0.587	0.824	0.197	0.435
		PrD1	798	797	–	–	0.497	0.615	0.058	0.073
		PrM	529	527	–	–	0.597	0.737	0.102	0.126
		GnPm	350	355	–	–	0.484	0.675	0.147	0.177
		SfPm	180	163	–	–	0.535	0.669	0.266	0.627

Notes: ET_{ob} and ET_{est} indicate observed *ET* and estimated *ET* using the SW and PM models, respectively. E_{est} and T_{est} are the estimated *E* and *T*, respectively, using the SW model. MAE, mean absolute error; RMSE, root mean square error; MAPE, mean absolute percentage error; RMSPE, root mean square percentage error.

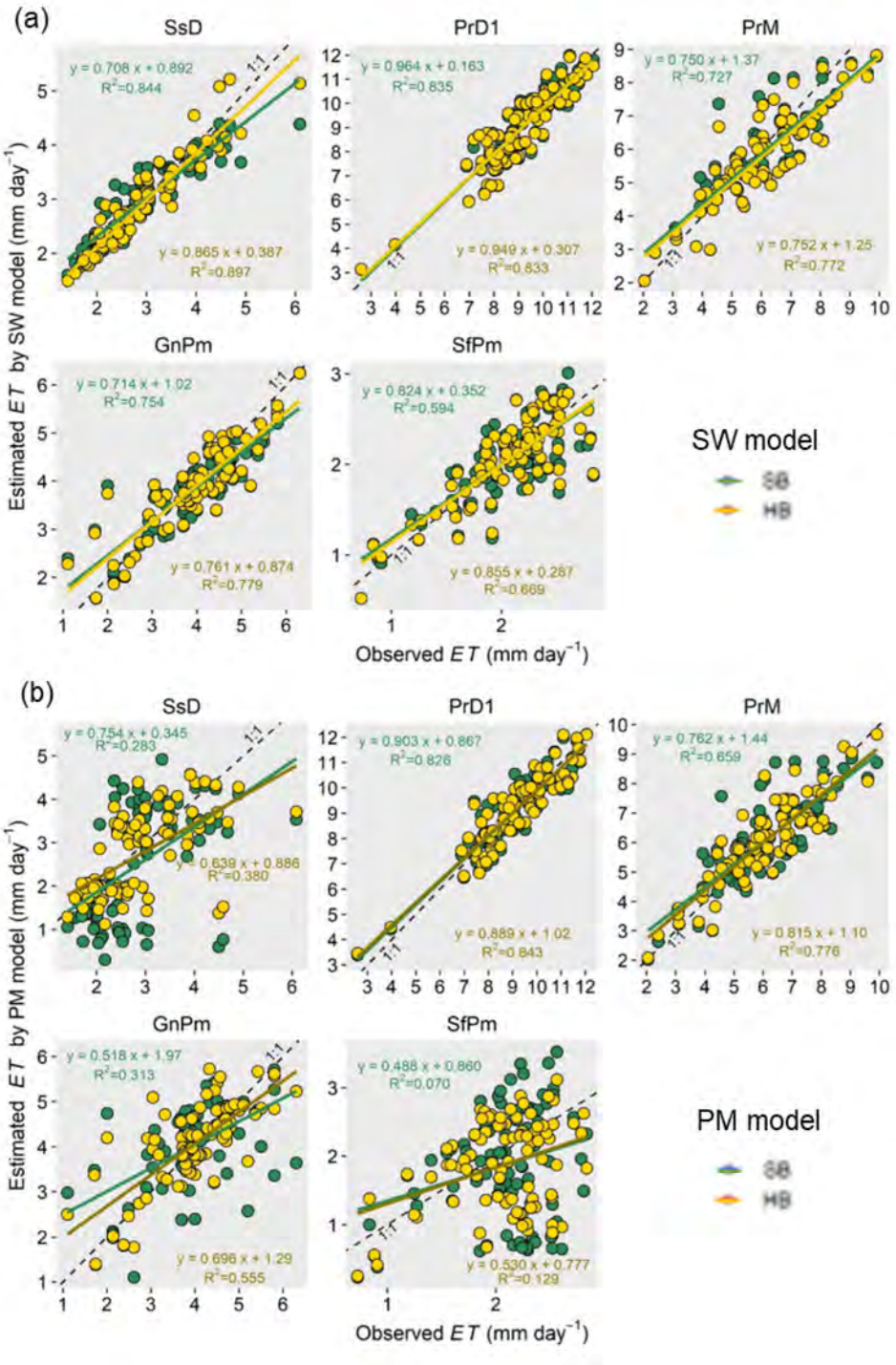

Figure 4-8 Regression analysis of observed and estimated evapotranspiration (*ET*) produced by (a) the Shuttleworth–Wallace (SW) and (b) the Penman–Monteith (PM) models with parameters calibrated using simple Bayesian (SB) and hierarchical Bayesian (HB) approaches at five observation conditions. R^2, coefficient of determination.

4.4.2.4. Validation of Model *ET* Estimation

Applying the posterior mean values of the parameters generated by the SB and the HB approaches using the dataset of PrD1, the model performance of the SW and the PM models were validated using the dataset of PrD2 as shown in Figure 4-8.

The *ET* estimates of the SW model were approximately equal to the observed *ET*, except during the initial stage, and there were few differences in the estimated *ET* using parameters calibrated by the SB and the HB approaches. The PM model overestimated *ET* in the last half period, and the estimated *ET* using parameters obtained using the HB approach was slightly larger than those obtained using the SB approach. Numerous studies have shown that the two-layer SW model has higher performance for *ET* estimation than other *ET* models, a finding consistent with those of our study. These studies have confirmed that the differences in the model structure by which *ET* is partitioned into *E* and *T* is related to the model performance [35, 36, 113–116]. The *ET* estimation of the SW model with parameters calibrated using the Bayesian approaches was acceptable for the paddy field condition, suggesting the usefulness of the two-layer SW model. The low level of difference between the SB and HB approaches in the *ET* estimation of the SW model may be related to the small environmental fluctuations in the calibration period (PrD1).

The overestimation of *ET* by the PM model in this study agrees with the results of several previous studies [31, 116], but some studies have found that the difference between the SW and PM models is not significant [30, 117]. Generally, the performance of *ET* model is strongly related to the surface resistance, which is calculated as the integration of the canopy and soil surface resistances, and reflects the effects of soil moisture and variation in LAI [118]. Some studies [114] reported that when the surface resistance in the PM model is lower than the observed resistance, the PM model overestimates *ET*. Thus, this overestimation in this study indicates an inadequate parameter estimation of the surface resistance, affected by the model structure of the PM model. The estimated mean value of r_s^c in the PM model using the parameters from the HB approach was slightly lower (54 m s^{-1}) than that from the SB approach (69 m s^{-1}) during the last half period. The posterior means of r_{STmin} for PrD1 generated by the SB and HB approaches were 52 m s^{-1} and 47 m s^{-1}, respectively, and those of other parameters also differed slightly between the SB and HB approaches. Since the validation was performed using only the dataset of the paddy field conditions, the validity of the HB approach must be further verified using calibration data including large seasonal fluctuations and variations in crop growth.

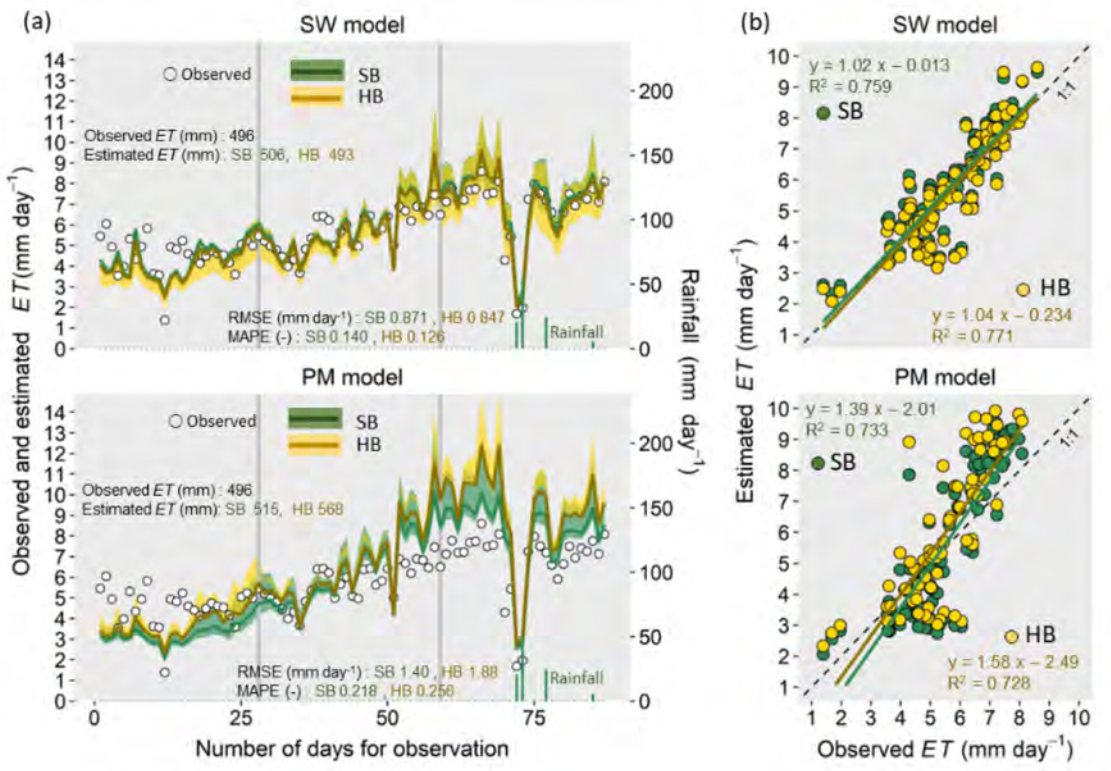

Figure 4-9 (**a**) Comparison of observed evapotranspiration (*ET*) for the paddy rice field in the dry season 2017 (PrD2) and estimated *ET* produced by the Shuttleworth–Wallace (SW) and the Penman–Monteith (PM) models with calibrated parameters using the simple Bayesian (SB) and hierarchical Bayesian (HB) approaches for the paddy rice field in the dry season 2019 (PrD1). Lines and bands indicate the mean values and 95% credible intervals of the estimated *ET*. (**b**) Regression analysis of estimated *ET* calculated by the SW and the PM models using calibrated parameters of PrD1 with observed *ET* of PrD1. RMSE, root mean square error; MAPE, mean absolute percentage error; R^2, coefficient of determination.

4.5. Conclusions

In this study, we assessed the estimation of *ET* and the parameters of the SW and PM models calibrated using SB and HB approaches, based on a field-based *ET* dataset collected from five agricultural fields over three seasons in Myanmar. The main conclusions were as follows:

Parameterization using the SB and HB approaches was, in most cases, successful in reducing the uncertainties in the parameters. Using the HB approach to parameter estimation, we identified the parameters which are sensitive to seasonal fluctuations and differences in crop growth stages. The parameter k_3, which is related to the water vapor pressure deficit, was not very susceptible to seasonal fluctuations, while r_{STmin}, which is related to stomatal resistance, was sensitive to variations in observation conditions. In the calibration of model parameters, the statistical criteria for all conditions observed indicated that the models with parameters calibrated using the HB approach had a better fit to the observed *ET* data than those with parameters calculated using the SB approach, indicating the potential importance of seasonal fluctuations and variability in crop growth stages for the calibration of model parameters. The performance of the SW models was superior to that of the PM model for most of the observation conditions, using both the SB and HB approaches. The SW model with parameters calculated using the SB and HB approaches with only observed *ET* data could provide an acceptable estimation of the *ET.* The PM model with parameters calculated using both SB and HB approaches overestimated the *ET* in the last half period, and the *ET* estimates for the HB approach were slightly overestimated compared with the SB approach.

A.1. Aerodynamic Resistances

The bulk boundary layer resistance of the vegetative elements in the canopy (s m^{-1}) (r_a^c) can be estimated by the following equation [103, 119]:

$$r_a^c = \frac{r_b}{\mathrm{LAI}} \tag{A4-1}$$

where r_b is mean boundary layer resistance. Typical values measured in the field are 25 s m^{-1} [120, 121].

The two aerodynamic resistance values for between the canopy height and reference level (s m^{-1}) (r_a^a) and for between the soil surface and canopy height (s m^{-1}) (r_a^s) can be calculated as in [103]:

$$r_a^a = \frac{\mathrm{LAI}}{4} r_a^a(\alpha) + \frac{4 - \mathrm{LAI}}{4} r_a^a(0) \qquad (0 \le \mathrm{LAI} \le 4) \tag{A4-2}$$

$$r_a^s = \frac{\mathrm{LAI}}{4} r_a^s(\alpha) + \frac{4 - \mathrm{LAI}}{4} r_a^s(0) \qquad (0 \le \mathrm{LAI} \le 4) \tag{A4-3}$$

$$r_a^a = r_a^a(\alpha) \qquad (\mathrm{LAI} > 4) \tag{A4-4}$$

$$r_a^s = r_a^s(\alpha) \qquad (\mathrm{LAI} > 4) \tag{A4-5}$$

$$r_a^a(0) = \frac{\ln^2(z/z_0')}{k^2 u_*} - r_a^s(0) \tag{A4-6}$$

$$r_a^s(0) = \frac{\ln(z/z_0')\ln\{(d+z_0)/z_0'\}}{k^2 u_*} \tag{A4-7}$$

$$r_a^a(\alpha) = \frac{\ln\{(z-d)/z_0\}}{k^2 u_*}\left[\ln\{(z-d)/(h_c-d)\} + \frac{h_c}{n(h_c-d)} \times [\exp[n\{1-(d+z_0)/h_c\}] - 1]\right] \tag{A4-8}$$

$$r_a^s(\alpha) = \frac{\ln\{(z-d)/z_0\}}{k^2 u_*}\frac{h_c}{n(h_c-d)}\left[\exp n - \exp[n\{1-(d+z_0)/h_c\}]\right] \tag{A4-9}$$

where $r_a^a(\alpha)$ and $r_a^s(\alpha)$ are value of r_a^a and r_a^s for a crop with complete canopy cover (LAI = 4) (s m^{-1}), respectively; $r_a^a(0)$ and $r_a^s(0)$ are values of r_a^a and r_a^s for bare soil (s m^{-1}), respectively; z is the reference height above the crop where meteorological measurements are available (2 m); h_c is plant height (m); d is zero plane displacement, usually estimated as $d = 0.63 \cdot h_c$; z_0 is roughness length of the crop, which can be calculated as $z_0 = 0.13 \cdot h_c$; z_0' is effective roughness length of bare soil (0.01 m); n is extinction coefficient of the eddy diffusion (2.5 [122]); and u_* is the friction velocity (m s^{-1}), which is given by $u_* = ku/\ln\{(z–d)/z_0\}$ where k is von Karman's constant (0.41) and u is wind speed (m s^{-1}).

Chapter 5. Determination of Crop Coefficient

Evapotranspiration and Crop Coefficient of Ratoon Rice Crop Determined by Water Depth Observation and Bayesian Inference

5.1. Introduction

Global rice production is projected to increase by 116 million tons by 2035 to meet the growing demand of an increasing population [123]. However, cultivated rice land has declined in recent years because of urbanization, industrialization, and stagnant rice prices [124]. Multiple rice cropping, which includes double- or triple-cropping and requires frequent rice harvesting on the same land, is one strategy to solve land shortages [125]. However, labor shortages and rising labor costs are limiting factors [126]. Ratoon rice double-cropping (main crop [MC] and ratoon), which refers to producing a second rice crop from the residual stubble after the MC harvest, is useful as an alternate option to replace conventional double-cropping [127]. Although the annual yield of ratoon double-cropping is lower than conventional double-cropping, labor and production costs can be reduced. The annual net profit could be higher or equivalent to conventional double-cropping [128, 129].

Moreover, the amount of irrigation water for ratoon crops (RCs) can be significantly reduced. The water utilization efficiency can be improved compared to the MC because the ratoon cropping has a short growth period and does not require irrigation for land preparation [130–134]. The growth period of ratoon is shorter by 40%–60% than that of the MC [135–137]. The amount of irrigation water for land preparation has been observed at 100–500 mm [138, 139], or 25% of the total water demand [140]. Therefore, there is a significant difference in the irrigation period and the amount of irrigation water required between ratoon and conventional double-cropping. Although there are many reports on evapotranspiration (*ET*) and crop coefficient (*Kc*) of single rice cropping [141–144], few studies have reported on *ET* estimation and *K*c of ratoon double-cropping. Furthermore, complex and expensive observation systems such as weighing lysimeter and the eddy covariance system are commonly used for the estimation of *ET* and *Kc*.

In Myanmar, rice is a vital crop grown in 34% of the country's total cultivated area [145]. Rice dominates the agricultural sector, the largest and most productive sector in Myanmar's economy. However, the sector is crippled by labor [146] and water shortages, particularly in the dry season [147], driving the need for a water-saving cropping system. Hence, this study on water usage in ratoon double-cropping is critical in Myanmar, because it has the potential to reduce labor costs and improve WP.

Therefore, the objective of this study was to determine the *ET* and *K*c of ratoon double-

cropping in a tropical climate region of Myanmar using a simple method. In addition, we inferred the water productivity (WP) and viability of practicing ratoon cropping in Myanmar.

5.2. Materials and Methods

5.2.1. Study site and concrete tank paddy experiment

The study site is in an experimental field at the Department of Agricultural Research (latitude 19.825, longitude 96.274), Ministry of Agriculture, Livestock and Irrigation, Myanmar, located in Zayarthiri Township in the Naypyidaw Union Territory at an elevation of 100 m above mean sea level. The study experiment used 10 concrete tanks with inside size of 1.62 m L × 0.84 m W × 0.4 m D, rice was planted in eight tanks for conventional transplanted rice and ratoon rice crops (four replications), and two tanks without plants to measure evaporation were used (two replications) (Figure 5-1). The difference in daily pond water depth (WD) (mm) above the soil surface in a concrete tank was used to determine daily crop evapotranspiration (ET_{tank}) (mm day^{-1}) and evaporation (E_{tank}) (mm day^{-1}). Net radiation, air temperature, relative humidity, air pressure and wind speed, were measured at a paddy field near the concrete tank experiment.

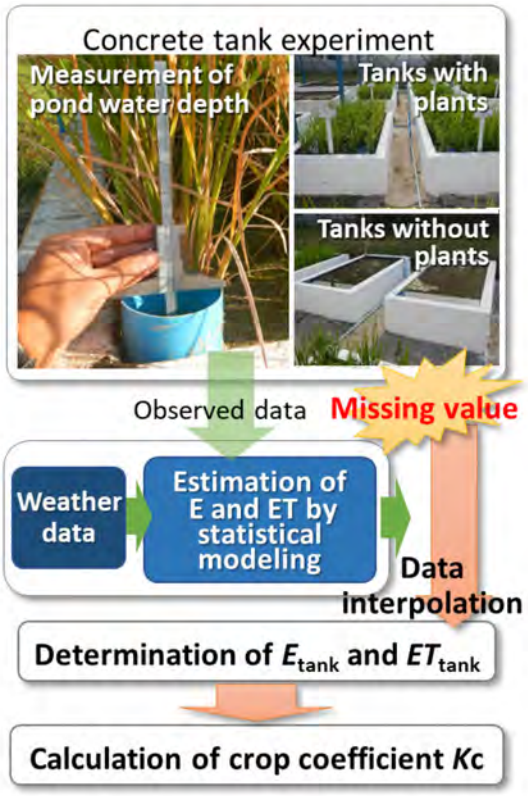

Figure 5-1 Calculation procedure for crop coefficient *K*c to determine evaporation and crop evapotranspiration from the difference in daily pond water depth above the soil surface in a tank.

5.2.2. Ratoon double-cropping in different seasons

The rice (*Oryza sativa* L.) cultivar used was “Theehtetyin” (indica), a popular variety in Myanmar with normal crop duration of 110–115 days from sowing to harvesting. Forty-five plants (approximately 21-day-old seedlings, BBCH-scale= 14) were transplanted with 20 × 20 cm spacing in nine rows and fine lines in the tank. A basal level of triple superphosphate fertilizer (18.5 kg P ha^{-1}) was applied before transplanting for the MC and two weeks before cutting the ratoon crop. Nitrogenous fertilizer (87 kg N ha^{-1}) and potash (31 kg K ha^{-1}) were applied equally to each tank at approximately 7, 30, and 50 days after transplanting and during the flowering period for the MC, and the ratoon crop was dosed at around 14, 30, and 50 days after cutting of the MC and at the flowering stage (BBCH-scale= 61).

The first trial of ratoon double-cropping planted in eight tanks, which are main crop1 (MC1) and ratoon1 (RC1), was from February 2019 to September 2019, and the second trial (MC2 and RC2) planted in eight tanks, was implemented from September 2019 to March 2020. In parallel with RC cropping, the transplanted rice (TC) planted in four tanks, was prepared in each trial to compare plant growth and the *ET* (Table 5-1 and Figure 5-2). Water management for the tank experiments was performed by continuously flooding until around 14 days before harvesting. The stem cutting of MC for ratooning was implemented at 5 cm height above the soil surface. The harvesting day at the physiological maturity stage (BBCH-scale= 87) was determined as approximately 25 days after the flowering day (BBCH-scale= 65). Myanmar has a typical tropical monsoon climate with three seasons: the hot and dry summer (i.e., March to May), the monsoon (i.e., June to September), and the cool and dry season (i.e., December to February).

Table 5-1 Cultivation information for transplanting and ratoon rice cropping.

Crop	Sowing date	Transplanting date	Harvesting date
First trial			
Main crop1 (MC1)	15 Feb 2019	7 Mar 2019	1 Jun 2019
Ratoon1 (RC1)	–	–	26 Aug 2019
Transplant1 (TC1)	24 May 2019	14 Jun 2019	10 Sept 2019
Second trial			
Main crop2 (MC2)	6 Sept 2019	25 Sept 2019	12 Dec 2019
Ratoon2 (RC2)	–	–	1 Mar 2020
Transplant2 (TC2)	30 Nov 2019	19 Dec 2019	1 Apr 2020

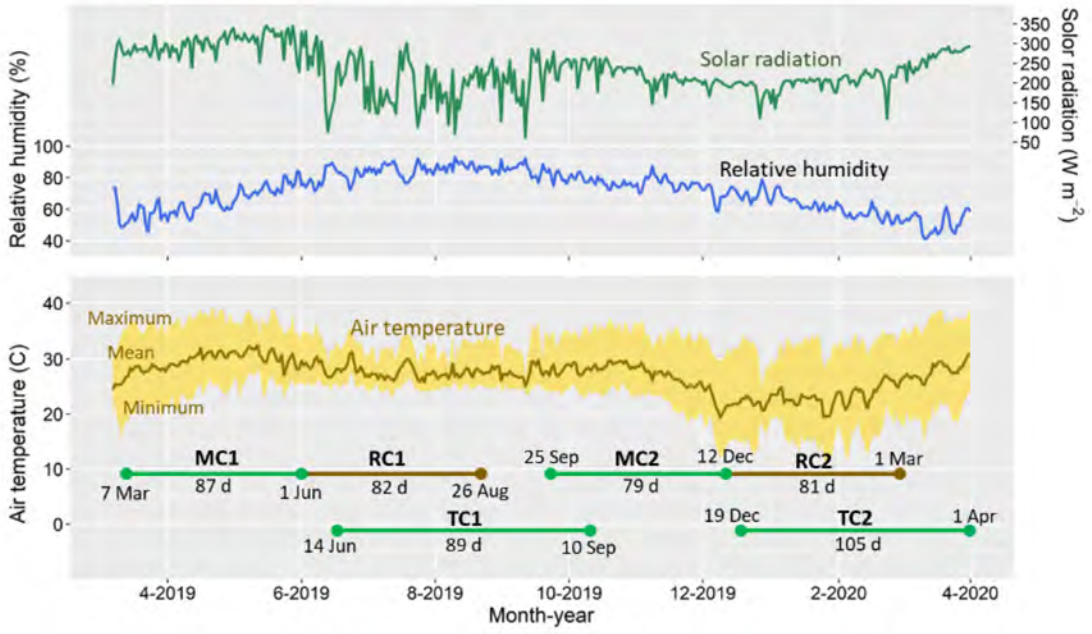

Figure 5-2 Cropping periods for the main crop (MC), ratoon (RC), and transplanted crop (TC) in the first and second trials. Daily solar radiation (W m^{-2}), relative humidity (%), and air temperature (℃) are shown lines and bands correspond to mean, maximum and minimum values from February 2019 to March 2020. The growth periods (d) are calculated from transplanting or stem cutting to harvesting.

5.2.3. Measurements of rice crop and calculation of WP

We measured plant growth (i.e., height of the plant and number of tillers), number of spikelets per panicle, filled grain weight, 1000-grain weight, weight of dried straw, and biological yield from four adjacent hills, excluding the outer hills in each tank. Grain weight was adjusted to 14% moisture content. Biological yield (g m^{-2}) was equal to the weight of dried straw and filled grains weight divided by the area of the four hills. Grain yield (g m^{-2}) and number of panicles (g m^{-2}) were determined on the basis of 21 harvested hills in seven rows and three lines. The WP of the rice crop regarding evapotranspiration (WP_{ET}) was defined as the ratio of the grain yield to the ET_{tank} (grain yield/ET_{tank}) (kg m^{-3}).

5.2.4. Determination of E_{tank}, ET_{tank}, and Kc

The daily E_{tank} and ET_{tank} were determined as follows: 1) by observing pond WD in every concrete tank above the soil surface at 7 AM every day and calculating E_{tank} and ET_{tank} from the daily difference in WD; 2) using the modified *E* and *ET* model with Bayesian inference approach; 3) interpolating missing and error observation data by the model estimates for determination; 4) by calculating *K*c, defined as the ratio of the ET_{tank} to the E_{tank} (ET_{tank}/E_{tank}). The determination period of E_{tank} and ET_{tank} was the irrigation period, in other word, the time from transplanting or cutting the stem to 14 days before harvesting.

5.2.4.1. Manual observation of E_{tank} and ET_{tank}

The WD (mm) in every tanks were observed at every morning using a depth gauge by manual reading (Figure 5-1). The ET_{tank} and E_{tank} (mm day^{-1}) were determined by the daily difference of pond WD. The amount of water lost through percolation and surface runoff, and the amount of irrigation water applied were neglected because the concreate tank cannot be penetrated and there is no runoff, and we observed the WD at two times before and after both irrigations. Moreover, when it rains, monitoring the amount of rainfall pouring into a tank is difficult, so that observed data with 5 mm daily precipitation or more were not used. On the other hand, precipitation less than 5 mm was regarded as negligible. In addition, for inferring the differences in the microclimate between paddy fields and concrete paddy tanks, we compared the daily reference crop evapotranspiration by FAO-56 (ET_0) (mm day^{-1}) with the E_{tank}. The ET_0 expresses the evaporation power of the atmosphere at a specific location and time of the year, regardless of crop characteristics and soil factors [21], and was calculated as:

$$ET_0 = \frac{0.408\Delta R_n(R_n - G) + \gamma \frac{900}{T_a + 273} u_2(e_s(T_a) - e)}{\Delta + \gamma(1 + 0.34u_2)} \quad (4\text{-}1)$$

where, R_n is the net radiation (W m^{-2}); G is the soil heat flux (W m^{-2}) that was not used because of the daily analysis (G = 0); Δ is the slope of the saturation water vapor pressure curve at the mean air temperature (kPa ℃$^{-1}$); γ is the psychrometric constant (approximately 0.066 kPa ℃$^{-1}$); u_2 is the wind speed at 2 m height (m s^{-1}); e is mean water vapor pressure (kPa) and e_s is the water vapor pressure at the evaporating surface at air temperature T_a (kPa).

5.2.4.2. Model estimation of E_{tank} and ET_{tank} for data interpolation

Many missing and error data were generated due to inconsistencies in observation such as misreading or absence of reading. Therefore, using the Bayesian inference approach, a dataset was organized to interpolate the missing data with the model estimates by the modified Penman model (P) [148] for E_{tank} (mm day^{-1}) and the Penman–Monteith (PM) model [64] for ET_{tank} (mm day^{-1}). In the modified P and PM model, adjustment parameters θ_s, which present a_1, a_2, b_1, b_2, c_1, c_2, and d, were applied for correcting the energy balance and aerodynamic resistances under the condition of the concrete tank. The modified P model expressed as

$$E_{\text{tank}} = \frac{\Delta(R_n - G)a_1}{(\Delta + \gamma)\lambda} + \frac{\gamma}{\Delta + \gamma} f(u_2)(e_s(T_a) - e) \tag{4-2}$$

$$f(u_2) = b_1 + b_2\, u_2 \tag{4-3}$$

where $f(u_2)$ is a function of the horizontal wind velocity (unitless). The modified PM model expressed as

$$ET_{\text{tank}} = \frac{\Delta(R_n - G)a_2 + C_p\rho(e_s(T_a) - e)/r_a}{\lambda\big(\Delta + \gamma(1 + r_s/r_a)\big)} \tag{4-4}$$

$$r_a = \frac{\ln\left(\frac{2.0 - d}{Z_{0m}}\right)\ln\left(\frac{2.0 - d}{Z_{0h}}\right)}{K^2 u_2} \tag{4-5}$$

$$d = c_1\, h_c,\ Z_{om} = c_2\, h_c \text{ and } Z_{oh} = 0.1\, Z_{om} \tag{4-6}$$

$$r_s = \frac{d}{0.5LAI} \tag{4-7}$$

where C_p is the specific heat capacity of dry air at constant pressure (approximately 1.01 kJ kg^{-1} ℃$^{-1}$); ρ is the mean air density (kg m^{-3}); r_a is the aerodynamic resistance (s m^{-1}); r_s is the surface resistance (s m^{-1}); d is the zero-plane displacement height, and h_c is the crop height (m) at observation day of WD; Z_{0m} is the roughness length governing momentum transfer (m), and Z_{0h} is the roughness length governing the transfer of heat and vapor (m); K is the von Karman's constant (0.41). The value of leaf area index (LAI) was predicted from the measured crop height h_c using the following formula for typical values of field crops [149–151]:

$$\text{LAI} = \text{LAI}_{\text{max}} + 1.5 \ln(h_c) \tag{4-8}$$

The maximum LAI (LAI_{max}) were obtained from the literature are reported as 5.0 for rice [152, 153].

5.2.5. Hierarchical Bayesian approach

The θ_s were estimated by hierarchical Bayesian inference, which can take into account the variation in observation condition such as seasonal fluctuation and plant growth stage for a dataset. These results can necessarily be generalized across different conditions and groups. The probabilistic model for estimating unknown adjustment parameters (i.e., a_1, a_2, b_1, b_2, c_1, c_2, d) accommodating group-level differences (i.e., different climate conditions and crop growth stages in a dataset) in the modified P and PM model are described as follows.

$$O_{[c]}[t] \sim \text{Normal}\left(S(\theta_{s\,[c]})[t], \sigma\right) \tag{4-9}$$

$$\theta_{s\,[c]} \sim \text{Normal}\left(\theta_{s,mean}, \sigma_{\theta_s}\right) \tag{4-10}$$

where $O_{[c]}[t]$ indicates the observed E_{tank} and ET_{tank} at day t in each observation period divided evenly into four periods c (1, 2, 3, 4) for E_{tank} and three periods c (1, 2, 3) for ET_{tank} (mm day^{-1}); S [t] is the estimated E_{tank} and ET_{tank} by the modified P and PM model at day t (mm day^{-1}), and σ is the standard deviance parameter that represents the measurement error variance for ET_{tank} and E_{tank} estimates (mm day^{-1}). Normal indicates a normal distribution from which ET estimates are generated. $\theta_{s\,[c]}$ represents a prior uncertainty in the parameters of group-level c and can be described as being stochastically generated from a normal distribution of $\theta_{s,mean}$ and σ_{θ_s}; $\theta_{s,mean}$ is the overall mean distribution of each parameter in a dataset, while σ_{θ_s} is a random variable distribution that represents the difference in group level of the parameter. We assumed that the specific unknown parameters θ_s were distributed uniformly within the range of $0 \le a \le 2$, $0 \le b \le 2$, $0 \le c \le 1$, and $30 \le d \le 150$ we heuristically set.

In this study, all the simulations and calculations were performed in R version 4.0.2. For estimating the posterior distribution, we used RStan version 2.19.3 developed by the Stan Development Team [154], which employs a Markov Chain Monte Carlo (MCMC) technique to sample from the posterior distribution of a given model. We ran four MCMC chains with 20,000 iterations and monitored them to confirm that the MCMC chains converged to the target distributions. The model estimates of E_{tank} and ET_{tank} using the hierarchical Bayesian approach were evaluated by comparing with the observed using common criteria in model evaluation: the root mean squared percentage error (RMSPE) and the coefficient of determination (R^2). The R^2 is a measure of the proportion of the total variance of observed data explained by the estimated data. Non-linear regression analysis for plant growth was analyzed by a generalized additive model explained in [155]. Difference between means were compared by analysis of variance (ANOVA) test at the 5% probability level.

5.3. Results

5.3.1. Crops growth in different seasons

Plant growth were higher in the monsoon season than in the cool and dry season. The plant height of TC1 in the monsoon season was the highest, that of RC2 in the cool and dry season was the lowest, and the growth trends for plant height of TC and RC were similar (Figure 5-3a). In contrast, that for the number of tillers between TC and RC was substantially different. MC1 and TC1 tillers reached the maximum tillering stage at around 70–80 days after transplanting, and that of the RC1 reached 20 in only 7 days after cutting the stem. Many tillers of RC emerged after stem cutting. In the RC2 in the cool and dry season, tillering was active until harvesting, with a large variation of the number of tillers (Figure 5-3b).

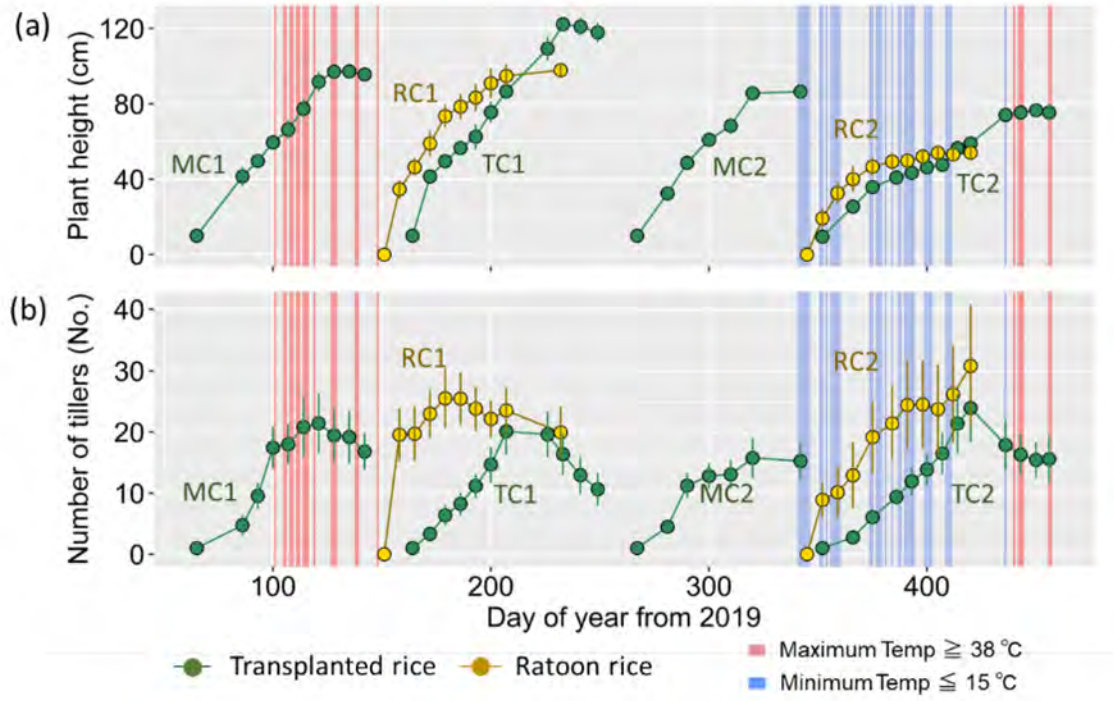

Figure 5-3 (a) Plant height and (b) number of tillers per hill of MC, RC, and TC described with points and error bars corresponding to the mean and standard deviation in the first and second double-cropping. MC, RC, and TC represent the main crop, ratoon, and transplanted rice crop, respectively. Red and blue vertical stripes indicate a day with the maximum temperature ≧ 38℃ and the minimum temperature ≧ 15℃.

Figure 5-4 shows the comparison of the plant growth of transplanted rice (i.e., MC1, TC1, MC2, and TC2) and ratoon rice (i.e., RC1 and RC2) with non-linear regression curves and 95% credible intervals. The accumulated air temperature was calculated from transplanting or cutting the stem to 14 days before harvesting. The R^2 of the transplanted rice was higher than that of the ratoon in both plant height and number of tillers. A strong correlation with the accumulated temperature was observed in the number of tillers for the transplanted rice. The transplanted rice reached the maximum tillering at around 1,500℃ accumulated temperatures. Conversely, the plant growth of the ratoon did not depend on the accumulated temperature, and the R^2 was less than 0.5.

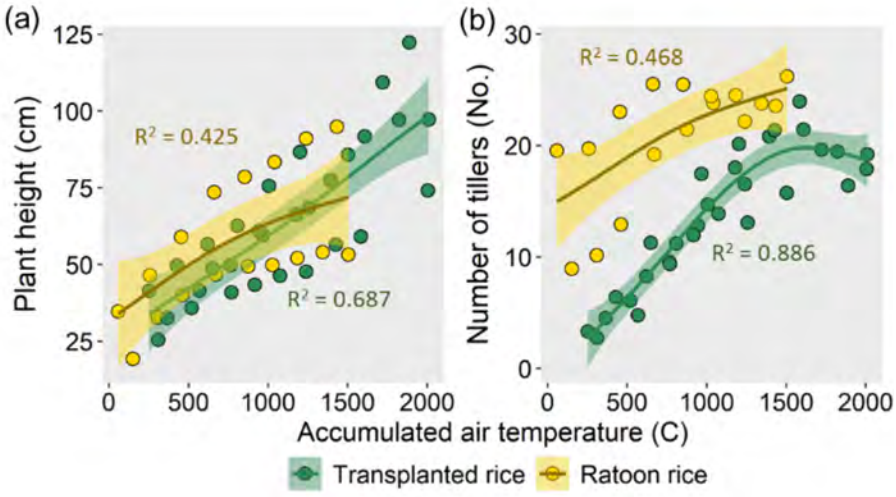

Figure 5-4 Comparison of the accumulated air temperature and (a) plant height, and (b) number of tillers per hill described with non-linear bands and 95% confidence intervals by a generalized additive model (transplanted rice: n = 29, ratoon: n = 17). Accumulated temperature was calculated from the period of transplanting or stem cutting to 14 days before harvesting. R^2, determination coefficient.

5.3.2. Rice yield components and grain yield

Table 5-2 presents the yield components and grain yield of each crop in the concrete tanks. The statistical comparison of the first and the second trial was not made due to the different seasons of the trials. For RCs, the number of panicles in both trials was significantly higher than that of the transplanted crops. The number of spikelets was significantly lower than that of the transplanted crops. The filled grains rate as well as 1000-grain weight, the biological and grain yields of RC2 were significantly lower than those of the others. This was caused by the effect of low temperature in the reproductive stage (BBCH-scale= 51–69) of RCs. Spikelet fertility of the rice decreased, because the rapidly growing booting and reproductive tissues are highly sensitive to low temperatures [156]. The grain yield of RC1 was 20% lower than MC1 and identical with TC1 cultivated in parallel with RC1. However, the yield of RC2 was 39% of that for MC2, exhibiting a significantly decrease. The highest grain yield among all crops was exhibited by TC2 together with the longest growth period.

Table 5-2. Yield components and grain yield for concrete tanks.

Crop	No. of panicles (m^{-2})	No. of spikelets (panicle^{-1})	Filled grains (%)	1000-grain weight (g)	Biological yield (g m^{-2})	Grain yield (g m^{-2})
First trial						
Main crop1 (MC1)	$377^{b} \pm 52$	$142^{b} \pm 23$	$61^{a} \pm 7$	$21^{b} \pm 0.3$	$1572^{a} \pm 150$	$555^{a} \pm 133$
Ratoon1 (RC1)	$488^{a} \pm 31$	$80^{c} \pm 6$	$56^{ab} \pm 7$	$22^{a} \pm 0.4$	$1259^{b} \pm 253$	$439^{a} \pm 54$
Transplant1 (TC1)	$262^{c} \pm 17$	$174^{a} \pm 28$	$50^{b} \pm 3$	$22^{a} \pm 0.7$	$1337^{ab} \pm 211$	$426^{a} \pm 53$
Second trial						
Main crop2 (MC2)	$329^{b} \pm 21$	$115^{b} \pm 9$	$62^{a} \pm 5$	$22^{a} \pm 0.7$	$1048^{a} \pm 138$	$510^{b} \pm 54$
Ratoon2 (RC2)	$501^{a} \pm 66$	$74^{c} \pm 8$	$30^{b} \pm 10$	$19^{b} \pm 0.6$	$699^{b} \pm 103$	$197^{c} \pm 57$
Transplant2 (TC2)	$310^{b} \pm 6$	$158^{a} \pm 35$	$66^{a} \pm 11$	$20^{b} \pm 0.5$	$1109^{a} \pm 111$	$631^{a} \pm 28$

Values within one cropping and with the same letter for crops are not significantly different at $p = 0.05$ level according to Tukey's honestly significant difference test.

5.3.3. E_{tank} and ET_{tank} combined with the observation and model estimates

5.3.3.1. Model estimates of E_{tank} and ET_{tank} for data interpolation

For the E_{tank}, the mean value of the observation was 4.6 ± 1.4 mm (mean ± SD), and that of the model estimates was 4.6 ± 1.2 mm. Both mean values were almost identical, but variation in the dataset was different between the estimates and the observation, as shown in Figure 5-5a. The evaluation criterion for the model estimate was 36% for RMSPE and 0.59 for R^2. In addition, the values for ET_0 and for E_{tank} from the day of year (DOY) 66 to 280 were almost identical. However, approximately from DOY 280 when the air temperature began to drop gradually (Figure 5-2), the values for ET_0 were underestimated compared with the values for E_{tank}. We assume that the underestimated values were caused by the different surface condition at paddy field and concrete tanks after the harvest of the paddy fields. The paddy field, where the meteorological station was installed was harvested at the end of October (i.e., DOY 300). After harvesting, the field was drained and left fallow during the cool season. For the ET_{tank}, the RMSPE and R^2 explained that the model performance in the monsoon season (RC1 and TC1) was lower than other seasons, and the performance for RC was low compared to that of TC cultivated in parallel with RC (Figure 5-5b). The RC1 was the highest with RMSPE = 62% and lowest with R^2 = 0.278. In the TC1 and MC2 with an incomplete dataset, 60% and 40% data deficient, respectively, using Bayesian parameter inference approach, the ET_{tank} for TC1 and MC2 could be estimated with a performance of RMSPE = 19.6% and 22%, and R^2 = 0.462 and 0.677, respectively. The MC1 and TP2 with sufficient datasets was with R^2 = 0.809 and 0.873, respectively, which indicated that the model explained more than 80% of the variability in the observed data (Figure 5-5b).

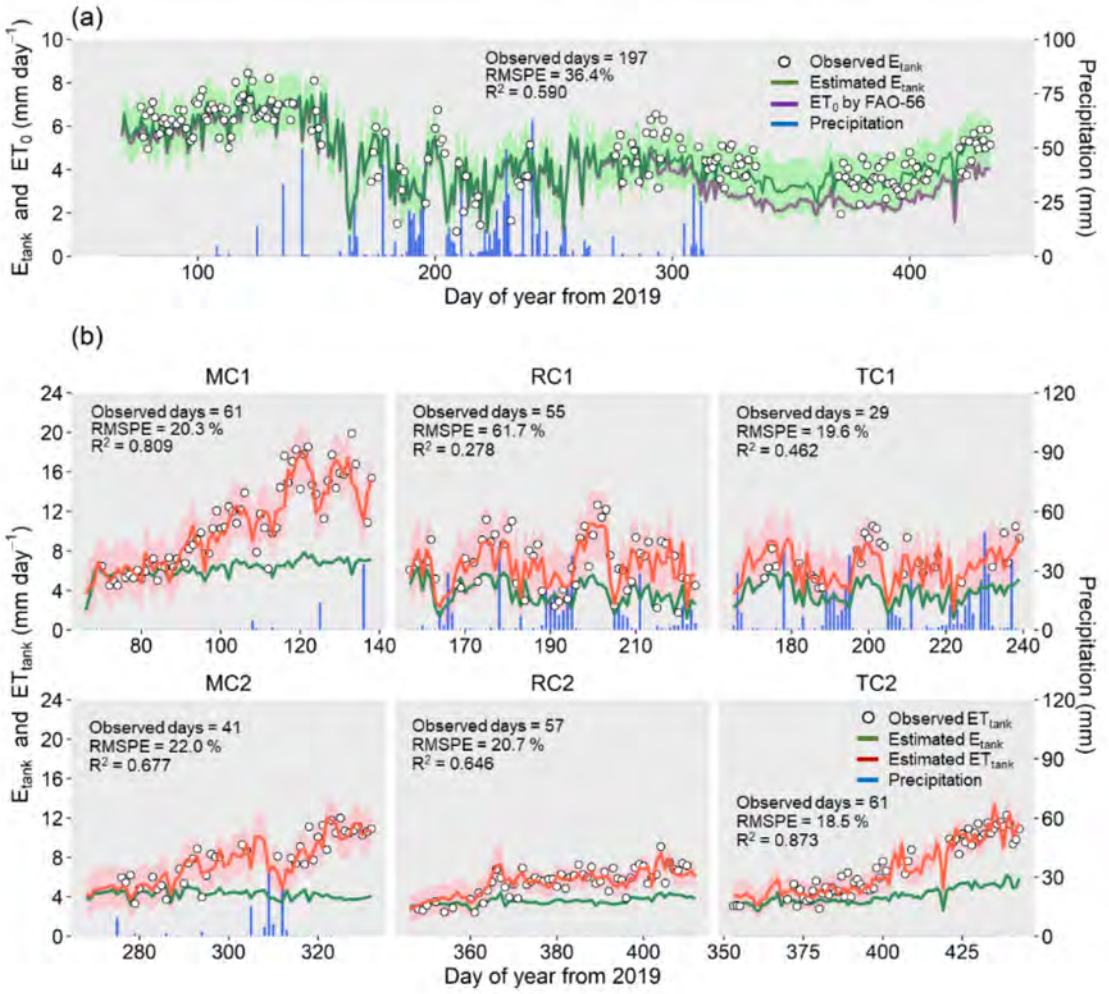

Figure 5-5 (**a**) E_{tank} and ET_0, and (**b**) ET_{tank} during the observation of water depth in a tank. The model estimates are described with lines and bands corresponding with the posterior means and 95% credible intervals. MC, RC, and TC present the main crop, ratoon, and transplanted crop, respectively. Observed days, days of observed pond water depth; RMSPE, root mean squared percentage error; R^2, determination coefficient.

5.3.3.2. Determination of E_{tank} and ET_{tank}

Summary of the E_{tank} and ET_{tank} for the model estimates and for the corrected observations are shown in Table 5-3. The total period represents the irrigated period in a tank for the observation of water depth from transplanting or cutting the stem to 14 days before harvesting. The model estimates for RC2 of E_{tank}, and TC1, MC2 and TC2 of ET_{tank} were identical with the corrected observations. For the daily mean of the E_{tank} and ET_{tank} on the corrected observations, the largest value was MC1 cultivated in the hot and dry summer, and the smallest was RC2 in the cool and dry season. And the ET_{tank} of RC1 was 59% of MC1, and RC2 was 74% of MC2. Conversely, comparing TC cultivated in parallel with RC, the ET_{tank} of RC1 was 94% that of TC1, and RC2 was 59% that of TC2. The total ET_{tank} of the first and second ratoon double-cropping was 1212 mm and 839 mm, respectively.

Table 5-2 Summary of E_{tank} and ET_{tank} for the model estimates and for the corrected observations.

Crop	Total period (days)	Model estimates				Corrected observations			
		E_{tank} (mm)		ET_{tank} (mm)		E_{tank} (mm)		ET_{tank} (mm)	
		Total	Daily mean	Total	Daily mean	Total	Daily mean	Total	Daily mean
First trial									
MC1	73	456	6.2	754	10	464	6.4	762	10
RC1	69	259	3.8	446	6.5	254	3.7	450	6.5
TC1	75	287	3.8	479	6.4	274	3.7	479	6.4
Second trial									
MC2	65	276	4.2	483	7.4	289	4.5	483	7.4
RC2	67	237	3.5	363	5.4	237	3.5	356	5.3
TC2	91	370	4.1	606	6.7	364	4.0	606	6.7

MC, RC, and TC indicate main crop, ratoon, and transplanted crop, respectively. Total period indicates the irrigated period in a tank for the observation of water depth from transplanting or cutting the stem to around 14 days before harvesting. The corrected observations represent the observed data with missing data interpolated by the model estimation.

5.3.4. Crop coefficient

Figure 5-6 shows *K*c values (ET_{tank}/E_{tank}) described with non-liner regression curves and bands corresponding to the 95% credible intervals. Target period was from transplanting or cutting the stem of the MC to 14 days before harvesting. The *K*c regression curve of all crops was approximately set in a range of 1 to 2. But the variation of *K*c value of RC1 and TC1 cultivated in the monsoon had very large compared to others, resulting in $R^2 = 0.100$ and 0.211, respectively. The *K*c regression curves of RC2 had a different shape from that of MC and TC. The regression curve of MC and TC showed a logistic curve, but that of RC2 formed a parabolic curve.

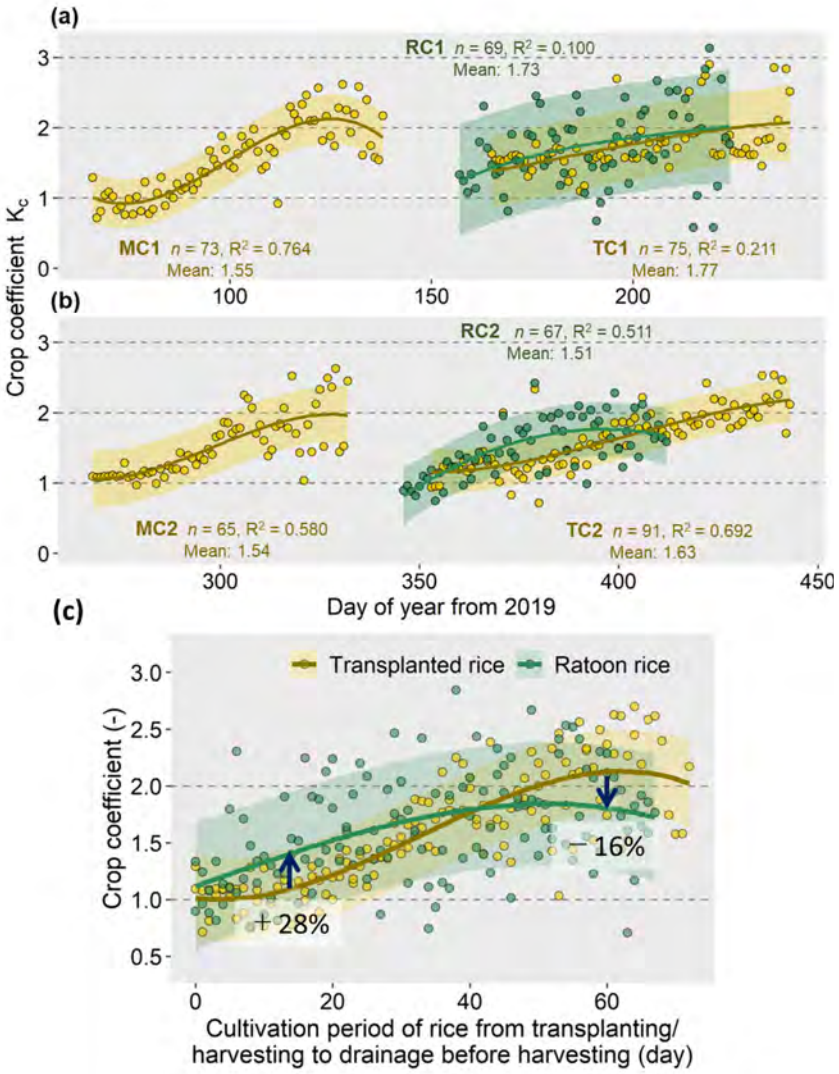

Figure 5-6 *K*c regression curves in (a) first, (b) second trial, and (c) comparing *K*c regression curves between transplatned and ratoon rice described with lines and bands corresponding to the means and 95% credible interval (i.e., the 2.5th and 97.5th percentiles). The calculation period of *K*c is from transplanting or cutting the stem of the main crop to 14 days before harvesting. *n*, number of *K*c data; R^2, determination coefficient; MC, RC, and TC present main crop, ratoon, and transplanted rice crop, respectively.

5.3.5. Water productivity

Figure 5-7 presents the comparison of the ET_{tank} and grain yield as well as grain yield and WP_{ET} for each cropping. The log approximation between the grain yield and the ET_{tank}, and the WP_{ET} and the grain yield were moderate established (R^2 = 0.558 and R^2 = 0.579, respectively). The WP_{ET} in this study ranged from 0.55 to 1.06. The MC1 cultivated in the summer season exhibited the highest ET_{tank} together with a large yield. By contrast, the WP_{ET} of MC1 was lower than that of other crops except for RC2. Regarding the ratoon, the WP_{ET} of the RC1 of the first trail was higher than that for MC1 and TC1. The WP_{ET} of the RC2 was considerably lower than that of others because of the low yield induced by the low temperatures.

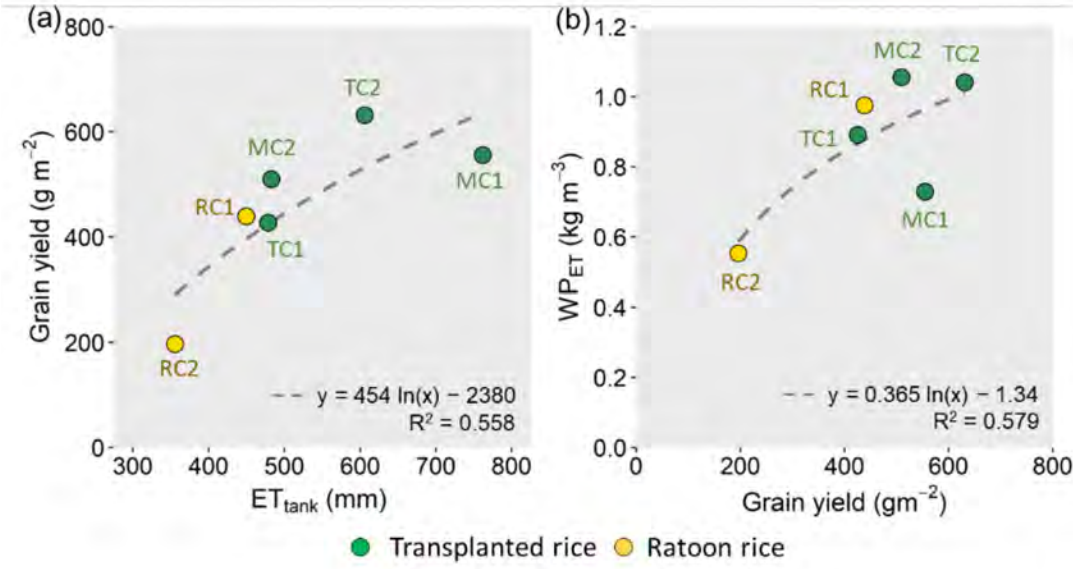

Figure 5-7 Comparison of (a) the ET_{tank} and grain yield as well as (b) the grain yield and WP_{ET} of each cropping. WP_{ET} represents water productivity with respect to the ET_{tank}. MC, RC, and TC present main crop, ratoon, and transplanted rice crop, respectively. R^2, determination coefficient.

5.4. Discussion

5.4.1. Method for *ET* determination

This study combined manual observation of the WD in concrete paddy tanks and the *ET* model estimation using Bayesian inference; this enabled the ET_{tank} to be determined with an incomplete observation dataset, around 20%–60% data deficit in total. Therefore, this method is useful when it is difficult to install a complex observation system and would be helpful when the observation error often occurs, or the observation frequency needs to be reduced.

However, for the estimation of ET_{tank} for RC, the model performance was decreased compared to that of TC. We assumed that the regression formula of the LAI could not meet the actual plant growth of RC because the tillering trait of RC was significantly different from that of the TC. Moreover, the considerable variation in the number of tillers for RC made the model estimation difficult. Since ratoon ability is a complex trait dependent on many heritable and environmental factors [134], the relationship between regeneration traits and surface resistance in modeling the *ET* of ratoon crops needs to be further developed.

5.4.2. *ET* characteristic of RC

The total ET_{tank} of RC in the two different seasons was 450 mm (RC1) and 356 mm (RC2), 59% and 74% that of MC, respectively. This reduction ratio of RC was similar to previous studies [132–134]. However, in this study, the growth period for MC and RC was nearly the same. Additionally, the daily mean of ET_{tank} for RC1 (6.5 mm) was equivalent to TC1 (6.4 mm) cultivated in parallel with RC1. In other words, it indicates that the difference in the amount of ET_{tank} between MC and RC was mainly attributed to the climate conditions in each cultivation. In most previous studies [135–137, 157], the growth period of RC was reduced to 40%–60% of MC, contributing to lowering irrigation water supply for RC, which was different from the results of this study. The factors in the growth period of RC included the effect of varieties, environmental conditions, and cultivation practices [158]. Therefore, for understanding the *ET* characteristics of ratoon cropping, the impact of different varieties and cultivation management and environment on the plant growth of RC should be investigated.

Although many studies on the *K*c of single rice cropping, few studies have reported on *K*c of ratoon cropping. In this study, the *K*c value was determined from the evaporation loss from a ponding tank and the crop evapotranspiration from a paddy tank. This result showed the different trend of *K*c values between TC2 and RC2. Since the initial tillering of RC2 was more vigorous than that of TC2, the increase rate of *K*c at the initial stage within one month for RC2 (83%) was higher than that for TC2 (20%). It is suggested that an irrigation scheduling of RC in the initial stage should take high crop water requirements into account. However, since the study on *K*c of ratoon is limited, it is essential to study on *K*c of RC under various conditions in the future.

5.4.3. Viability of practice for ratoon cropping

The ratoon rice exhibited approximately 40%–60% reduction in grain yield and growth period compared with the main crop [135–137, 159, 160]. Because of the well-established linear relationship between plant biomass and transpiration [161], the fundamental factor causing the low yield of the ratoon crop is likely due to the shorter growth period. This leads to a decrease in total transpiration and a decrease in plant biomass, which affects the sink and source capacity of the yield performance. However, in this study, the growth period of ratoon crops (RC1 and RC2) was similar to that of the transplanted rice. For this reason, the observed grain yield for RC1 was similar to that of TC1 cultivated in parallel with RC1. Moreover, the WP_{ET} in this study ranged from 0.55 to 1.06, which constitutes a larger range than those reported in previous studies (e.g., 0.19–0.29 [162]; 0.22–0.39 [163]; 0.23–0.27 [164]; 0.24–0.70 [165]; 0.30–0.33 [166]). This indicates that the rice variety and environment applied in this study might be suitable for ratoon cropping. However, because the result of this study is based on small tank cultivation, careful evaluation of plant growth and yield performance of ratoon crop in fields is necessary. Further study on ratoon in Myanmar is necessary for generating reliable recommendations for farmers.

5.5. Conclusions

Few studies on the *ET* and *K*c of ratoon rice double-cropping have been reported, and it remains difficult to observe *ET* in developing countries. Therefore, the *ET* and *K*c for ratoon cropping during 2019–2020 in the tropical region of Myanmar were determined using a simple method. The conclusions are described as follows: To determine *ET* in ratoon cropping, we combined manual observation of WD in concrete paddy tanks and the *ET* model estimation using the Bayesian inference approach. The *ET* and *K*c could be determined using this method with an incomplete observation dataset. The complex regeneration traits of ratoon affected the prediction of LAI and *ET*. The relationship between regeneration traits and surface resistance in modeling the *ET* of ratoon crops need to be further developed. The total amount of *ET* for the RC1 (450 mm) was reduced by around 60% compared to the MC1 (762 mm). However, the growth period (82 d) and the mean *ET* value (6.5 mm day^{-1}) of ratoon were similar to transplanted rice (89 d and 6.4 mm day^{-1}) cultivated in parallel with ratoon. Thus, the difference in the *ET* was mainly attributed to the difference in climate conditions in each cropping period. The *K*c regression curve between transplanted rice and RCs was different because of the tillering traits, and the increase rate of *K*c at the initial stage for RC2 (83%) was higher than that for TC2 (20%). It is suggested that irrigation scheduling of ratoon cropping in the initial growth stage should take high crop water requirements into account. The yield (439 g m^{-2}) and WP_{ET} (0.98 kg m^{-3}) of ratoon crop equivalent to the yield (426 g m^{-2}) and WP_{ET} (0.89 kg m^{-3}) of transplanted rice was observed for crops cultivated in concrete tanks. Further study on ratoon in Myanmar is essential for clarifying the viability of ratooning and for generating reliable recommendations for farmers.

Chapter 6. General Conclusions

In Myanmar, the water usage of the Yezin dam irrigation area strongly depends on the annual rainfall. Moreover, irrigation water demand competes with domestic water demand due to the population increase. Therefore, irrigation water with reduced water loss and the application of water-saving techniques are required, and the characteristic of water consumption of fields should be evaluated properly for irrigation planning. However, especially in developing countries, characterizing water consumption in practice faces many challenges due to the limitations in the observation system.

This thesis investigates the problems of observation and data analysis on water consumption of agricultural fields in Myanmar, and the characteristics of soil infiltration and *ET* are evaluated using a simple observation system with statistical modeling. The four main objectives of this thesis were studied and summarized as follows:

In Chapter 1, an overview of the Yezin dam irrigation area, Myanmar, and the problem of water shortage and water use were shown. The challenges of study on soil infiltration and *ET* were explained through a literature review.

In Chapter 2, the factors that produced negative field-saturated hydraulic conductivity (K_{fs}) in the data analysis for the infiltration test were shown, which were due to the magnitude of initial infiltration caused by drying of the soil. Additionally, an analytical method was proposed using a cumulative linearization approach of Philip's infiltration model to correct abnormal K_{fs} values. This study can contribute to field infiltration tests in evaluating the soil permeability of fields under a dry soil condition.

In Chapter 3, rejection determinations for BREB calculation flux were performed based on the objective criteria derived from instrument resolution limits and physical consideration. Moreover, meteorological conditions that produce inaccurate flux due to Bowen ratio approaching −1 and incorrect fluxes signs were shown. Specifically, for rice cultivation conditions in the dry season, 56% of the observed data were rejected, in which the majority of the rejected data occurred during nighttime, with rejection frequencies of 98%. This indicates that the BREB method cannot be applied under the conditions that the water vapor pressure gradient is positive (latent heat flux is upward) and the air temperature gradient is negative (sensible heat flux is downward), such as in a paddy field during nighttime in the dry season. Under the above observation conditions, the aerodynamic method by adding another wind speed in the BREB observation system (i.e., to observe the specific humidity and wind speed at two heights) can be suggested to estimate proper fluxes at the above conditions instead of the BREB method.

In Chapter 4, the parameters estimation of the two-layer *ET* model using Bayesian approaches was assessed to improve *ET* estimation and demonstrate the possibility of the *ET* partitioning into *E* and *T*, based on a field-based *ET* dataset collected from five agricultural fields

over three seasons. This study showed that parameterization using a hierarchical Bayesian (HB) approach was successful in reducing the uncertainties in the parameters. The statistical criteria indicated that the models with parameters calibrated using the HB approach had a better fit to the observed *ET* data than that using a simple Bayesian approach. This indicates the potential importance of seasonal fluctuations and variability in crop growth stages for the calibration of model parameters. The HB approach can take into account the variation in crop growth and seasonal fluctuations and can be a strong tool for the parameterization of the two-layer *ET* model that partitions *ET* into *E* and *T*. Thus, future studies should validate the *E* and *T* derived from the two-layer *ET* model, with parameters calibrated using the HB approach compared with direct measurement of *E* and *T*.

In Chapter 5, considering that there is an incomplete dataset due to manual observation, crop coefficient (Kc) for double rice ratoon cropping was determined using *ET* model estimation with parameters calibrated by the HB approach. Even in developing countries, the *ET* and Kc of rice plants could be determined using this method without installing an expensive observation system. Moreover, it was shown that the Kc regression curve between transplanted and ratoon crops was different due to the different tillering traits among crops, and the increase rate of Kc at the initial stage for ratoon crops was higher than that for transplanted rice. It is suggested that irrigation scheduling of ratoon cropping in the initial growth stage should take into account high crop water requirements.

Especially in developing countries, there are various restrictions for field measurement and data analysis on the water consumption of agricultural fields. The results can contribute to evaluating the characteristics of water consumption for improving irrigation planning, especially developing countries.

References

[1] Chow V, Maidment D, Mays, L (1988) Applied hydrology, 572 pp, Editions McGraw-Hill, New York.

[2] Philip JR (1957) The theory of infiltration: 4. Sorptivity and algebraic infiltration equations. Soil Sci 84(3):257–264. https://doi.org/10.1097/00010694-195709000-00010.

[3] Jačka L, Pavláseka J, Pavel P, Kuráž V (2016) Assessment of evaluation methods using infiltration data measured in heterogeneous mountain soils. Geoderma 276:74–83. https://doi.org/10.1016/j.geoderma.2016.04.023.

[4] Watson KK (1959) A note on the field use of a theoretically derived infiltration equation. J Geophys Res 64(10):1611–1615. https://doi.org/10.1029/JZ064i010p01611

[5] Maheshwari BL, Turner AK, McMahon TA, Campbell BJ (1988) An optimization technique for estimating infiltration characteristics in border irrigation. Agric Water Manag 13(1):13–24. https://doi.org/10.1016/0378-3774(88)90129-1

[6] Williams T, Kelley C (2017) Gnuplot 5.0, An interactive plotting program. Gnuplot homepage web. http://gnuplot.sourceforge.net. Accessed 15 June 2018

[7] Hillel D (1980) Applications of soil physics. Academic Press, New York

[8] Jaynes RA, Gifford GF (1981) An In-depth examination of the Philip equation for cataloging infiltration characteristics in rangeland environments. J Range Manage 34(4):285–296. https://dx.doi.org/10.2307/3897853

[9] Fahad AA, Mielke LN, Flowerday AD, Swartzendruber D (1982) Soil physical properties as affected by soybean and other cropping sequences. Soil Sci Soc Am J 46(2):377–381. https://doi.org/10.2136/sssaj1982.03615995004600020033x

[10] Bonell M, Williams J (1986) The two parameters of the Philip infiltration equation: Their properties and spatial and temporal heterogeneity in a red earth of tropical semi-arid Queensland. J Hydrol 87(1–2):9–31. https://doi.org/10.1016/0022-1694(86)90112-5

[11] Berndtsson R (1987) Application of infiltration equations to a catchment with large spatial variability in infiltration. Hydrol Sci J 32(3):399–413. https://doi.org/10.1080/02626668709491197

[12] Serralheiro RP (1995) Furrow irrigation advance and infiltration equations for a Mediterranean soil. J Agric Engng Res 62(2):117–126. https://doi.org/10.1006/jaer.1995.1070

[13] Shukla MK, Lal R, Unkefer P (2003) Experimental evaluation of infiltration models for different land use and soil management systems. Sil Sci 168(3):178–191. https://doi.org/10.1097/01.ss.0000058890.60072.7c

[14] Machiwal D, Jha MK, Mal BC (2006) Modelling infiltration and quantifying spatial soil variability in a wasteland of Kharagpur, India. Biosyst Eng 95(4):569–582.

https://doi.org/10.1016/j.biosystemseng.2006.08.007

[15] Zadeh KS, Shirmohammadi A, Montas HJ, Felton G (2007) Evaluation of infiltration models in contaminated landscape. J Environ Sci Heal A 42(7):983–988. https://doi.org/10.1080/10934520701373000

[16] Fodor N, Sándor R, Orfanus T, Lichner L, Rajkai K (2011) Evaluation method dependency of measured saturated hydraulic conductivity. Geoderma 165(1):60–68. https://doi.org/10.1016/j.geoderma.2011.07.004

[17] Liu H, Lei TW, Zhao J, Yuan CP, Fan YT, Qu LQ (2011) Effects of rainfall intensity and antecedent soil water content on soil infiltrability under rainfall conditions using the run off-on-out method. J Hydrol 396(1–2):24–32. https://doi.org/10.1016/j.jhydrol.2010.10.028

[18] Fashi FH, Sharifi F, Kamali K (2014) Modelling infiltration and geostatistical analysis of spatial variability of sorptivity and transmissivity in a flood spreading area. Span J Agric Res 12(1):277–288. https://doi.org/10.5424/sjar/2014121-4659

[19] Aubinet M, Vesala T, Papale D (2012) Eddy covariance: A practical guide to measurement and data analysis, Springer, Heidelberg, New York, 438 pp

[20] Evett SR, Schwartz RC, Howell TA, Louis BR, Copeland KS (2012) Can weighing lysimeter ET represent surrounding field ET well enough to test flux station measurements of daily and sub-daily ET? Adv Water Resour 50: 79–90. http://dx.doi.org/10.1016/j.advwatres.2012.07.023

[21] Allen RG, Pereira LS, Raes D, Smith M (1998) Crop evapotranspiration: guidelines for computing crop water requirements. FAO irrigation and drainage paper 56. Rome. http://www.fao.org/docrep/X0490E/x0490e00.htm#Contents (Accessed 9 July 2019).

[22] Farg E, Arafat SM, Abd El-Wahed MS, EL-Gindy AM (2012) Estimation of Evapotranspiration ETc and Crop Coefficient Kc of Wheat, in south Nile Delta of Egypt Using integrated FAO-56 approach and remote sensing data. Egyp J Remo Sen Spa Scie. 15(1): 83–89. https://doi.org/10.1016/j.ejrs.2012.02.001.

[23] Bowen IS (1926) The ratio of heat losses by conduction and by evaporation from any water surface. Phys Rev 27(6):779–787. http://doi.org/10.1103/PhysRev. 27.779

[24] Hu S, Zhao C, Li J, Wang F, Chen Y (2014) Discussion and reassessment of the method used for accepting or rejecting data observed by a Bowen ratio system. Hydrol Process 28(15):4506–4510. https://doi.org/10.1002/hyp.9962

[25] Zhang C, Yan H, Shi H, Sugimoto H (2013) Study of crop coefficient and the ratio of soil evaporation to evapotranspiration in an irrigated maize field in an arid area of Yellow River Basin in China. Meteorol Atmos Phys 121:207–214. https://doi.org/10.1007/s00703-013-0264-6

[26] Odhiambo LO, Irmak S (2011) Performance of extended Shuttleworth–Wallace model for estimating and partitioning of evapotranspiration in a partial residue–covered subsurface drip–irrigated soybean field. Trans ASABE 54:915–930

[27] Anadranistakis M, Liakatas A, Kerkides P, Rizos S, Gavanosis J, Poulovassilis, A (2000) Crop water requirements model tested for crops grown in Greece. Agr Water Manage 45:297–316. https://doi.org/10.1016/S0378-3774(99)00106-7

[28] Gardiol JM, Serio LA, Maggiora AD (2003) Modelling evapotranspiration of corn (Zea mays) under different plant densities. Journal of Hydrology 271:188–196. https://doi.org/10.1016/S0022-1694(02)00347-5

[29] Kato T, Kimura R, Kamichika M (2004) Estimation of evapotranspiration, transpiration ratio and water-use efficiency from a sparse canopy using a compartment model. Agricultural Water Management 65:173–191. https://doi.org/10.1016/j.agwat.2003.10.001

[30] Fisher JB, Debiase TA, Qi Y, Xu M, Goldstein AH (2005) Evapotranspiration models compared on a Sierra Nevada forest ecosystem. Environmental Modelling & Software 20:783–796. https://doi.org/10.1016/j.envsoft.2004.04.009

[31] Zhou M, Ishidaira H, Hapuarachchi H, Magome J, Kiem A, Takeuchi K (2006) Estimating potential evapotranspiration using Shuttleworth–Wallace model and NOAA-AVHRR NDVI data to feed a distributed hydrological model over the Mekong River basin. J Hydrol 327(1):151–173. https://doi.org/10.1016/j.jhydrol.2005.11.013

[32] Ortega-Farias S, Carrasco M, Olioso A, Acevedo C, Poblete C (2007) Latent heat flux over Cabernet Sauvignon vineyard using the Shuttleworth and Wallace model. Irrig Sci 25:161–170. https://doi.org/10.1007/s00271-006-0047-7

[33] Kool D, Agam N, Lazarovitch N, Heitman JL, Sauer TJ, Ben-Gal A (2014) A review of approaches for evapotranspiration partitioning. Agric For Meteorol 184:56–70. https://doi.org/10.1016/j.agrformet.2013.09.003

[34] Reinds GJ, van Oijen M, Heuvelink GBM, Kros H (2008) Bayesian calibration of the VSD soil acidification model using European forest. Geoderma 146:475–488. https://doi.org/10.1016/j.geoderma.2008.06.022

[35] Zhu GF, Su YH, Li X, Zhang K, Li CB (2013) Estimating actual evapotranspiration from an alpine grassland on Qinghai–Tibetan plateau using a two-source model and parameter uncertainty analysis by Bayesian approach. J Hydrol 476:42–51. http://dx.doi.org/10.1016/j.jhydrol.2012.10.006

[36] Zhu GF, Li X, Su YH, Zhang K, Bai Y, Ma JZ, Li CB, Hu XL, He JH (2014) Simultaneously assimilating multivariate data sets into the two-source evapotranspiration model by Bayesian approach: application to spring maize in an arid region of northwestern China. Geosci Model Dev 7:1467–1482. https://doi.org/10.5194/gmdd-7-741-2014

[37] Wei G, Zhang X, Ye M, Yue N, Kan F (2019) Bayesian performance evaluation of evapotranspiration models based on eddy covariance systems in an arid region. Hydrol Earth Syst Sci 23:2877–2895. https://doi.org/10.5194/hess-23-2877-2019

[38] Chen DY, Wang X, Liu SY, Wang YK, Gao ZY, Zhang LL, Wei XG, Wei XD (2015) Using Bayesian analysis to compare the performance of three evapotranspiration models for rainfed jujube (Ziziphus jujuba Mill) plantations in the Loess Plateau. Agr Water Manage 159:341–357. https://doi.org/10.1016/j.agwat.2015.06.004

[39] Song Y, Jin L, Zhu G, Ma M (2016) Parameter estimation for a simple two-source evapotranspiration model using Bayesian inference and its application to remotely sensed estimations of latent heat flux at the regional scale. Agric For Meteorol 230–231:20–32. https://doi.org/10.1016/j.agrformet.2016.03.019

[40] Clark JS, Gelfand AE (2006) Hierarchical Modeling for the Environmental Sciences: Statistical Methods and Applications. Oxford University Press, Oxford

[41] Nilsson H, Rieskamp J, Wagenmakers E (2011) Hierarchical Bayesian parameter estimation for cumulative prospect theory. J Math Psychol 55(1):84–93. https://doi.org/10.1016/j.jmp.2010.08.006

[42] Nimmo JR, Schmidt KM, Perkins KS, Stock JD (2009) Rapid measurement of field-saturated hydraulic conductivity for areal characterization. Vadose Zone J 8:142–149. https://doi.org/10.2136/vzj2007.0159

[43] Noshadi M, Parvizi H, Sepaskhah AR (2012) Evaluation of different methods for measuring field saturated hydraulic conductivity under high and low water table. Vadose Zone J 11:1-9. https://doi.org/10.2136/vzj2011.0005

[44] Valiantzas JD (2010) New linearized two-parameter infiltration equation for direct determination of conductivity and sorptivity. J Hydrol 384(1–2):1–13. https://doi.org/10.1016/j.jhydrol.2009.12.049

[45] Mishra SK, Tyagi JV, Singh VP (2003) Comparison of infiltration models. Hydrol Process 17(13):2629–2652. https://doi.org/10.1002/hyp.1257

[46] Dashtaki SG, Homaee M, Hahdian MH, Kouchakzadeh M (2009) Site-dependence performance of infiltration models. Water Resour Manage 23(13):2777–2790. https://doi.org/10.1007/s11269-009-9408-3

[47] Duan R, Fedler CB, Borrelli J (2011) Field evaluation of infiltration models in lawn soils. Irrigat Sci. 29(5):379–389. https://doi.org/10.1007/s00271-010-0248-y

[48] Harden CP, Scruggs PD (2003) Infiltration on mountain slopes: A comparison of three environments. Geomorph 55(1–4):5–24. https://doi.org/10.1016/S0169-555X(03)00129-6

[49] Reynolds WD, Elrick DE (1990) Ponded infiltration from a single ring: 1. Analysis of steady state flow. Soil Sci Soc Am J 54(5):1233–1241. https://doi.org/10.2136/sssaj1990.03615995005400050006x

[50] Davidoff B, Selim HM (1986) Goodness of fit for eight water infiltration models. Soil Sci Soc Am J 50(3):759–764. https://doi.org/10.2136/sssaj1986.03615995005000030039x

[51] Ander Kutílek M, Nielsen DR (1994) Soil hydrology. Catena, Cremlingen–Destedt, Germany

[52] Philip JR (1990) Inverse solution for one-dimensional infiltration, and the ratio A/K_1. Water Resour Res 26(9):2023–2027. https://doi.org/10.1029/WR026i009p02023

[53] Swartzendruber D (1987) A quasi-solution of Richards' equation for the downward infiltration of water into soil. Water Resour Res 23(5):809–817. https://doi.org/10.1029/WR023i005p00809

[54] Brutsaert W (1977) Vertical infiltration in dry soil. Water Resour Rres 13(2):363–368. https://doi.org/10.1029/WR013i002p00363

[55] Kutílek M, Nielsen DR (1994) Soil hydrology. Catena, Cremlingen–Destedt, Germany

[56] Mezencev VJ (1948) Theory of formation of the surface runoff (In Russian). Meteorologiae Hidrologia 3:33–40.

[57] Horton RE (1940) An approach toward a physical interpretation of infiltration capacity. Proc Soil Sci Soc Am 5:339–417.

[58] Reynolds WD (2008) Saturated hydraulic properties: ring infiltrometer. In: Carter MR, Gregorich EG (eds) Soil sampling and methods of analysis, 2nd ed. CRC Press Taylor & Francis, USA, Boca Raton, pp. 1043–1056.

[59] White I, Sully MJ (1987) Macroscopic and microscopic capillary length and time scales from field infiltration. Water Resour Res 23(8): 1514-1522. https://doi.org/10.1029/WR023i008p01514

[60] Reynolds WD, Elrick DE, Youngs EG (2002) Single-ring and double-or-concentric-ring infiltrometer. In: Dane JH, Topp GC (eds) Methods of soil analysis. Madison: Soil Sci Soc Am, pp 821–826.

[61] Lasdon LS, Fox RL, Ratner MW (1974) Nonlinear optimization using the generalized reduced gradient method. Revue française d'automatique, d'informatique et de recherché 3:73–103. https://doi.org/10.1051/ro/197408V300731

[62] Marquardt DW (1963) An algorithm for least-squares estimation of nonlinear parameters. J Soc Indust Appl Math 11(2):431–441. https://doi.org/10.1137/0111030

[63] Levenberg K (1944) A method for the solution of certain non-linear problems in least squares. Quart Appl Math 2:164–168. https://doi.org/10.1090/qam/10666

[64] Ardia D, Boudt K, Carl P, Mullen KM, Peterson BG (2011) Differential evolution with DEoptim. R J 3(1):27–34.

[65] Nash JE, Sutcliffe JV (1970) River flow forecasting through conceptual models part I– A discussion of principles*. J Hydrol 10(3):282–290. https://doi.org/10.1016/0022-1694(70)90255-6

[66] Rao CR (1965) Linear Statistical Inference and its Applications. John Wiley and Sons, Inc, New York. https://doi.org/10.1002/bimj.19680100127

[67] Anderson TW (1958) An introduction to multivariate statistical analysis. John Wiley & Sons, New York

[68] Smiles DE, Knight JH (1976) A note on the use of the Philip infiltration equation. Aust J Soil

Res 14(1):103–108. https://doi.org/10.1071/SR9760103

[69] Di Prima S, Lassabatere L, Rodrigo-Comino J, Marrosu R, Pulido M, Angulo-Jaramillo R, Úbeda X, Keesstra S, Cerdà A, Pirastru M (2018) Comparing transient and steady-state analysis of single-ring infiltrometer data for an abandoned field affected by fire in Eastern Spain. Water 10(4) 514. https://doi.org/10.3390/w10040514

[70] Moorhead JE, Marek GW, Colaizzi PD, Gowda PH, Evett SR, Brauer DK, Marek TH, Porter DO (2017) Evaluation of sensible heat flux and evapotranspiration estimates using a surface layer scintillometer and a large weighing lysimeter. Sensors 17(10): 2350 https://doi.org/10.3390/s17102350

[71] Aubinet M, Vesala T, Papale D (2012) Eddy covariance: A practical guide to measurement and data analysis, Springer, Heidelberg, New York, 438 pp

[72] Eugster W and Merbold L (2015) Eddy covariance for quantifying trace gas fluxes from soils. SOIL 1: 187–205. https://doi:10.5194/soil-1-187-2015

[73] Prueger JH, Hatfield JL, Aase JK, Pikul JL Jr (1997) Bowen-ratio comparisons with lysimetric evapotranspiration. Agron J 89(5):730–736

[74] Pruitt WO, Swain BD, Held A, Sutton B, Matista A, Hsiao TC (1987) Bowen ratio and Penman: Australian–California test. Irrigation Systems for the 21st Century, Proc. Irrig and Drain Spec Conf, ASCE, Portland, Oregon

[75] Ortega-Farias SO, Cuenca RH, Ek M (1996) Daytime variation of sensible heat flux estimated by the bulk aerodynamic method over a grass canopy. Agric For Meteorol 81 (1):131–143. http://doi.org/10.1016/0168-1923(95)02278-3

[76] Unland HE, Houser PR, Shuttleworth WJ, Yang ZL (1996) Surface flux measurement and modeling at a semi-arid Sonoran Desert site. Agric For Meteorol 82:119–153. https://doi.org/10.1016/0168-1923(96)02330-1

[77] Ohmura A (1982) Objective criteria for rejecting data for Bowen ratio flux calculations. J Appl Meteor 21(4):595–598. https://doi.org/10.1175/1520-0450(1982)021<0595: OCFRDF>2.0.CO;2

[78] Guo X, Zhang H, Kang L, Du J, Li W, Zhu Y (2007) Quality control and flux gap filling strategy for Bowen ratio method: revisiting the Priestley–Taylor evaporation model. Environ Fluid Mech 7(5):421–437. http://dx.doi.org/10.1007/s10652-007-9033-8

[79] Liu H, Foken T (2001) A modified Bowen ratio method to determine sensible and latent heat fluxes. Meteorologische Zeitschrift 10(1):71–80. http://dx.doi.org/10.1127/0941-2948/2001/0010-0071

[80] Perez PJ, Castellvi F, Ibañez M, Rosell JI (1999) Assessment of reliability of Bowen ratio method for partitioning fluxes. Agric For Meteorol 97(3):141–150. https://doi.org/10.1016/S0168-1923(99)00080-5

[81] Payero JO, Neale CMU, Wright JL, Allen RG (2003) Guidelines for validating Bowen ratio data. Trans ASAE 46 (4):1051–1060

[82] Savage MJ, Everson CS, Metelerkamp BR (2009) Bowen ratio evaporation measurement in a remote montane grassland: Data integrity and fluxes. J Hydrol 376 (1):249–260. https://doi.org/10.1016/j.jhydrol.2009.07.038

[83] Flumignan DL, Faria RT, Prete CEC (2011) Evapotranspiration components and dual crop coefficients of coffee trees during crop production. Agrc Water Manage. 98, 791–800. https://doi.org/10.1016/j.agwat.2010.12.002.

[84] Williams DG, Cable W, Hultine K, Hoedjes JCB, Yepez EA, Simonneaux V, Er-Raki S, Boulet G, de Bruin HAR, Chehbouni A, Hartogensis OK, Timouk, F (2004) Evapotranspiration components determined by stable isotope, sap flow and eddy covariance techniques. Agric Forest Meteorol. 125 (3–4), 241–258. https://doi.org/10.1016/j.agrformet.2004.04.008

[85] Moran MS, Scott RL, Keefer TO, Emmerich WE, Hernandez M, Nearing GS, Paige GB, Cosh MH, O'Neill PE (2009) Partitioning evapotranspiration in semiarid grassland and shrubland ecosystems using time series of soil surface temperature. Agric For Meteorol. 149(1), 59–72. https://doi.org/10.1016/j.agrformet.2008.07.004

[86] Monteith JL (1965) Evaporation and environment. In Symposia of the Society for Experimental Biology; Cambridge University Press (CUP): Cambridge, UK, Volume 19, pp. 205–234.

[87] Anadranistakis M, Liakatas A, Kerkides P, Rizos S, Gavanosis J, Poulovassilis A (2000) Crop water requirements model tested for crops grown in Greece. Agr Water Manage. 45, 297–316. https://doi.org/10.1016/S0378-3774(99)00106-7

[88] Gardiol JM, Serio LA, Maggiora AD (2003) Modelling evapotranspiration of corn (Zea mays) under different plant densities. J Hydro. 271, 188–196. https://doi.org/10.1016/S0022-1694(02)00347-5

[89] Shuttleworth WJ, Wallace JS (1985) Evaporation from sparse crops – an energy combination theory. Quart J Roy Meteorol Soc. 111, 839–855. https://doi.org/10.1002/qj.49711146910

[90] Samanta S, Mackay DS, Clayton MK, Kruger EL, Ewers BE (2007) Bayesian analysis for uncertainty estimation of a canopy transpiration model. Water Resour Res. 43. https://doi.org/10.1029/2006WR005028

[91] Finsterle S, Najita J (1998) Robust estimation of hydrologic model parameters. Water Resour Res. 34, 2939–2947. https://doi.org/10.1029/98WR02174

[92] Morey RD, Pratte MS, Rouder JN (2008) Problematic effects of aggregation in z ROC analysis and a hierarchical modeling so-lution. J Math Psychol. 52, 376–388. https://doi.org/10.1016/j.jmp.2008.02.001

[93] Weine NNO (2013) Review of Efforts to Combat Desertification and Arrest and Reverse Land Degradation in Myanmar. In Com-bating Desertification in Asia, Africa and the Middle East.; Heshmati G., Squires, V., Eds.; Springer, Dordrecht, Holland. https://doi.org/10.1007/978-94-007-6652-5_14

[94] Casanova D, Epema GF, Goudriaan J (1998) Monitoring rice reflectance at field level for estimating biomass and LAI. Field Crops Res. 55, 83–92. https://doi.org/10.1016/S0378-4290(97)00064-6

[95] Allen RG, Jensen ME, Wright JL, Burman RD (1989) Operational Estimates of Reference Evapotranspiration. Agron J. 1989, 81, 650. https://doi.org/10.5897/SRE2015.6238

[96] Kim S, Kim HS (2008) Neural networks and genetic algorithm approach for nonlinear evaporation and evapotranspiration mod-eling. J Hydrol. 351, 299–317. https://doi.org/10.1016/j.jhydrol.2007.12.014

[97] Shibayama M, Sakamoto T, Takada E, Inoue A, Morita K, Takahashi W, Kimura A (2011) Estimating Paddy Rice Leaf Area Index with Fixed Point Continuous Observation of Near Infrared Reflectance Using a Calibrated Digital Camera. Plant Produc Scien. 14(1), 30–46. https://doi.org/10.1626/pps.14.30

[98] Wei Z, Lee X, Wen X, Xiao W (2018) Evapotranspiration partitioning for three agro-ecosystems with contrasting moisture con-ditions: a comparison of an isotope method and a two-source model calculation. Agri For Meteorol. 252, 296–310. https://doi.org/10.1016/j.agrformet.2018.01.019

[99] Kar G, Kumar A (2007) Surface energy fluxes and crop water stress index in groundnut under irrigated ecosystem. Agric For Me-teorol. 2007, 146(1), 94–106. https://doi.org/10.1016/j.agrformet.2007.05.008

[100] Banik CN, Nath R, Chakraborty PK (2009) Effect of dates of sowing on growth and yield of groundnut crop. J Crop Weed. 5(2), 59–62.

[101] Chapman SC, Hammer GL, Palta JA (1993) Predicting leaf area development of sunflower. Field Crop Res. 34, 101–112. https://doi.org/10.1016/0378-4290(93)90114-3

[102] Chongdar S, Singharoy A, Saha A, Chhetri B (2015) Performance of summer sesame (Sesamum indicum L.) cultivars under varying dates of sowing in prevailing agro-climatic condition of North Bengal. Sci Res Essays. 10(12), 411–420. https://doi.org/10.5897/SRE2015.6238

[103] Shuttleworth WJ, Gurney RJ (1990) The theoretical relationship between foliage temperature and canopy resistance in sparse crops. Q J Roy Meteorol Soc. 116, 497–519. https://doi.org/10.1002/qj.49711649213

[104] Jarvis PG (1976) The interpretation of the variations in leaf water potential and stomatal conductance found in canopies in the field. Philos Trans R Soc Lond. 273, 593–610. https://doi.org/10.1098/rstb.1976.0035

[105] Stewart JB (1988) Modelling surface conductance of pine forest. Agr Forest Meteorol. 43, 19–35. https://doi.org/10.1016/0168-1923(88)90003-2

[106] Li S, Kang S, Zhang L, Ortega-Farias S, Li F, Du T, Tong L, Wang S, Ingman M, Guo W (2013) Measuring and modeling maize evapotranspiration under plastic film-mulching condition. J Hydrol. 503(1), 153–168. https://doi.org/10.1016/j.jhydrol.2013.07.033

[107] Stewart GH (1988) The influence of canopy cover on understorey development in forests of the western Cascade Range, Oregon, USA. Vegetatio. 76, 79–88. https://doi.org/10.1007/BF00047391

[108] Brutsaert W (1982) Theory, History, and Applications. In Evaporation into the atmosphere: Reidel, Dordrecht, Holland, p. 299.

[109] Stan Modelling Language Users Guide and Reference Manual, Version 2.4. Available online: http://mc-stan.org/rstan. (Accessed on 23 October 2020).

[110] Sellers PJ, Heiser MD, Hall FG (1992) Relations between surface conductance and spectral vegetation indices at intermediate (100 m^2 to 15 km^2) length scales. J Geophys Res. 97, 19033–19059. https://doi.org/10.1029/92JD01096

[111] Meng W, Xihuan S, Juanjuan M, Xianghong G, Tao L, Ruofan L (2019) Measurement and simulation of the water storage pit irrigation trees evapotranspiration in the Loess Plateau. Agric Water Manage. 2019, 226. https://doi.org/10.1016/j.agwat.2019.105804

[112] Gavilán P, Berengena J (2007) Accuracy of Bowen ratio-energy balance method for measuring latent heat flux in a semiarid ad-vective environment. Irrig Sci. 25(2), 127–140. https://doi.org/10.1007/s00271-006-0040-1

[113] Ershadi A, McCabe MF, Evans JP, Wood EF (2015) Impact of model structure and parameterization on Penman–Monteith type evaporation models. J Hydro. 525, 521–535. https://doi.org/10.1016/j.jhydrol.2015.04.008.

[114] Stannard DI (1993) Comparison of Penman-Monteith, Shuttleworth-Wallace, and Modified Priestley-Taylor Evapotranspiration Models for wildland vegetation in semiarid rangeland. Water Resour Res. 29(5), 1379–1392. https://doi.org/10.1029/93WR00333

[115] The CBS, Simmonds LP, Wheeler TR (2001) Modelling the partitioning of solar radiation capture and evapotranspiration in-tercropping systems, Proceedings of the 2nd International Conference on Tropical Climatology, Meteorology and Hydrology TCMH-2001, Brussels, Belgium.

[116] Zhang B, Kang S, Li F, Zhang L (2008) Comparison of three evapotranspiration models to Bowen ratio-energy balance method for a vineyard in an arid desert region of northwest China. Agric Forest Meteorol. 148, 1629–1640. https://doi.org/10.1016/j.agrformet.2008.05.016.

[117] Ortega-Farias SO, Olioso A, Fuentes S, Valdes H (2006) Latent heat flux over a furrow-irrigated tomato crop using Penman–Monteith equation with a variable surface canopy resistance. Agric Water Manage. 82, 421–432. https://doi.org/10.1016/j.agwat.2005.07.028

[118] Burba GG, Verma SB (2005) Seasonal and interannual variability in evapotranspiration of native tallgrass prairie and cultivated wheat ecosystems. Agr For Meteorol. 135 (1-4), 190–201. https://doi.org/10.1016/j.agrformet.2005.11.017

[119] Alves I, Cameira M (2002) Evapotranspiration estimation performance of root zone water quality model: evaluation and im-provement. Agric Water Manag. 57:61–73. https://doi.org/10.1016/S0378-3774(02)00038-0

[120] Denmead OT (1976) Temperate Cereals. In Vegetation and the Atmosphere.; Monteith, J.L., Ed.; Academic Press, New York, USA. Volume 2, pp.1–31

[121] Uchijima Z (1976) Maize and rice. In Vegetation and the Atmosphere.; Monteith, J.L., Ed.; Academic Press, New York, USA. Volume 2, pp.33–64.

[122] Monteith JL (1973) Principles of Environmental Physics; Edward Arnold, London, UK. p.241

[123] Yamano T, Arouna A, Labarta RA, Huelgas ZM, Mohanty S (2016) Adoption and impacts of international rice research technologies. *Global food Sec.* 8, 1–8. https://doi.org/10.1016/j.gfs.2016.01.002.

[124] Long HL (2014) Land consolidation: an indispensable way of spatial restructuring in rural China. *J. Geogr. Sci.* 24, 211–225. https://doi.org//10.1007/s11442-014-1083-5.

[125] Peng S, Tang Q, Zou Y (2009) Current status and challenges of rice production in china. *Plant Prod. Sci.* 12, 3–8. https://doi.org/10.1626/pps.12.3.

[126] Xu L, Zhan X, Yu T, Nie L, Huang J, Cui K, Wang F, Li Y, Peng S (2018) Yield performance of direct-seeded, double-season rice using varieties with short growth durations in central China. *Field Crop Res*, 227, 49–55. https://doi.org/10.1016/j.fcr.2018.08.002.

[127] Chen Q, He A, Wang W, Peng S, Huang J, Cui K, Nie L (2018) Comparisons of regeneration rate and yields performance between inbred and hybrid rice cultivars in a direct seeding rice-ratoon rice system in central China. *Field Crop Res*, 223, 164−170. https://doi.org/10.1016/j.fcr.2018.04.010.

[128] Liang Y, Zhang Q, Zhou J, Li Y, Tan C, Huang H (2016) Effects of different cultivation patterns on rice quality and economic efficiency. *Acta Agr Boreali Sinica*, 31, 265–269 (In Chinese with English Abstract).

[129] Sen LTH, Bond J (2017) Agricultural adaptation to flood in lowland rice production areas of central Vietnam: understanding the 'regenerated rice' ratoon system. *Clim. Dev*. 9, 274–285. https://doi.org/10.1080/17565529.2016.1149440.

[130] Elias RS (1969) Rice production and minimal tillage. *Outlook Agric*, 6, 67–70.

[131] Prashar CRK (1970) Paddy ratoons. *World Crops*, 22, 145–147.

[132] Babaee M, Shahnazari A, Mashaal M, Azadegan B (2019) Investigation of water use efficiency and water productivity in second cultivating system and ratoon cultivation in Sari (abstract in English). *Iran J of Irri Drain*, 13, 69–77.

[133] Yuan S, Cassman KG, Huang J, Peng S, Grassini P (2019) Can ratoon cropping improve resource use efficiencies and profitability of rice in central China? *Field Crops Res*, 234, 66–72. https://doi.org/10.1016/j.fcr.2019.02.004.

[134] Wang W, He A, Jiang G, Sun H, Jiang M, Man J, Ling X, Cui K, Huang J, Peng S, Nie L (2020) Ratoon rice technology: A green and resource-efficient way for rice production.

Advanc Agron, 159, 135–167. https://doi.org/10.1016/bs.agron.2019.07.006.

[135] Zhang L, Jiang P, Gou X, Zhou X, Zhu Y, Liu M, Xiong H, Xu F (2019) Integrated Water and Nitrogen Management Practices to Enhance Yield and Environmental Goals in Rice–Ratoon Rice Systems. *Agron J*, 111, 2821–2831. https://doi.org/10.2134/agronj2018.10.0691.

[136] Dong H, Chen Q, Wang W, Peng S, Huang J, Cui K, Nie L (2017) The growth and yield of a wet-seeded rice-ratoon rice system in central China, *Field Crops Res*, 208, 55–59. https://doi.org/10.1016/j.fcr.2017.04.003.

[137] Munda GC, Das A, Patel DP (2009) Evaluation of transplanted and ratoon crop for double cropping of rice (Oryza sativa L.) under organic input management in mid altitude sub-tropical Meghalaya. *Curr. Sci*, 96. 1620–1627.

[138] Bouman BAM, Peng S, Castaneda AR, Visperas RM (2005) Yield and water use of irrigated tropical aerobic rice systems. *Agr Water Manage*, 74, 87–105. https://doi.org/10.1016/j.agwat.2004.11.007.

[139] Tabbal DF, Bouman BAM, Bhuiyan SI, Sibayan EB, Sattar MA (2002) On-farm strategies for reducing water input in irrigated rice; case studies in the Philippines. *Agr Water Manage*, 56, 93–112. https://doi.org/10.1016/S0378-3774(02)00007-0.

[140] Kumar V, Ladha JK (2011) Chapter six - Direct seeding of rice: Recent developments and future research needs. *Advanc Agron*, 111, 297–413. https://doi.org/10.1016/B978-0-12-387689-8.00001-1.

[141] Lv Y, Xu J, Yang S, Liu X, Zhang J, Wang Y (2018) Inter-seasonal and cross-treatment variability in single-crop coefficients for rice evapotranspiration estimation and their validation under drying-wetting cycle conditions. *Agric Water Manage*, 196, 154–161. https://doi.org/10.1016/j.agwat.2017.11.006.

[142] Mizutani M, Prasanta KK, Shinde D (1989) Effect of Different Rice Varieties and Mid-Term Drainage Practice on Water Requirement in Dry Season Paddy - Observational studies on water requirement of low land rice in Thailand (I)-. *J Irriga Engine Roral Planning*, 17, 6–20. https://doi.org/10.11408/jierp1982.1989.17_6.

[143] Tyagi NK, Sharma DK, Luthra SK (2000) Determination of evapotranspiration and crop coefficients of rice and sunflower with lysimeter. *Agric Water Manage*, 45, 41–54.

[144] Yan HF, Zhang C, Oue H, Peng GJ, Darko RO (2017) Determination of crop and soil evaporation coefficients for estimating evapotranspiration. *Int J Agric & Biol Eng*, 10, 130–139. https://doi.org/10.25165/j.ijabe.20171004.2290

[145] Department of Agricultural Planning (DAP) Ministry of Agriculture Livestock and Irrigation (2016) *Myanmar Agriculture in Brief* ; DAP: Naypyitaw, Myanmar.

[146] Phyo AS, Grunbuhel CM, Williams L, Htway SS (2019) Does selective mechanization make up for labor shortages in rural Myanmar? *IOP Conf. Ser. Earth Environ. Sci*, 338.

[147] FAO Myanmar and AVSI Foundation (2019) *Handbook on Climate Smart Agriculture in*

Myanmar.; FAO and AVSI Foundation: Nay Pyi Taw, Myanmar.

[148] Penman HL (1948) Natural evaporation from open water, bare soil and grass. *Proc. Roy. Soc*, 193, 120–146. https://doi.org/10.1098/rspa.1948.0037.

[149] Allen RG, Jensen ME, Wright JL, Burman RD (1989) Operational estimates of reference evapotranspiration. *Agron J*, 81. 650. https://doi.org/10.5897/SRE2015.6238.

[150] Jensen ME, Burman RD, Allen RGZ(1990) Evapotranspiration and irrigation water requirements. In *ASCE Manuals and Reports on Engineering Practices No. 70.*; Am Soc Civ Engr: New York, USA.

[151] Kim S, Kim HS (2008) Neural networks and genetic algorithm approach for nonlinear evaporation and evapotranspiration modeling. *J Hydro*, 351, 299–317. https://doi.org/10.1016/j.jhydrol.2007.

[152] Shibayama M, Sakamoto T, Takada E, Inoue A, Morita K, Takahashi W, Kimura A (2011) Estimating paddy rice leaf area index with fixed point continuous observation of near infrared reflectance using a calibrated digital camera. *Plant Prod Sci*, 14, 30–46. https://doi.org/10.1626/pps.14.30.

[153] Wei Z, Lee X, Wen X, Xiao W (2018) Evapotranspiration partitioning for three agro-ecosystems with contrasting moisture conditions: a comparison of an isotope method and a two-source model calculation. *Agri For Meteor*, 252, 296–310. https://doi.org/10.1016/j.agrformet.2018.01.019.

[154] Stan modeling language users guide and reference manual, version 2.4. Available online: http://mc-stan.org/rstan (Accessed on 15 December 2021).

[155] Wood SN (2004) Stable and efficient multiple smoothing parameter estimation for generalized additive models. *J. Am. Statist. Ass*, 99, 673–686.

[156] Dai LY, Kariya K,Ye CR, Ise K, Tanno HI, Yu TQ, Xu FR (2002) Studies on cold tolerance of rice, Oryza sativa L. II. Evaluation on cold tolerance of Yunnan rice genetic resources. *Southwest China J Agri Sci*, 15, 47–52.

[157] He A, Wang W, Jiang G, Sun H, Jiang M, Man J, Cui K, Huang J, Peng S, Nie L (2019) Source-sink regulation and its effects on the regeneration ability of ratoon rice. *Field Crops Res*, 236, 155-164. https://doi.org/10.1016/j.fcr.2019.04.001.

[158] Harrel DL, Bond JA, Blanche S (2009) Evaluation of maincrop stubble height on ratoon rice growth and development. *Field Crops Res*, 114, 396–403. https://doi.org/0.1016/j.fcr.2009.09.011.

[159] Santos AB, Fageria NK, Prabhu AS (2003) Rice ratooning management practices for higher yields. *Commun. Soil. Sci. Plant Anal*, *34*, 881–918, https://doi.org/10.1081/CSS-120018981.

[160] Faruq G, Taha RM, Prodhan ZH (2014). Rice ratoon crop: A sustainable rice production system for tropical hill agriculture. *Sustainability*, *6*, 5785–5800.

[161] Steduto P, Hsiao TC, Fereres E (2007) On the conservative behavior of biomass water productivity. *Irrig Sci*, 25, 189–207. https://doi.org/10.1007/s00271-007-0064-1.

[162] Hassan AA, Sarkar AA, Ali MI (1989) Effect of fertilizer and water management practices on rice production in the Ganges-Kobadok (G.K.) project area. *Nucl. Sci. Appl*. 1, 48–53.

[163] Sandhu BS, Khera KL, Prihar SS, Singh B (1980). Irrigation needs and yield of rice on a sandy-loam soil as affected by continuous and intermittent submergence. *Ind. J. Agric. Sci*, 50, 492–496.

[164] Uppal HS, Cheema SS, Walla AS (1991) Irrigation need of transplanted rice in non-cracking soil. *Ind. J. Agric. Sci.* 61, 634–636.

[165] Islam MZ, Haq KA, Bhuiyan LR (1986) Effect of different water management practices on grain yield, weed population and recovery of applied nitrogen in rice cultivation. *Bangladesh J. Agric*, 11, 57–64.

[166] Sarkar AA, Hassan AA, Ali MH, Karim NN (2002) Supplemental irrigation for Binashail rice cultivation at two agro-ecological zones of Bangladesh. *Bangladesh J. Agric. Sci*, 29, 95–100.

Acknowledgments

I wish to express my sincere appreciation to the organization: Japan International Research Center for Agricultural Sciences Research (JIRCAS) to have opportunities for this research funded by JIRCAS from 2017 to 2021.

I would like to express my deepest gratitude to Professor Yutaka Matsuno at Kinki University and Professor Yoshiyuki Shinogi at Kyushu University for their generous support, suggestions, and discussion on this doctoral dissertation.

I would like to express special appreciation to Dr. Naing Kyi Win at Department Agricultural Research (DAR), Myanmar for his insightful comments and thoughtful support on my research in Myanmar.

I am also greatly indebted to Dr. Khin Mar Htay, Dr. Aung Kyaw Thu, U Kyaw Myaing, Daw Thin Mar Cho, Daw Lae Lae Mon, Daw Nwe Ni, Daw Kywae, U Thura, Daw Loon Poe Poe and Daw Chaw Su, DAR for their enormous support and encouragement in conducting the experiments.

I would like to thank assistant workers of Water Utilization Research section and Natural Resource Study section, DAR for their great contribution to the field work, too.

Last but not least, a sweet word to all members of my family, they vitally encouraged and sympathized for my study.

SHIRAKI Shutaro

March 2023